Redox-activated Covalent Functionalization of Semiconductor Surfaces

Thesis by

Maureen Baradi Morla

In Partial Fulfillment of the Requirements for the Degree of
Doctor of Philosophy

CALIFORNIA INSTITUTE OF TECHNOLOGY
Pasadena, California

2023
(Defended April 20, 2023)

ORCID: 0000-0002-2520-9543

Acknowledgements

I am grateful to so many colleagues, peers, mentors, family, and friends that it feels nearly impossible to account for every single individual in such a short span of pages. First, I need to thank my Ph.D. advisor Nate Lewis for allowing me to work in this group. Throughout my time, I have been absolutely blessed to learn such a large variety of skills and concepts from so many talented peers. Nate is incredible at creating a space where students feel welcome and safe, where they feel they can take full charge of their own schedules, and where they can flourish and learn about whatever it is that interests them. I am also thankful to Nate for always being so understanding and empathetic as an advisor. I would also like to thank Miguel Cabán-Acevedo for his mentorship. I am grateful for his guidance and for allowing me to pick his brain for my projects. Bruce Brunschwig and Kimberly Papadantonakis have also been incredibly instrumental in propelling my projects forward and have provided me with invaluable insight and direction, both in science and in life. I would also like to thank Barbara Miralles, who is an absolutely vital pillar for the functioning of the Lewis group, and without her, I am certain that my time in graduate school would have been far more difficult. I am also grateful to Bill Goddard, Soonho Kwon, and Charles Musgrave for their time and crucial advice during our collaboration on the density functional theory work discussed in this thesis. Without them, I certainly would have been lost and unable to complete the story. Finally, I would like to thank Professors Harry Gray, Geoffrey Blake, and Bill Goddard for offering their support and time by serving on my committee.

As exciting as it all was, my journey from my small rural hometown in Gonzales, CA to this point has been nothing short of arduous. I attended a Title I K-12 school district, surrounded by children who were also first-generation Americans or were often immigrants themselves. I reflect on these days with profound nostalgia and gratitude, as it was there where my STEM teachers supported my goals to become a scientist as best they could, knowing full well that our small community did not really have enough resources to aid or prepare me. I'd especially like to thank Ms. Sloan, my chemistry teacher, for being the first to show me how beautiful it is that everything in this universe is comprised of the same tiny building blocks and for always believing in me. I am so honored to be representing my little hometown as a female first-generation American scientist.

My family left everything they knew in the Philippines to pursue a better life for their children. Both of my parents worked very long hours when they reached America and made many sacrifices for us over the years. I am grateful to them for passing onto me their principles of endurance, ambition, diligence, and relentless pursuit of the unknown. My mother says she “built my big brain by eating many clams.” I’m not sure if that’s how it works, but I’m thankful anyway. My recent trip to the Philippines in 2022 also taught me a lot about my heritage. In their tiny fisherman village off the coast of Luna, La Union, my father’s mother instilled in her children the importance of higher education and demanded that they each pursued a degree. My grandfather fought for the U.S. Army in WWII so that he could open opportunities for his children in America. I fully realize now that I am carrying the hopes and dreams of not just my parents, but the generations before them as well. I am so grateful to my elders for paving this path forward for me from an ocean away. As the first in my family to receive a Ph.D., I’d like to think my ancestors are throwing me a thumbs up from above.

I want to thank the friends and loved ones who have supported me to this point of my life even though they are no longer present. Throughout my graduate school career, I lost many whom I held dear to my heart for many years to a wide variety of reasons, including death. I especially want to pay tribute to my late maternal grandmother for the kindness she showed me while I was growing up. Despite the language barrier, I found solace in those memories every time I struggled in graduate school, even as she quickly lost her own ability to remember. Mahal kita, Lola.

The Lewis group has changed in size dramatically over the course of my stay at Caltech, and I am thankful for every single person I’ve encountered along the way. I’ve had the pleasure of sharing many whole workdays plumbing, wiring, and tweaking my wrist while tightening bolts and screws with my fellow XPS GLAs Jake Evans, Sean Byrne, Ellen Yan, Annelise Thompson, and Michael Mazza. Troubleshooting has never been so tiresome and yet so entertaining. Renata Balgley was a helpful member of the surfaces subgroup, and I had a grand time shooting ideas back and forth with her. Birch Simpson and Kyra Lee have been steadfast friends, even long after they left the group, and I am so grateful for all their support and love. Noyes 220 has been an incredibly supportive office space to be a part of, and I'm thankful for all the memories I've made here, from boba and coffee runs, looking for campus printers because the one in the SURF room was spitting out Wingding curses, many ridiculous conversations, you name it. Lastly, I'm thankful for my cohort members Madeline Meier, Jackie Dowling, and Zach Ifkovits. Planning a group retreat for nearly 30 people would've been impossible without them.

One of the most important people I have met at Caltech is my dear friend James Lawniczak. I'm so thankful I was able to persuade him to pick Caltech because every moment we have spent together has been so precious to me. I know that I can call him at 11 PM, and he'll be enthusiastic to drive an hour to the beach, go to Denny's to chat over endless hot chocolate and mozzarella sticks, or just grab tea and go anywhere the wind takes us. He's my go-to friend for hiking, the most objective rock-solid human being to ask for both life and scientific advice, and insanely honest, genuine, and kind. He's the best.

Over the last two years of my time in graduate school, I moved to South Bay LA where I met a spectacular eclectic group of people who have truly turned my whole world upside down with all of the love and fun we have shared. In such a short span of time, I have created so many wonderful memories with Robert Marrast, Missy Whalen, and Sergio Bazan. From climbing on rooftops, heated political debates, the most aggressive Uno card games I have ever played, spontaneous and not-so-spontaneous adventures out of South Bay, zoning out over movies and TV shows, to gaining the nickname "Doom Squad" at our local bar, nothing has been short of wildly entertaining with this group of friends. They're the best friends I could've ever made, and I am so endlessly thankful that they are in my life. They're my family. I know that they'd go the extra mile for me and back, in the same way that I would for them.

When I passed my candidacy exam, I adopted a Korean Jindo named Sumi who was rescued from an Asian dog meat farm. She saw me through many highs and lows during my graduate career, and in every way, she was my right-hand companion. There is something so beautiful about meeting a creature who was once so afraid and skeptical and seeing them blossom with so much confidence given the right love and care. Despite our time together ending abruptly and tragically, I am grateful for every moment I spent with her. I only wish she could’ve been here to see me through this achievement too. However, through this loss, I also learned that the human heart has an enormous capacity to love, and I welcomed another spunky puppy into my life whom I fondly named Luna in dedication to all of my favorite people whom I met at night. Luna is so full of love, charisma, and energy, and it has been a joy to watch her grow up even though she still tries to pull my sleeves while I’m working.

Finally, I am thankful for my significant other Sam Pessoa. When I first drove into LA with my father to attend graduate school, it was 110 °F with lightning storms looming in the distance. I jokingly said it was a sign that I was heading toward a very tumultuous chapter of my life, and for my first year of graduate school, it was. However, when I met Sam, I was soon able to see LA as home. I am grateful for every time he stormed into my apartment with a pack of water bottles because he thought I didn’t drink enough water, for each time he took me out to eat and then ordered an obnoxious amount of food only to make me take all of the leftovers home, for each time he listened to me vent about my project struggles despite not understanding half of the things I said, for making me tea and setting snacks on my desk while I worked, and for sticking around through all the beautiful moments and difficult periods. Over the years, we’ve probably overcome more life challenges than many people our age, but through all the good and the bad, I wouldn’t have become who I am now without him.

Abstract

Semiconducting materials are those with a band gap across which electrons can be excited when the material absorbs photons with sufficient energy. Surface functionalization of semiconductors involves manipulation of the properties of the material by attaching organic small molecules through a surficial covalent bond. By controlling the surface properties of the material, functionalization has enabled the application of semiconductors in a myriad of fields, prompting a highly active field of research. To aid in this effort, we explore a new reaction methodology based on redox-mediated surface functionalization, where an outer-sphere, one-electron metallocene reductant or oxidant is added to the solution medium containing the semiconductor and the small molecule to be added to its surface. Using density functional theory, we elucidated the thermodynamic and kinetic factors that limit the experimentally observed upper coverage bound of reductant-activated methylation of 1T′-molybdenum disulfide by determining two governing factors: 1) sulfur sites with longer Mo–S bonds are more thermodynamically favorable for methyl addition, and 2) sulfur sites with fewer adjacent methylated sulfur sites are preferentially functionalized due to steric hindrance. We then expanded this reductant-activated reaction methodology to silicon(111) surfaces and demonstrated that the reductant solution potential must lie near or above the silicon(111) conduction band edge to observe reactivity. By extending this study to silicon nanocrystals of different sized diameters and different conduction band edges, we found that the extent of surface reactivity relied heavily on reductant strength, but the energy difference between the conduction band edges was too small to observe a distinct dependency on nanocrystal size. The work encompassed in this thesis expanded our understanding of redox-mediated reactions on semiconductor surfaces, providing a new avenue for attaining atomic-level control of the surficial properties of the material using mild reaction conditions and no specialized equipment. Furthermore, redox-activated addition enables the use of new functional groups that would otherwise be reactive in other functionalization methods, promoting an abundance of opportunities to explore new applications of semiconductor materials.

Published Content and Contributions

Portions of this thesis have been drawn from the following manuscripts in preparation or submitted:

Morla, M. B.; Balgley, R.; Carim, A. I.; Lewis, N. S. Reductant-Activated Electrophilic Addition to Hydrogen-Terminated Silicon Nanocrystal Surfaces. *In preparation.*
M.B.M. collected and analyzed the data with input from R.B. The manuscript was prepared by M.B.M. with input from co-authors.

Yan, E.X.*; **Morla, M. B.***, Kwon, S.; Musgrave, C. B.; Brunschwig, B. S.; Kempler, P. A.; Goddard, W. A.; Lewis, N. S. Theoretical Analysis of Thermodynamic and Kinetic Limitations for Covalent Functionalization of 1T′-MoS_2: A model for methylation coverage on chemically exfoliated MoS_2. *Submitted*.
E.X.Y performed low-coverage methyl functionalization calculations and analysis and coded the coverage simulations. M.B.M. performed propyl and high-coverage methyl functionalization calculations and handled the submission and revision process. S.K. and C.M. provided input on the details of the calculations. The manuscript was prepared by E.X.Y and M.B.M. with input from co-authors (* indicates equal first-author contribution).

Balgley, R.; **Morla, M. B**.; Yu, W.; Lewis, N. S. Reductant-Activated Electrophilic Functionalization of Hydrogen-Terminated Si(111). *Submitted*.
R.B. collected the data and analyzed the data with input from M.B.M. The manuscript was prepared and submitted by R.B. with input from co-authors, and the revision process was handled by M.B.M.

Other contributions to published content not included in this thesis:

Yan, E. X.; Balgley, R.; **Morla, M. B**.; Kwon, S.; Musgrave, C. B.; Brunschwig, B. S.; Goddard, W. A.; Lewis, N. S. Experimental and Theoretical Comparison of Potential-dependent Methylation on Chemically Exfoliated WS_2 and MoS_2. *ACS Appl. Mater. Interfaces*, **2022**, *14(7)*, 9744-9753. doi: 10.1021/acsami.1c20949

Evans, J. M.*; Lee, K. S.*; Yan, E. X.*; Thompson, A. C.; **Morla, M. B**.; Meier, M. C.; Ifkovitz, Z. P.; Carim, A. I.; Lewis, N. S. Demonstration of a Sensitive and Stable Chemical Gas Sensor Based on Covalently Functionalized MoS_2. *ACS Materials Lett.*, **2022**, *4(8)*, 1475-1480. doi: 10.1021/acsmaterialslett.2c00372

Ifkovits, Z. P.; Evans, J. M.; Kempler, P. A.; **Morla, M. B**.; Pham, K. H.; Dowling, J. A.; Carim, A. I.; Lewis, N. S. Powdered $Mn_ySb_{1-y}O_x$ Catalysts for Cerium-Mediated Oxygen Evolution in Acidic Environments. *ACS Energy Lett.*, **2022**, *7(12)*, 4258-4264. doi: 10.1021/acsenergylett.2c01754

Table of Contents

List of Figures

List of Tables

Chapter 1 – Introduction

1.1 Electronic Structure of Semiconducting Materials

Semiconductors are a diverse class of inorganic materials with conductivity lying between metals and insulators.[1] This conductivity is heavily dependent on the electronic structure of the material, which is characterized by the delocalization of electrons throughout the semiconducting solid and can be described by the band theory of solids.[2] These materials can have a variety of crystal structures created by repeating molecular or atomic units in a distinct arrangement. Excluding complications that arise from symmetry and spin-orbit coupling considerations, the electronic structure of semiconductors can be described as a set of localized molecular orbitals that are constructed based on a set of valence orbitals, where the effect of delocalization of electrons are then incorporated as individual orbitals as the number of repeating units in the crystal structure increases to infinity.[2] Unlike in organic conductive polymer descriptions, the energy spacing between the large number of tightly packed molecular orbitals can be ignored for most purposes and thus be considered continuous bands of energy levels. The group of fully occupied bonding orbitals are defined as the valence band and the group of vacant antibonding orbitals are denoted as the conduction band of the material (Figure 1.1). The energy gap between these is called the band gap of the material. When the semiconducting solid absorbs photons with energy greater than the band gap, electrons can be excited from the valence band to the conduction band, which is the principle which many semiconductor applications are built upon. In metals, there is no band gap which allows electrons to move freely throughout the material resulting in high conductivity, and in insulators, the band gap is too large to readily excite electrons across resulting in poor conductivity. In this thesis, we focus on the surface chemistry of 1T′ phase of molybdenum disulfide nanosheets (1T′-MoS_2) which is quasi-metallic with a band gap of 0.1 eV,[3–5] bulk silicon(111) with a band gap of 1.1 eV,[2] and silicon nanocrystals (Si NCs) with diameters of 8 nm, 5 nm, and 3 nm that correspond to band gaps of 1.23 eV, 1.35 eV, and 1.67 eV, respectively.[6]

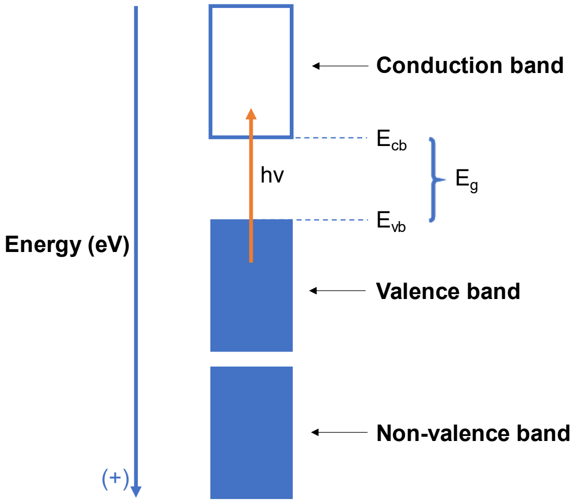

Figure 1.1 A schematic representation of the electronic structure of a semiconducting material described using band theory. The shaded area represents the bands occupied fully with electrons, where the valence band is defined as the highest occupied band of orbitals (E_{vb}). The non-shaded area denotes the vacant conduction band (E_{cb}). The energy gap between the valence band and conduction band is the band gap of the material (E_g). When the semiconductor absorbs photons with sufficient energy greater than the band gap energy, electrons can be excited from the valence band to the conduction band.

1.2 Surface Functionalization and Applications

Surface functionalization is a method of covalently attaching small molecules to the surface of a material and has large and various impacts on the behavior of the surface. These reactions manipulate the surface properties at a molecular level to control the nanoscopic and macroscopic properties of the material to enable its use in diverse applications.[7] Surface functionalization can be used to passivate the surface and protect the semiconductor from oxidation under ambient conditions, tune the band gap and resulting optical and electronic properties, covalently link semiconductor materials to other structures, attach biomolecules or molecular catalysts, or to tailor the solubility of nano-sized semiconductor materials for novel purification methods, inks, or biological applications.

The 1T phase (1 layer in the unit cell, T = tetragonal) of MoS_2 is metastable and can be described as the perfectly octahedral phase that may spontaneously distort to the 1T′ and 1T″ phases, where 1T′ is the most stable of the three with an energetic barrier of >0.7 eV preventing its conversion into the 1H phase (H = hexagonal).[3,8] This material is the focus of our work presented in Chapter 2. 1T′-MoS_2 is synthesized via chemical or electrochemical intercalation and exfoliation of the 2H phase. In this process, intercalation imparts excess negative charge to the MoS_2, and the addition of a protonated solvent results in separation of the layers into nanosheet suspensions of chemically exfoliated MoS_2 (*ce*MoS_2).[9–11] This additional negative charge increases the nucleophilicity of the material allowing for the addition of electrophilic small molecules to its surface. Surface functionalization stabilizes the 1T′ phase, barring its transformation into the 2H phase that would otherwise occur over days to weeks.[12] Researchers have developed a variety of applications for 1T′-MoS_2 in electrocatalysis as a hydrogen evolution catalyst,[13–18] in gas and electrochemical sensors,[19,20] and in bioimaging.[21]

Another semiconducting material studied in this thesis are silicon materials, a member of the Group 14 materials. The bulk Si(111) material (111 = crystal face) possesses a band gap of 1.12 eV and its structural and electronic properties are previously well described.[2] Si(111) oxidizes readily to form a thin outer oxide layer that passivates the surface.[22] To tailor its properties for a desired application, a variety of methods exist to functionalize the surface of Si(111), most of which begin with a reactive hydrogen-terminated surface achieved by first etching the surface with hydrogen fluoride to remove the oxide layer. Following this step, small molecules can be covalently linked to the surface via hydrosilylation reactions with unsaturated hydrocarbons, carbene insertions, electrografting with unsaturated hydrocarbons in the presence of diazonium salts, scanning probe-induced cathodic electrografting with alkynes, and by electrochemical derivatization of the surface using Grignard reagents.[23–35] Another means of functionalizing the surface is through a two-step chlorination/alkylation sequence, where the Si(111) surface is terminated with chlorine to produce a highly reactive intermediate state. Such functionalization methods have enabled wide-ranging applications in electronics, sensing, and solar cells.[36–45]

Because silicon in the bulk is a semiconductor with an indirect band gap, dipole-forbidden band gap optical transitions result in longer charge carrier lifetimes, and recombination is dominated by non-radiative processes.[46,47] However, when the size of the material is reduced to the nanocrystalline regime (below ~10 nm), Si NCs display unique optical properties such as observable, tunable photoluminescence with a photoemission maximum at 1.7 eV.[46] Currently, two main theories are being investigated to elucidate the origin of this photoluminescence: 1) passivation of surface traps that are otherwise present in bulk silicon, and 2) the band gap transition becomes weakly dipole-allowed within the quantum-confined size regime.[46] Nevertheless, Si NCs have recently garnered considerable research interest for their aforementioned properties and for the highly attractive possibility of low-cost solution-processing in the production of different technologies.[48] Methods of functionalizing these surfaces include thermal hydrosilylation with unsaturated hydrocarbons, oxidant-activated nucleophilic addition, radical-initiated addition, Lewis acid-mediated addition, photochemical reactions, and microwave-heating methods.[6,48] These routes have enabled the use of Si NCs in a myriad of applications including bioimaging, light-emitting diodes, photodiodes, catalysis, sensing, and antimicrobial coatings.[49–53]

1.3 Scope of this Thesis

This thesis works toward understanding the redox-mediated surface functionalization reactions of semiconducting materials, including 1T′-MoS_2 nanosheets, Si(111), and Si NCs. In Chapter 2, we explore the thermodynamic and kinetic limitations of reductant-activated addition of electrophiles to 1T′-MoS_2 surfaces using density functional theory (DFT) in order to explain the experimental upper and lower limits of functional group coverage. In Chapter 3, we investigate reductant-activated addition of electrophiles to Si(111) as an analogy to the oxidant-activated addition of methanol to Si(111) that our group previously reported. Chapter 4 extends this methodology to Si NCs, where we explore the influence of reductant strength and Si NC size on the reductant-activated reaction, effectively completing our experimental understanding of redox-mediated reactions on Si materials. In Chapter 5, we develop a time-dependent method of synthesizing Si NCs with a narrow size distribution via reductive thermal annealing and use oxidant-activated addition to create a mixed monolayer on its surface. At the end of this chapter, we present a strategy for using this mixed monolayer and a two-step, orthogonal reaction approach to crosslink Si NCs and form a mesostructured Si material within which carriers can more freely move, which has enormous implications for developing non-toxic silicon-based inks for use in next-generation photovoltaics.

Chapter 2 – Density Functional Theory Modeling of 1T′-Molybdenum Disulfide Surface Functionalization

2.1 Introduction

Molybdenum disulfide, MoS_2, is a two-dimensional layered transition metal dichalcogenide (TMD) that can be in either a semiconducting (2H, 3R) or metallic/quasi-metallic phase (1T, 1T′).[8,54–56] MoS_2 has been studied for a variety of applications in optoelectronics,[57,58] sensing,[9,19,20,59,60] catalysis,[15,18,61,62] photothermal imaging,[21,63,64] drug delivery,[64–67] and antibacterial coatings.[68,69] For many applications, the 1T and 1T′ phases can be interchanged because both behave as metals, although the 1T′ phase possesses a very small bandgap of ~0.1–0.2 eV.[3–5] Functionalization methods for TMDs in both the 2H and 1T′ phases have been developed to explore the potential benefits and effects of functionalization.[12,70–84]

Density functional theory (DFT) calculations can be used to determine the structure and reactivity of 2H-, 1T-, and 1T′-MoS_2 and have provided useful insights for understanding experimental observations and predicting reaction sites for functionalization and catalysis in a variety of scenarios.[3,8,55,74] For example, DFT calculations have provided insight into the mechanism for diazonium radical functionalization on 2H-MoS_2, indicating that the reaction follows a nucleation-propagation sequence and that this propagation relies on vacancy- and functionalization-induced reactivity in neighboring sulfurs.[74]

Chemically exfoliated MoS_2 (*ce*MoS_2) generated via lithium intercalation and water exfoliation of MoS_2 allows preparation of functionalized 1T′-MoS_2. The exfoliated MoS_2 undergoes a 2H to 1T′ phase transition and reacts with an electrophile to form a carbon–sulfur bond.[12,79–81] *ce*MoS_2 is in the distorted 1T′ phase rather than the 1T based on scanning transmission electron microscopy and photoemission spectroscopy.[4,8,85] DFT calculations have shown that the 1T phase is 0.3 and 0.9 eV per Mo higher in energy than the 1T′ and 1H phases, respectively, and thus the 1T phase spontaneously distorts to the 1T′ phase.[3,55] The distortion of the 1T to 1T′ phase results in two distinct sulfur sites instead of one, which may impact the reactivity of the 1T′ surface. For example, hydrogen adsorption studies on 2H-, 1T-, and 1T′-MoS_2 indicated that adsorption on 1T′ was at least twice as favorable as adsorption on 1T.[3]

Reductant-activation using one-electron donors such as metallocenes can increase the fraction of functionalized sulfur on *ce*MoS_2 by two-fold, from ~40% to ~70% per MoS_2, as the reductant strength increases.[81] However, the maximum observed methyl fractional coverage was ~70% per MoS_2, i.e., ~35% per sulfur. Compared to the 100% methyl coverage that can be obtained on other surfaces such as silicon(111),[86] 35% appears to be a relatively low upper bound, and the observation consequently remains unexplained in detail.

The goal was to use DFT calculations to elucidate the thermodynamics and kinetics of alkyl halide functionalization on 1T′-MoS_2 as a function of potential.[81] Using the GC-DFT method, calculations of free energy as a function of fixed charge were converted to a function of fixed potential, allowing calculation of and comparison between the ΔG and $\Delta G^{\ddagger}$ of reactions at fixed potential.[87] Previous DFT studies have explored functionalization of 1T-MoS_2,[88] in contrast to our investigations of the thermodynamic and kinetic limits of alkyl halide reactions with 1T′-MoS_2, which is believed to be the phase adopted by *ce*MoS_2.

Our work specifically focused on investigating the thermodynamics and kinetics of reaction between methyl chloride ($ClCH_3$) and a periodic slab of 1T′-MoS_2 (Figure 2.1), in conjunction with assessing the primary factors that contribute to limitations on the coverage of methyl groups on such functionalized surfaces. Both the thermodynamics and kinetics of the methylation reaction were investigated on unfunctionalized MoS_2, and then the work focused solely on the thermodynamics for methylation reactions on functionalized MoS_2.

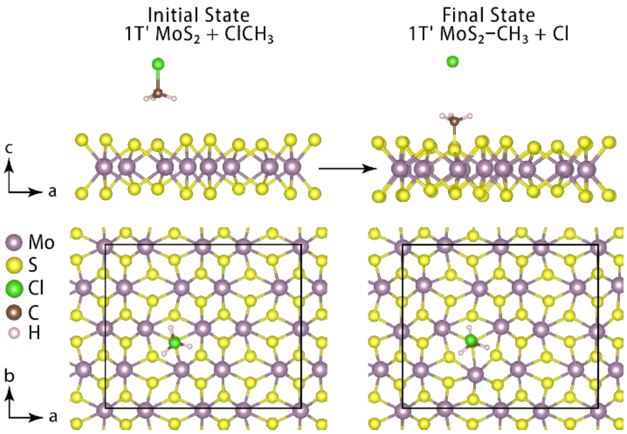

Figure 2.1 Reaction scheme for the 1T′-MoS_2 methylation reaction be discussed in this paper, viewed along the b- and c-axes of the rectangular cell. Shown here is the initial methylation. The left side shows the initial state, with ClCH3 suspended over the sulfur to be functionalized, and the right side shows the final state after the reaction is finished. Both structures were optimized with Δn = 2, where Δn is the number of excess electrons ($n – n_0$).

2.2 Computational Methods

To determine the ground-state structure for 1T′-MoS_2, DFT calculations were performed using the Vienna ab initio simulation package (VASP) with plane wave basis sets and projector augmented-wave pseudopotentials (PAW).[89,90] The geometries were optimized using the Perdew-Burke-Ernzerhof (PBE) exchange-correlation functional[91] with the Becke-Johnson D3 correction for dispersion.[92] The criteria of convergence for energy and forces were set to 1×10^{-5} eV and 0.01 eV/Å, respectively. Water was modeled as the solvent and the cavitation energy contribution was neglected.[93] A plane wave energy cutoff of 500 eV was applied and a Γ-centered 6×6×1 Monkhorst-Pack *k*-grid was used for a 1×2 periodic slab of 1T′-MoS_2 with a 30 Å vacuum slab. The 1×2 unit cell of 1T′-MoS_2 obtained from previous work was transformed from a hexagonal cell to a rectangular cell.[8] The 1×2 unit cell was then converted into a 2×4 supercell containing 16 Mo atoms and 32 S atoms, and was re-optimized using a 3×3×1 *k*-grid (Figure 2.2). The cell parameters and volume were fixed in subsequent optimizations for functionalized 1T′-MoS_2. The nudged elastic band (NEB) method was used to calculate the reaction barriers and transition states for all reactions.[94]

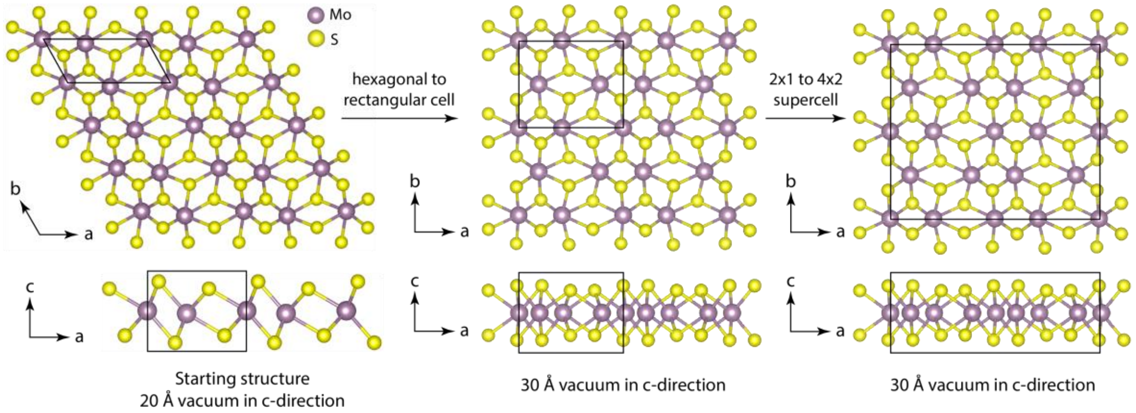

Figure 2.2 From left to right, the starting 1T′-MoS$_2$ structure obtained from literature, the transformation of the starting structure to a rectangular cell with 30 Å of vacuum (middle), and the expansion of the unit cell into a 16 MoS$_2$ supercell. The unit cell extends beyond the visual area of the *c*-axis for the bottom row of images.

To determine the reduction potential of 1T′-MoS$_2$ vs SHE relative to vacuum as a function of the number of excess electrons in the slab, we used the grand-canonical joint DFT (jDFTx) method with the CANDLE solvation model and 0.1 M KF in water.[95,96] To interpolate the free energy of structures at the desired potential, the free energy vs number of electrons was fitted to a quadratic curve, according to a previously reported GC-DFT method (Figure 2.3 and Figure 2.4, see Appendix for calculation details).[87]

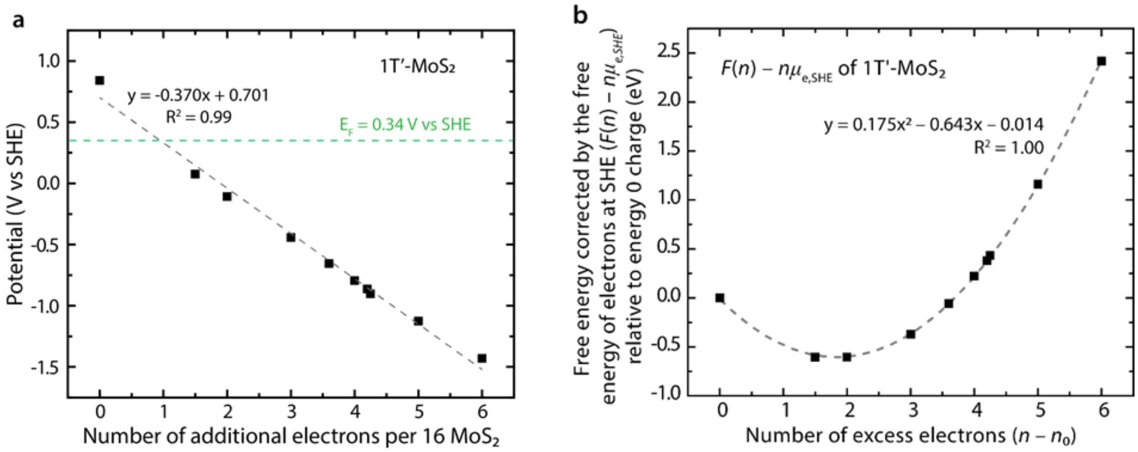

Figure 2.3 The effects of adding electrons to 1T′-MoS$_2$ containing 16 MoS$_2$ units on the (a) potential, in V vs SHE, and (b) free energy corrected by the free energy of electrons at the standard hydrogen electrode. In (a), the potential with respect to the number of electrons is fitted linearly, and in (b), the free energy corrected linearly by the free energy of electrons (–4.44 eV) is fitted quadratically. Electrochemical potentials and free energy values were obtained using jDFTx after geometry optimization using VASP. The Fermi level is illustrated in (a) as a green line.[81]

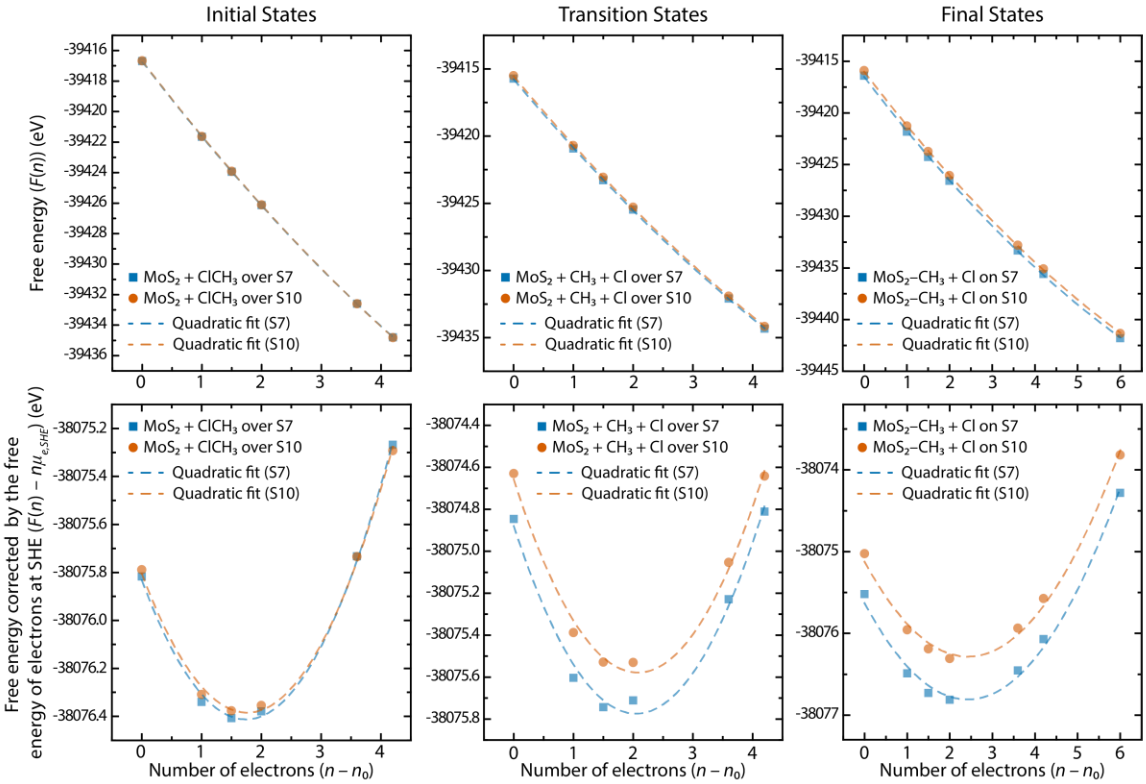

Figure 2.4 Free energy of the initial state (left column), transition state (middle column), and final state (right column) of the MoS_2 + $ClCH_3$ reaction on S7 and S10 as a function of the number of electrons relative to the neutral charge ($\Delta n = n - n_0$). The points are energies calculated using DFT and dashed curves indicate the interpolated fit that is a quadratic fit vs the number of electrons *n*. The quadratic nature of the free energy dependence on the number of electrons *n* is more apparent once corrected for the electronic free energy at the standard hydrogen electrode (bottom row).

To better corroborate experimental observations, some structures in this study have been optimized with $\Delta n = 1.5$–2, where Δn is the total number of excess electrons, which corresponds to an electrochemical potential near the middle of the range spanned by the reductants experimentally tested.[81]

Although the reductant-activated experimental research was conducted with methyl iodide, methyl chloride was used as the reactant for the theoretical study due to incompatibilities between the iodine and bromine pseudopotentials in combination with solvation during structural optimization using VASP. These incompatibilities resulted in significant convergence issues and unreasonable energies during the study. Despite the difference in halide between this study and the methyl iodide used in the experimental work, we believe that the relative trends obtained using methyl chloride will be consistent with the behavior of methyl bromides and iodides.

2.3 Results and Discussion

2.3.1 Potential dependence of 1T′-MoS_2 on the number of electrons

A cornerstone of our analysis is the use of GC-DFT to relate the structural free energies as a function of the number of electrons to the free energies as a function of electrochemical potential, thereby facilitating meaningful comparisons between the calculation results and experimental data.[97,98] This process has been described previously and is described briefly in the Appendix.[87] To illustrate this process, we first discuss the relationship between the potential and the number of excess electrons on a 1T′-MoS_2 slab containing 16 MoS_2 units.

A periodic slab of 1T′-MoS_2 that consists of 16 MoS_2 units in the unit cell was constructed based on a previously optimized 1T′-MoS_2 structure obtained from literature.[8] Figure 2.3a plots the potential vs SHE of the MoS_2 slab as a function of the number of excess electrons (Δn). Each point corresponds to an individual optimization and free energy calculation, whereby the structure was optimized using VASP and a single-point free energy calculation was subsequently performed using jDFTx. The potential is thus reflective of any changes in the optimal structure resulting from addition or subtraction of electrons. The grand canonical potential of each transition state was obtained from each NEB calculation with different charges. Figure 2.3b plots the grand free energy of the MoS_2 slab referenced to the energy at zero charge ($\Delta n = 0$) corrected by the free energy contribution of an electron at SHE using the electronic energy at SHE, $\mu_{e,SHE}$, as a function of the number of excess electrons, fitted to a quadratic curve. This procedure was used for all structures in this work. A detailed analysis and derivation has been presented previously.[87]

2.3.2 Differences in thermodynamics and kinetics of methylation on the two types of sulfur on 1T′-MoS_2

A focus of our work was understanding differences in reactivity towards nucleophilic addition with methyl chloride to the two types of sulfurs in the 1T′ phase. The distortion of the 1T to the 1T′ phase results in sulfurs with shorter, “low-S,” and longer, “high-S,” Mo–S bonds (Figure 2.5), following the nomenclature used in previous computational studies of 1T′-MoS_2.[3]

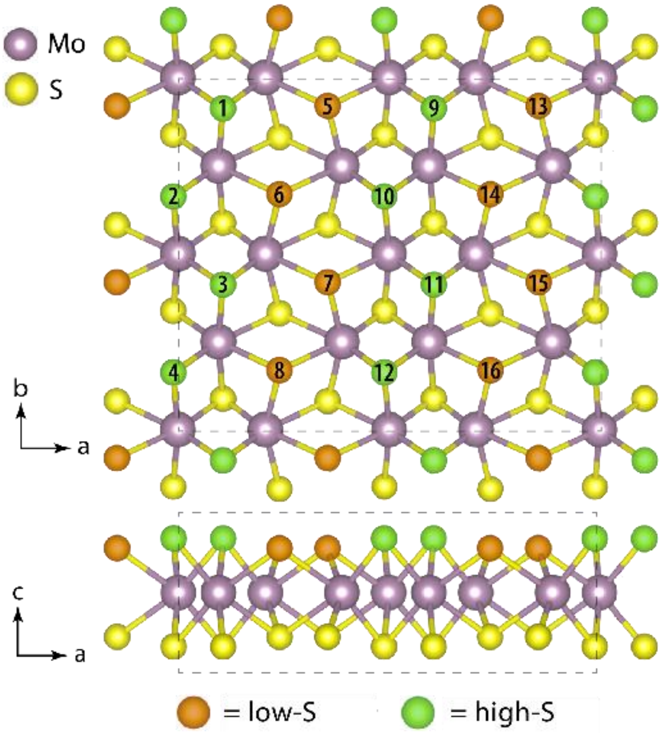

Figure 2.5 Top-down and side view of the rectangular unit cell of the minimized 1T′-MoS_2 supercell, color-coded to show the two types of sulfur in the unit cell: low-S and high-S, with low-S having a longer average Mo–S distance and high-S having a shorter average Mo–S distance and protruding further out-of-plane compared to the low-S.

The free energies of methylated MoS_2 were calculated for two sulfurs of each type at constant charge: S6 and S7 for low-S, S10 and S11 for high-S. The free energy of methylated MoS_2 depended primarily on whether the S was a high-S or low-S site. Only a small difference was obtained between the two low-S and two high-S sites (<0.1 eV), but a larger difference of ~0.5 eV was found between the two types of S sites (Figure 2.6). Low-S S7 and high-S S10 sites were selected to investigate the thermodynamics and kinetics of the methylation reaction as a function of potential, to reveal differences in methylating low-S vs high-S sites.

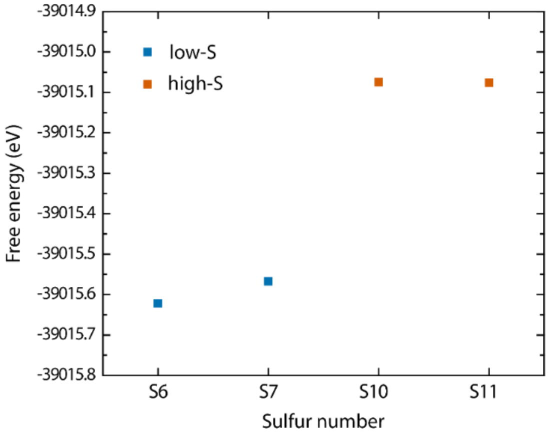

Figure 2.6 Free energy of $(MoS_2)_{16}(CH_3)$ with methyl on either S6, S7, S10, or S11, the former two being low-S and the latter two being high-S. Geometry optimizations and free energy calculations were performed on solvated structures that were negatively charged with Δ*n* = 2, resulting in structures with potentials –0.15, –0.16, –0.11, and –0.11 V vs SHE, respectively.

Figure 2.7 shows the reaction free energy (ΔG) and the free energy barrier ($\Delta G^{\ddagger}$) of methylation on S7 and S10. Figure 2.7 shows the potential dependence of the free energy of the system, the ΔG and $\Delta G^{\ddagger}$ values from 0.5 to –0.9 V vs SHE, with interpolated lines. The notation Δn refers to the number of excess electrons in the system ($n - n_0$), and U indicates the potential.

The potential window of 0.5 to –0.9 V vs SHE was explored, which captured a substantial portion of the electrochemical potentials used in the experimental work that explored the effects of reductant-activated functionalization on the methyl coverage of chemically exfoliated MoS_2 (*ce*MoS_2). Specifically, metallocene reductants with solution potentials ranging from –0.1 to –1.9 V vs $E(Fc^{+/0})$ (with Fc = ferrocene) were used in addition to no deliberate addition of a reductant.[81] The highest methyl coverage was observed when cobaltocene was used as the reductant (~ –1.3 V vs $E(Fc^{+/0})$). To determine the potential of *ce*MoS_2 in the absence of a reductant, drop cast *ce*MoS_2 electrodes were fabricated and the open-circuit potential was measured in acetonitrile under 1 atm of $N_2(g)$ with 0.10 M tetrabutylammonium perchlorate and 0.10 M methyl iodide. The measured open-circuit potential (–0.07 V vs $E(Fc^{+/0})$) was converted to the SHE (standard hydrogen electrode) scale using $E(Fc^{+/0})$ ~ SHE + 0.4 V, thus the potential for *ce*MoS_2 was simulated at 0.3 V vs SHE. For reference, the electrochemical potential of unfunctionalized 1T′-MoS_2 at zero charge was calculated to be 0.84 V vs SHE, which is 0.5 V positive of the open-circuit potential of *ce*MoS$_2$, and is consistent with experimental observations that as-synthesized *ce*MoS$_2$ is negatively charged.[85,99] X-ray photoelectron spectra of drop cast *ce*MoS$_2$ in the Mo 3*d* and S 2*p* regions were consistent with previously reported for spectra of *ce*MoS$_2$ (Figure 2.8).[12,79,81]

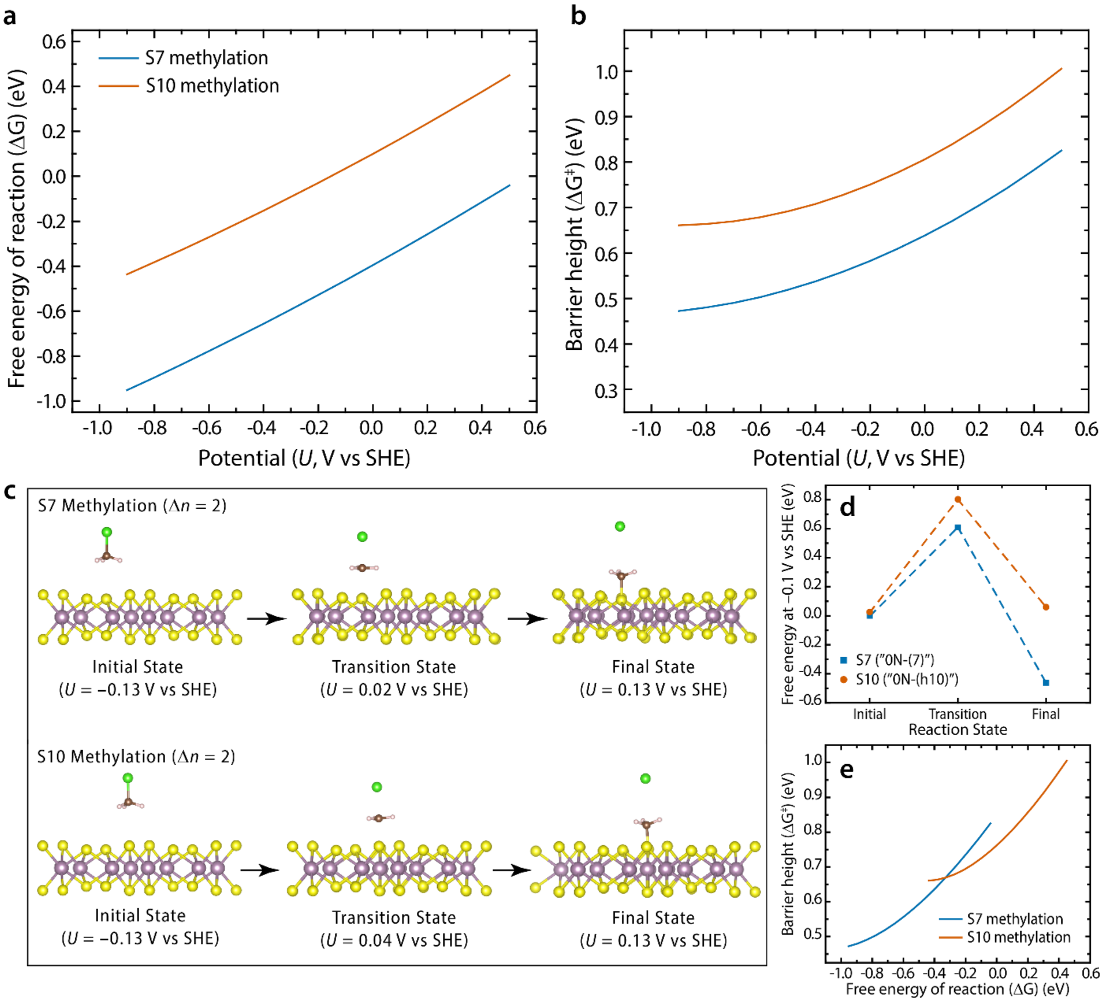

Figure 2.7 Addition of a single methyl to 1T′-MoS$_2$. (a) Thermodynamic favorability, ΔG, and (b) kinetic barrier, $\Delta G^{\ddagger}$, of methylation on S7 and S10 of 1T′-MoS$_2$ as a function of potential based on interpolations of the initial, transition, and final state free energies. (c) Side-view of the initial state, transition state, and final states for S7 and S10 methylation with $\Delta n = 2$ per 16 MoS$_2$. (d) Free energies at constant potential (–0.1 V vs SHE) for the initial, transition, and final states of S7 methylation ("0N-(7)") and S10 methylation, relative to the initial state energy of S7 methylation, to illustrate which states exert greater influence on the ΔG and $\Delta G^{\ddagger}$ at a given potential. This example shows that the transition and final states in the high-S methylation (S10) are destabilized relative to low-S methylation (S7) but the initial state energies are similar, resulting in a more positive ΔG and $\Delta G^{\ddagger}$ for high-S relative to low-S methylation. (e) The correlation between the barrier height and the free energy of reaction for S7 and S10 methylation, plotted using the same points as shown in (a) and (b). The reaction potential varies along each curve.

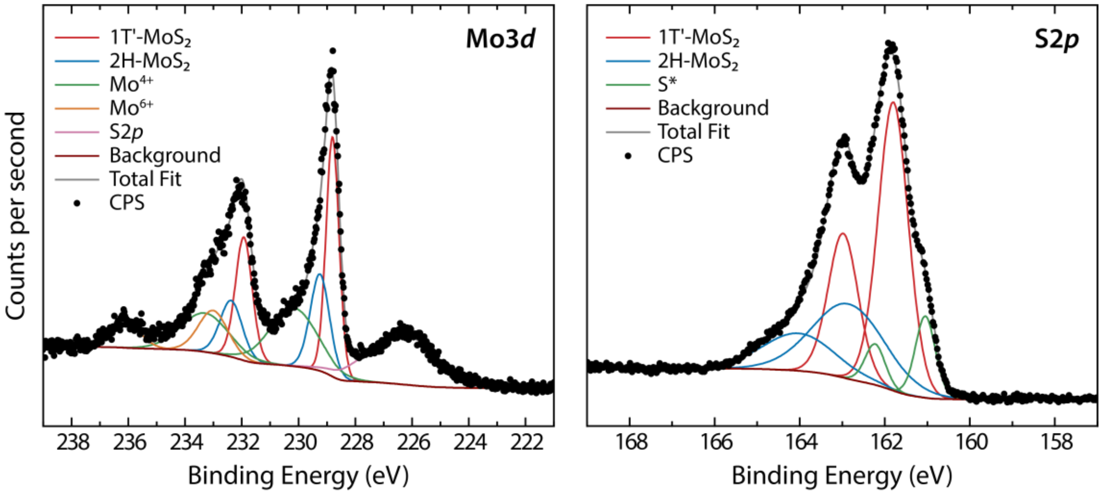

Figure 2.8 High-resolution Mo 3*d* and S 2*p* X-ray photoelectron spectra of chemically exfoliated MoS_2 used in open-circuit voltage measurements. For Mo 3*d*, $\Delta = 3.13$ eV and for S 2*p*, $\Delta = 1.18$ eV. All lineshapes are GL(30) and full-width-half-max were constrained to be less than 2.

The ΔG and $\Delta G^{\ddagger}$ for methylation of both S7 and S10 decreased as the potential became more negative (Figure 2.7a-b), consistent with experimental studies that have shown an increase in methyl coverage with increasing reductant strength.[81] Figure 2.7a-b also shows that ΔG for methylation of S10, a high-S atom, was consistently ~0.5 eV larger than ΔG for methylation of S7, a low-S atom. The barrier height for methylation of S10, $\Delta G^{\ddagger}$, is ~0.2 eV larger than the $\Delta G^{\ddagger}$ for S7 methylation. These results show that at a constant potential, low-S functionalization is preferred over high-S functionalization both thermodynamically and kinetically. A comparison of the initial-, transition-, and final-state energies at a fixed potential, such as at –0.1 V vs SHE (Figure 2.7d), indicates that the differences in ΔG and $\Delta G^{\ddagger}$ values are due to destabilization of the transition state and final state for S10 (high-S) methylation relative to S7 (low-S) methylation, whereas the initial states for these two reactions have relatively similar energies. A plot of $\Delta G^{\ddagger}$ vs ΔG (Figure 2.7e) reveals the correlation between the thermodynamics and kinetics for these two reactions as the potential changes.

Based on a Boltzmann distribution, the 0.5 eV difference between the ΔG values indicates that the probability of S10 methylation is 9 orders of magnitude lower than that of S7 methylation. The rate constants obtained using the Eyring equation to evaluate the rate constant k for S7 methylation were 2 s^{-1} but were only 0.002 s^{-1} for S10 methylation at 0.3

V vs SHE, a difference of 3 orders of magnitude (see Appendix for calculations). The Boltzmann distribution and Eyring equation are given by eq. 1 and 2:

$$p_i/p_j = exp(-(E_i - E_j)/k_BT) \qquad (1)$$

$$k = (k_BT/h)exp(-\Delta G^{\ddagger}/k_BT) \qquad (2)$$

where p_i is the probability of the system being in state i, $\underline{E}_i$ is the energy of state i, k_B is the Boltzmann constant, T is the temperature, k is the rate constant of the reaction, and h is Planck's constant.

The substantial thermodynamic and kinetic preference for the functionalization of low-S atoms originates from the longer Mo–S bond lengths for low-S relative to high-S sites. For high-S atoms, the Mo–S bond distances are 2.34, 2.39, and 2.46 Å, whereas for low-S atoms the distances are 2.35, 2.51, and 2.54 Å. As the Mo–S bond length increases, the covalent bond is weaker and more electron density is localized on the sulfur atom, making the sulfur more nucleophilic. Conversely, as the Mo–S bond shortens, more electron density from the sulfur participates in the Mo–S bond and becomes unavailable to participate in nucleophilic addition. Two of the Mo–S bonds for low-S sites are longer by 0.08–0.11 Å each, indicating that low-S atoms would be expected to preferentially engage in nucleophilic attack compared to the high-S atoms. Similar conclusions have been made in computational studies of hydrogen adsorption on low-S and high-S atoms, in which the ~0.7 eV difference in the free energy of H adsorption (0.06 eV on low-S, 0.73 eV on high-S) was ascribed to the more negatively charged low-S with a charge of –0.54, compared to high-S with a charge of –0.47,[3] as calculated using Bader's charge population analysis.[100] The same study also found that H atoms adsorbed on high-S sites moved to the nearest low-S sites with a barrier height of 0.15 eV that can be easily overcome at room temperature.[3]

Figure 2.9 shows that the S–C distance at the transition state increased as the potential decreased. An increase in the S–C distance implies that the transition state occurs earlier along the reaction coordinate, and thus more closely resembles the reactants, which is expected when the ΔG for the reaction becomes more negative. This behavior is consistent with the decrease in barrier height and increased thermodynamic favorability of methylation as the potential decreases (Figure 2.7). Thus, as the potential becomes more negative, the reaction becomes more exergonic, and the transition state moves closer along the reaction coordinate to the initial state.

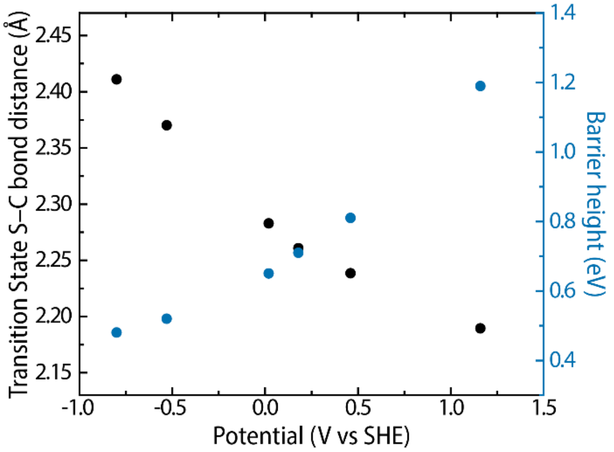

Figure 2.9 The S–C distance at the transition state and the corresponding barrier height of the reaction as a function of potential in V vs SHE. A single nudged elastic band calculation was performed at each potential. As the potential becomes more negative, the barrier height decreases and the S–C bond length increases, indicating that the transition state resembles the initial state more than the final state, consistent with the data in Figure 2.7 indicating a more exergonic reaction as the potential decreases.

In addition to methylation of the 1T′ phase, we also performed a relaxation of a methyl-functionalized 1T phase. Notably, the methylated 1T-MoS_2 distorted to a 1T′-like structure, although its minimized free energy was 1.6 eV higher than the structures shown above. Thus, functionalization necessitates that the 1T phase becomes distorted. The structures before and after the geometry optimization of the methylated 1T-MoS_2 are shown in Figure 2.10. The free energy of the resulting structure was higher than the structures obtained by optimizing starting from the 1T′ phase and thus was not used aside from this calculation.

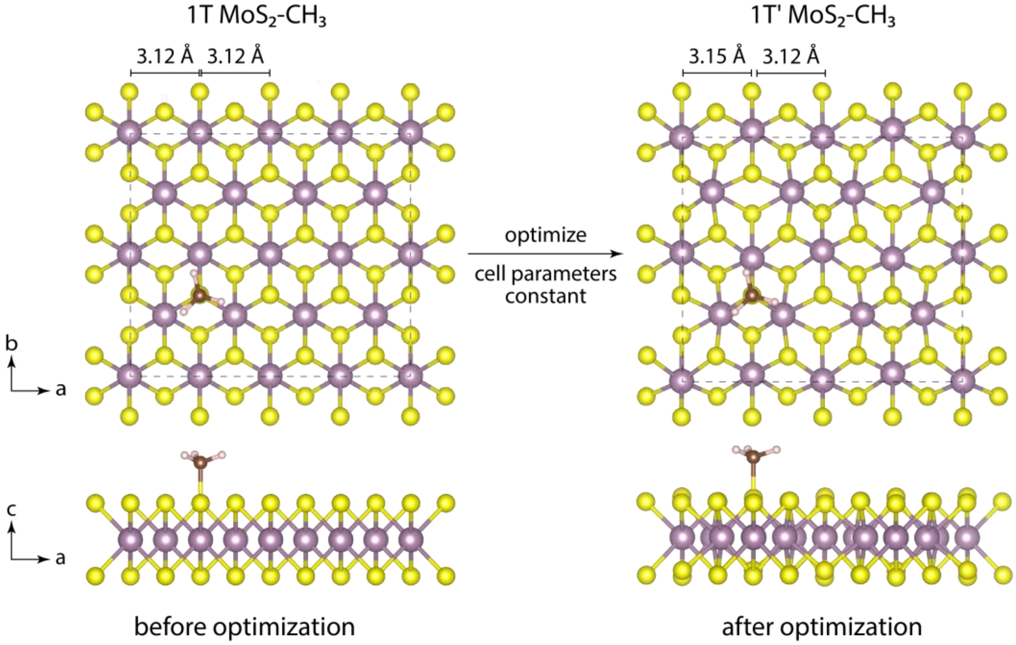

Figure 2.10 Top and side view of 1T-MoS$_2$ methylated on S7 before and after geometry optimization using VASP. A perfect octahedral structure was used for the 1T-MoS$_2$ in the starting structure but became distorted after geometry optimization.

2.3.3 Thermodynamics of progressive methyl functionalization on 1T′-MoS$_2$ as a function of electrochemical potential

The thermodynamics of adding additional methyl groups after the first one was investigated. The notation "*X*N-(*A*)[-[h]*B*]" represents reactions for which *X* is the number of neighbors of the methyl being added, N stands for neighbors, *A*, *B*, etc. are the numbered sulfur positions that are functionalized (see Figure 2.5), an "h" appears next to positions that are high-S, and parentheses "()" appears around the position being functionalized. "Neighbors" are sulfurs that are bound to the same molybdenum as the site of interest that also reside on the same surface of the slab. Thus, each sulfur has 6 neighboring sulfur sites.

Because functionalization preferably occurs on low-S rather than high-S, a low-S site, S7, was functionalized prior to adding the second methyl group. To decide which sulfur to functionalize following the first methyl, the free energies of every 2-methyl functionalization pattern were compared, with one of the methyls on S7 at fixed charge. The methylation patterns with the lowest free energy were 7-5 (i.e., positions S7 and S5 are methylated) and 7-14 (Figure 2.11). This process was repeated to determine the position to functionalize for the 3rd, 4th, 5th, and 6th methyl additions (Figure 2.12 and Figure 2.13).

Figure 2.14 shows the 13 methylation reactions that were selected for study of the thermodynamics based on these calculations.

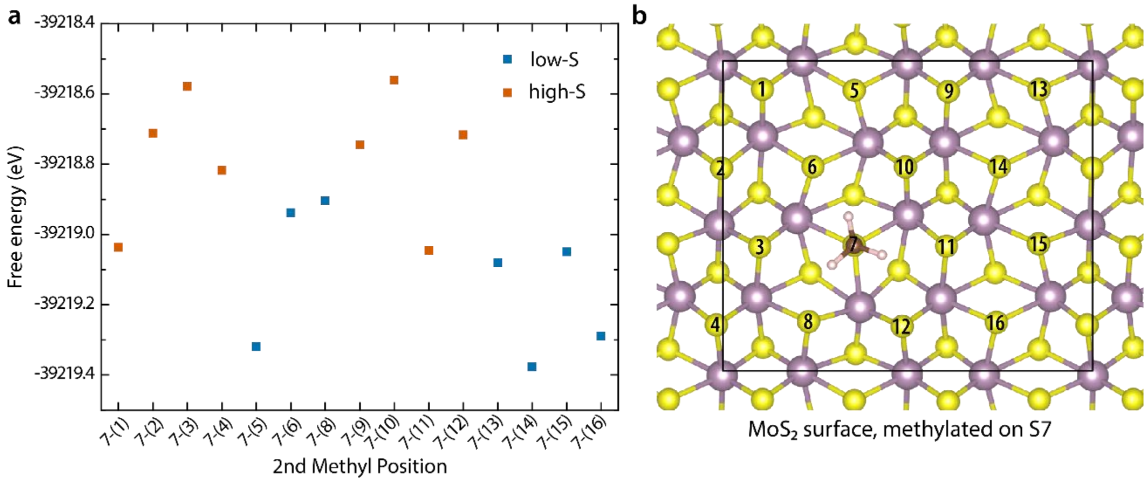

Figure 2.11 Progressive methylation of a surface including one methyl on S7. (a) Free energies of 2-methyl functionalization patterns, minimized with a charge of –2 (Δ*n* = 2) per unit cell. (b) MoS_2 surface prior to the addition of the 2nd methyl. High- and low-S labels refer to the position being methylated.

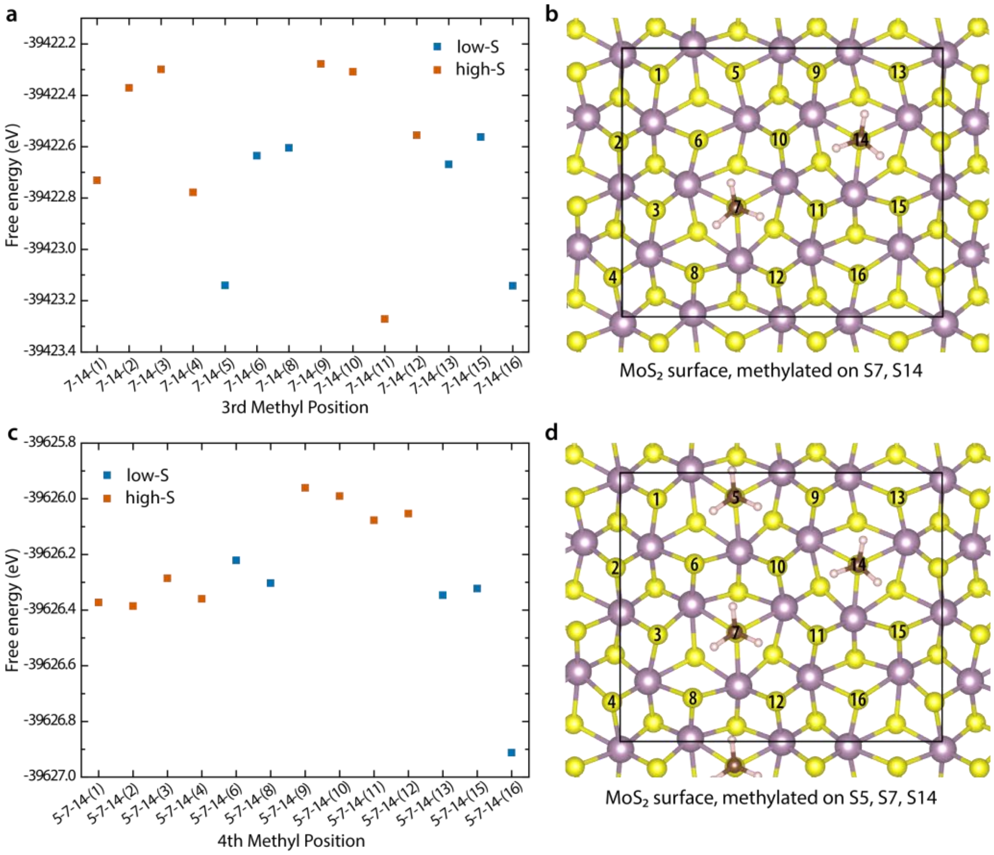

Figure 2.12 Progressive functionalization by addition of a 3rd and 4th methyl group. (a) Free energies of 3-methyl functionalization patterns that include methyls on S7 and S14, minimized with Δ*n* = 2 per unit cell, (b) the MoS_2 surface prior to the addition of the 3rd methyl. (c) Free energies of 4-methyl functionalization patterns that include methyls on S5, S7, and S14, minimized with Δ*n* = 2 per unit cell, (d) MoS_2 surface prior to the addition of the 4th methyl. High- and low-S labels refer to the position being methylated.

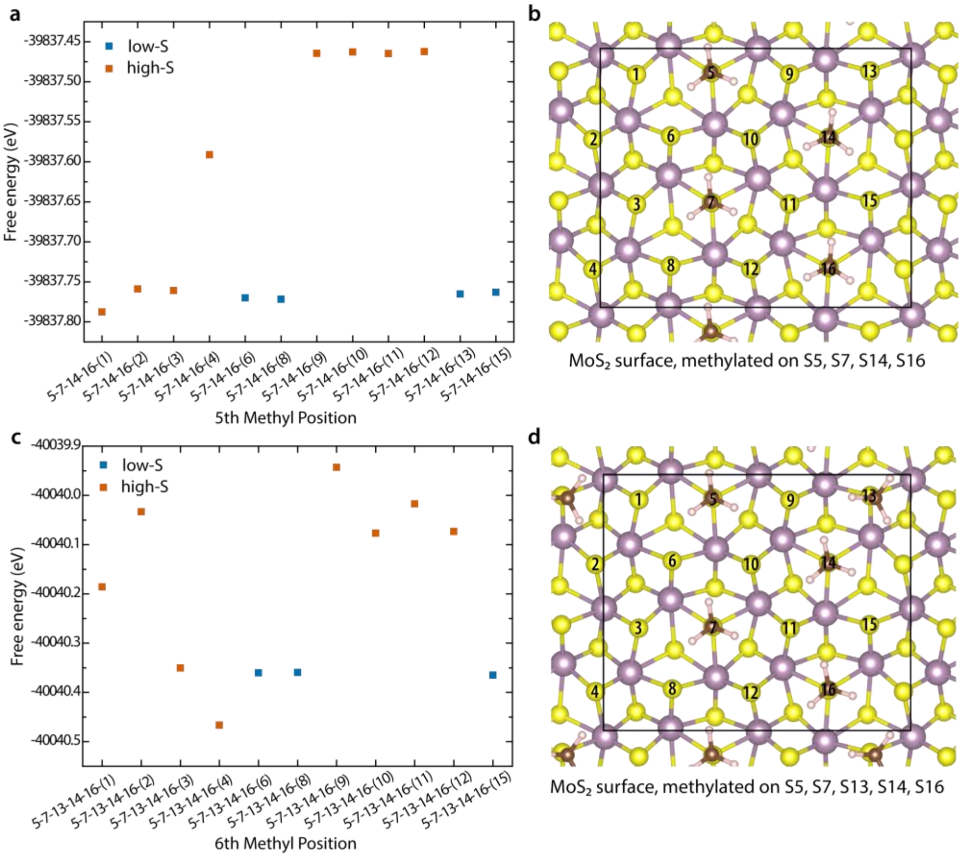

Figure 2.13 Progressive functionalization by addition of a 5th and 6th methyl group (a) Free energies of 5-methyl functionalization patterns that include methyls on S5, S7, S14, and S16, minimized with $\Delta n = -4.2$ per unit cell, (b) the MoS$_2$ surface prior to the addition of the 5th methyl. (c) Free energies of 6-methyl functionalization patterns that include methyls on S5, S7, S13, S14, and S16, minimized with $\Delta n = -4.2$ per unit cell, (d) MoS$_2$ surface prior to the addition of the 6th methyl. High- and low-S labels refer to the position being methylated.

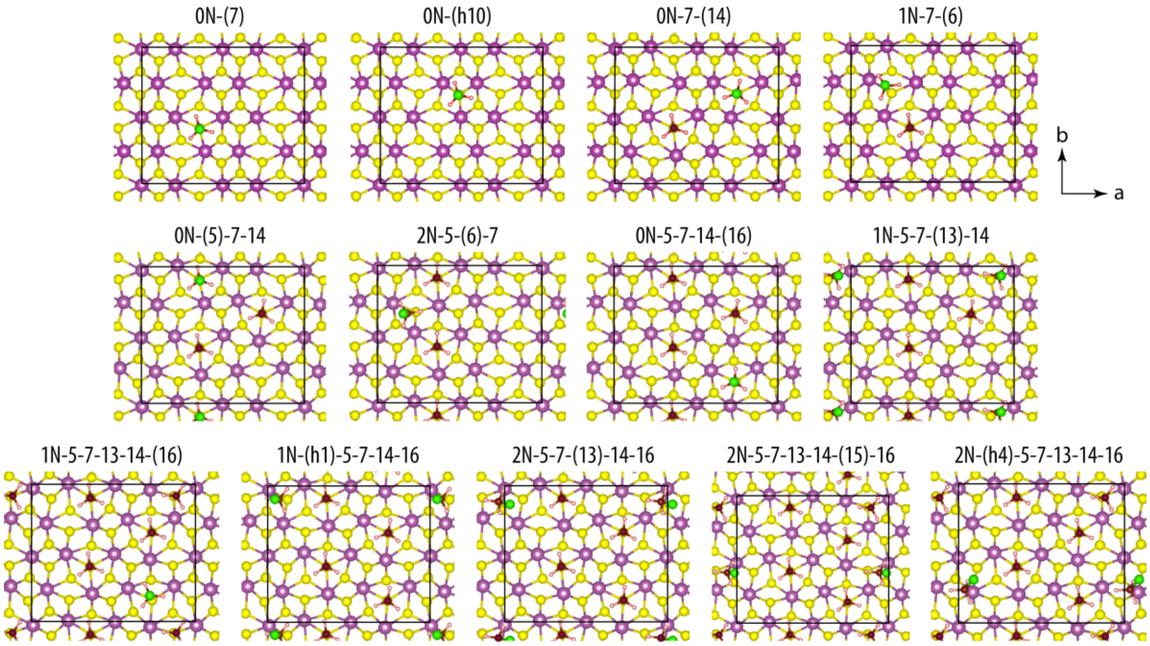

Figure 2.14 Top-down views of the initial states for all functionalization reactions with methyl chloride for which thermodynamic calculations were performed, ordered by the number of methyls on the surface after functionalization then by the number of neighbors next to the methylated position. The labels *X*N represents *X* neighbors next to the methyl being added, the numbers representing the sulfur positions that are methylated, "h" denotes high-S, and parentheses "()" surround the position undergoing the methylation reaction. Structures shown were optimized with Δn = 1.5 per unit cell (except for 2N-5-(6)-7 which was optimized with Δn = 2 per unit cell).

The thermodynamic calculations revealed that the potential of the reaction products became increasingly negative as more methyl groups were added to the surface. Figure 2.15 shows the potential of the MoS_2 slab after each methylation (a chlorine atom is present above the newly added methyl) with Δn = 2 per unit cell. This is consistent with the mechanism, whereby S–C bond formation is expected to increase the number of electrons in the MoS_2 slab. Thus, the calculated decrease in potential with higher coverage supports this mechanism. Additionally, this finding is consistent with experimental studies that demonstrated higher coverages were obtained with stronger reductants since an increasingly negative potential with coverage would decrease the potential difference between the MoS_2 surface and the solution.[81]

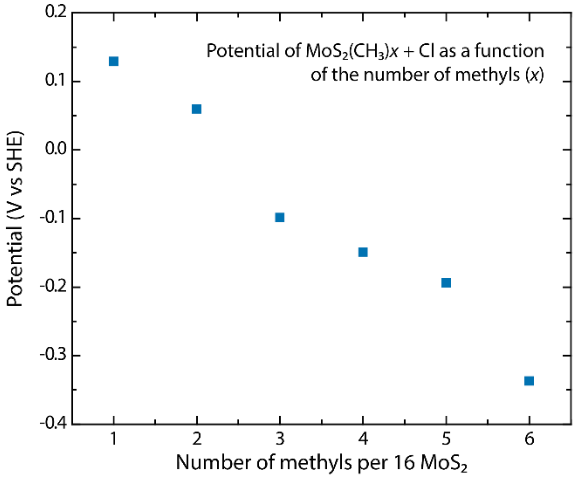

Figure 2.15 Potential in V vs SHE of the final state products $(MoS_2)_{16}(CH_3)_x$ + Cl, with Δn = 2 per unit cell, depending on the number of methyls added to the surface (x = 1, 2, 3, 4, 5 or 6). The potential of the final products becomes more negative as the number of methyls increases due to additional electrons in the system.

Figure 2.16 shows the ΔG as a function of potential for all reactions discussed herein. Methylations that occur surrounded by empty sites (i.e., those labeled 0N) had similar thermodynamic favorability and were thermodynamically more favored than the initial addition of the first methyl group on S7. This behavior is analogous to the vacancy-induced radical functionalization of diazonium on 2H-MoS_2, for which DFT calculations indicated that the initial functionalization reaction can occur only next to a sulfur vacancy, but a functionalized sulfur induces higher reactivity in nearby sulfurs, resulting in a nucleation-propagation functionalization pattern across the surface.[74] A similar mechanism may be present in this system, promoting functionalization of non-sterically-hindered nearby sites. High-S functionalization generally had substantially higher ΔG values than low-S reactions with the corresponding number of neighbors (e.g., 0N-(h10) vs 0N-(7), and 2N-(h4)-5-7-13-14-16 vs 2N-5-7-13-14-(15)-16). An exception is the case of 1N-(h1)-5-7-14-16, which was comparable to 2N and a subset of 1N low-S functionalization reactions.

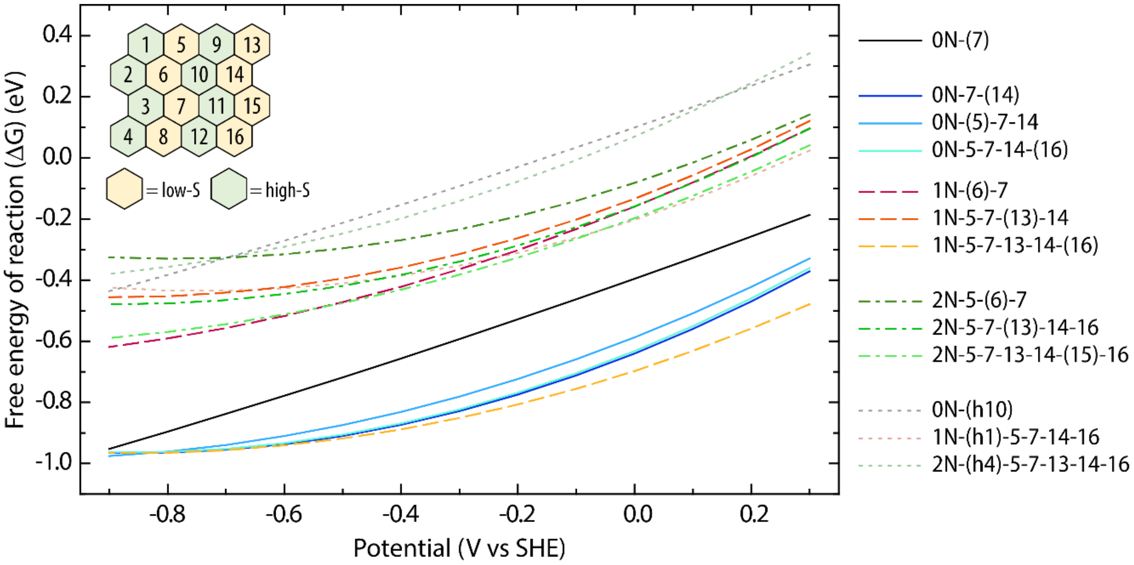

Figure 2.16 The free energy of methylation reactions, ΔG, vs potential for reactions discussed herein. The labels XN represents X neighbors next to the methyl being added, the numbers representing the sulfur positions that are methylated, "h" denotes high-S, and parentheses surround the position undergoing the methylation reaction. Methylation reactions involving 0, 1, or 2 neighboring methyls during the reaction are grouped by color and by solid, dashed, and dashed-dotted lines, while methylation reactions on high-S atoms are grouped using dotted lines.

To identify the cause of the differences in ΔG values, Figure 2.17 compares the grand canonical free energies of the initial and final states at an intermediate potential of –0.1 V vs SHE for each n-methyl reaction, where n denotes the number of functionalized methyl groups in the final state ranging from $n = 2 – 6$. This potential was chosen to avoid interpolation errors at the extremes of the potential range, and also corresponds roughly to the reductant nickelocene, which was used in experimental studies of the reaction.[81] The free energy of the system changes with the number of atoms, so the free energies for each set of n-methyl reactions were referenced to the highest free energy within each n-methyl set to aid the relative comparison of differences in free energy between reactions with different n. 0N, 1N, and 2N comparisons for low-S reactions within each n-methyl set are labeled on the graph. The substantial difference in ΔG between the 0N and 1N/2N reactions is due to the destabilization of the final state for the latter rather than differences in the initial state energies. However, for the 5-methyl reactions, the initial state for the 1N low-S reaction is destabilized relative to the 1N high-S and 2N low-S reactions, both of which have evenly spaced methyl groups (5-7-14-16) in the initial state. The destabilization of the final state of the 1N-5-7-(13)-14 reaction consequently translates into a destabilized initial state for the 1N-5-7-13-14-(16) reaction.

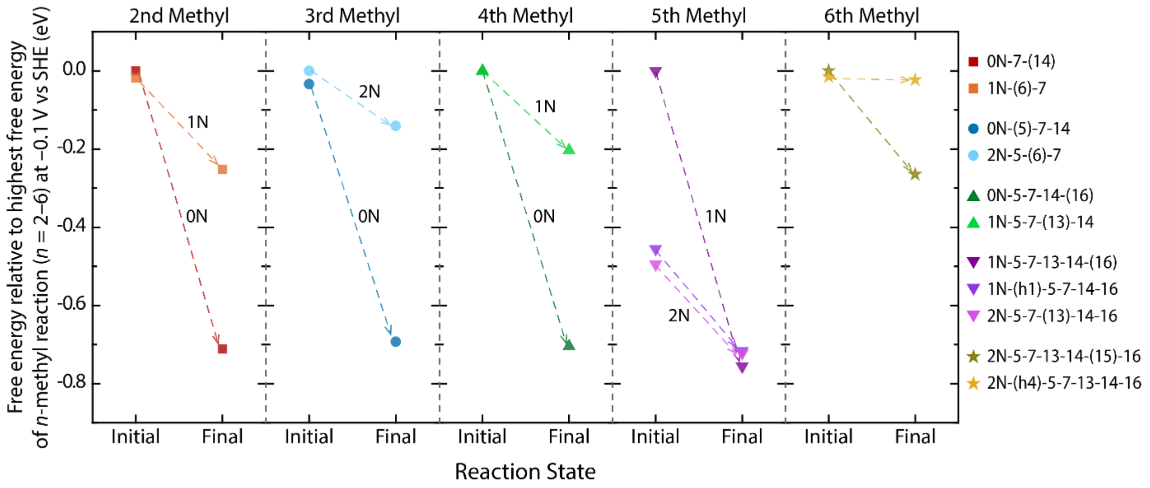

Figure 2.17 Free energy of initial and final states of *n*-methyl reactions relative to the highest free energy within each set of *n*-methyl reactions, where *n* = 2, 3, 4, 5, or 6 and describes the total number of methyl groups present in the final state. The labels *X*N represents *X* neighboring methyl groups present on the slab next to the sulfur position to which an *n*th methyl is being added. The numbers represent the sulfur positions that are methylated, where "h" denotes high-S, and parentheses indicate the sulfur position undergoing the methylation reaction.

Within the potential range of 0.3 to –0.9 V vs SHE, the Δ*G* for 0N, 1N and 2N reactions on low-S were between –0.4 to –1.0 eV, 0.1 to –1.0 eV, and 0.3 to –0.6 eV, respectively (Figure 2.16). At any specific potential, overlap was present between the 1N and 2N reactions but not between 0N and 2N reactions.

Figure 2.18 displays the ΔG required to add one methyl via a progressive stepwise addition from 6% to 94% coverage per MoS_2. These energies were calculated using VASP free energy structural minimization using Δ*n* = 0 as well as single-point jDFTx where the potential was held constant at -0.86 V vs SHE to mimic the experimental condition of cobaltocene-activated methylation. Free energy structural minimization of the MoS_2 pattern with 100% coverage per MoS_2 unit resulted in convergence issues, so those functionalization patterns are not included in this work. Three distinct regions were observed from 6% to 31%, 31% to 56%, and 56% to 94% coverage per MoS_2 unit where the difference in ΔG to add a single methyl becomes more positive. These trends indicate that the reaction to add another methyl becomes less thermodynamically favorable and may provide an explanation for the experimentally observed coverage limits. Without the addition of a reductant, methyl coverages are limited to <25-30% per MoS_2 unit,[12,85] which corresponds well with the upper limit of the first ΔG region in Figure 2.18. At the upper limit of the second region, ΔG becomes significantly more positive by 1.33 eV and begins to rise sharply after 69% per MoS_2 unit, corresponding well to the experimentally observed upper coverage limit of ~70% per MoS_2 unit in cobaltocene-activated methylation.[81]

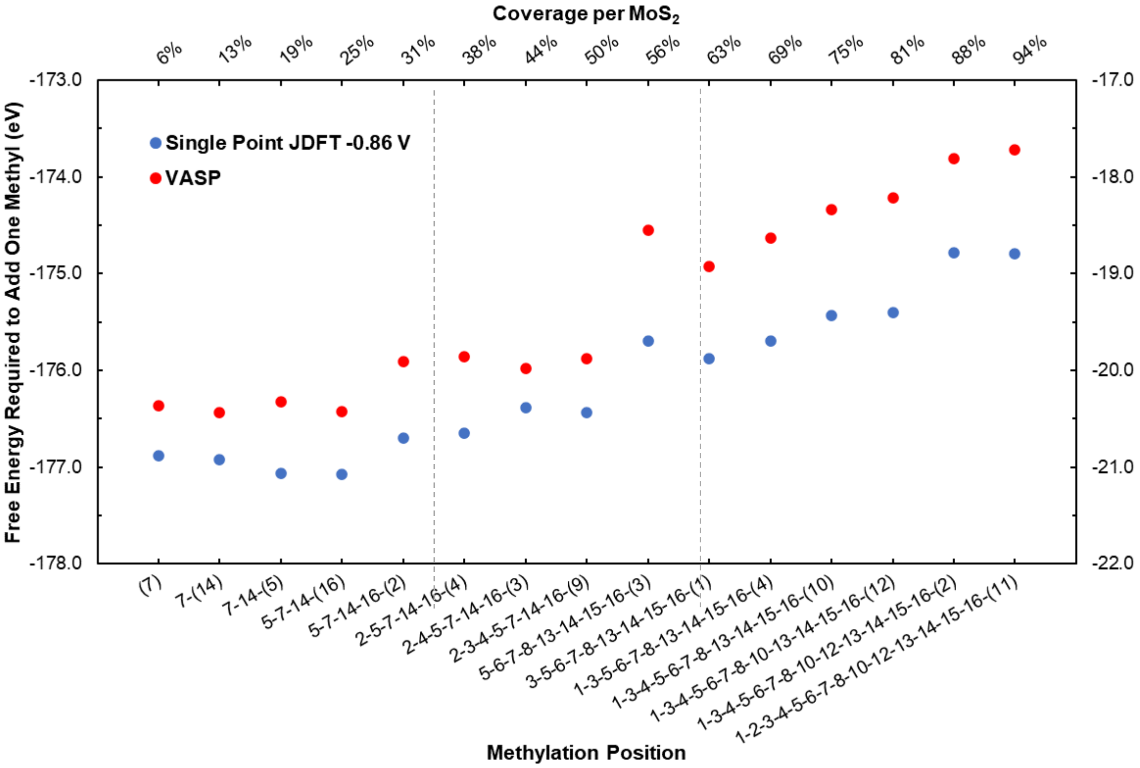

Figure 2.18 Free energy (ΔG) required to add one methyl during progressive methylation. Red circles denote the free energies achieved using VASP free energy structural minimization with Δ*n* = 0 (right y-axis), and blue circles represent the free energies obtained with single point JDFT when the electrochemical potential is held constant at -0.86 V vs SHE (left y-axis). Dotted lines separate the three ΔG regions of interest where a notable positive increase is observed.

2.3.4 Effects of neighboring methyl groups on the rotational barrier of methyls

Aside from the thermodynamics and kinetics of the methylation reaction, we also studied how the number of neighbors impacts the rotational barrier of methyl groups on 1T′-MoS_2. Methyl groups with higher rotational barriers suggest that rotation occurs with lower probability and thus the conformation is more restricted. If we assume that the kinetics of a reaction depends on the likelihood for the reactants' conformation to meet the conformation limitations in the products, then the rotational barrier of the functional group in the final product may be correlated to the likelihood for the reaction to take place at that location.

We computed the rotational barrier for seven cases of low-S methyl rotation using NEB at fixed charge. In four cases, the rotating methyl had 0 neighbors, in two cases, the rotating methyl had 1 neighbor, and in the remaining two cases, the rotating methyl had 2 neighbors. We will use the following notation to convey the surface conformation and the rotating methyl: *X*N-*A**[-*B*], where *X* is the number of neighbors of the rotating methyl, N stands for neighbors, *A*, *B*, etc. are the sulfur positions that are functionalized and can have more or fewer positions as appropriate, and the asterisk (*) appears next to the position of the rotating methyl. Four examples of this notation are shown in Figure 2.19. The numbering of sulfur atoms is consistent with Figure 2.5.

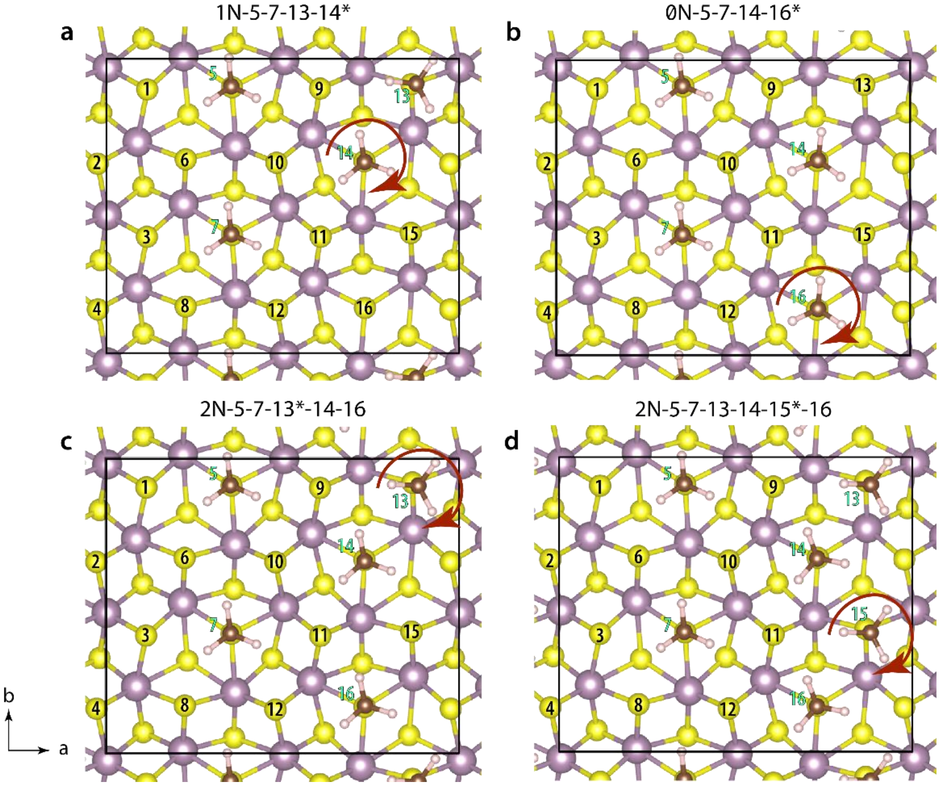

Figure 2.19 Examples of methyl patterns and the corresponding notation to indicate the pattern and the rotating methyl. (a) Example where the rotating methyl has one neighbor, (b) an example where the rotation methyl has 0 neighbors, (c) and (d) are examples where the rotating methyl has 2 neighbors. Note that positions 13 and 16 are adjacent due to the periodic repeat of the unit cell.

Figure 2.20 plots the rotational barriers of various examples organized by the number of neighbors adjacent to the rotating methyl, from 0 to 2. From Figure 2.20, we observe a distinct increase in the rotational barrier for methyl groups with 0 or 1 neighbors compared to methyls with 2 neighbors, with the latter doubling in the barrier height from ~0.05 eV to ~0.1 eV.

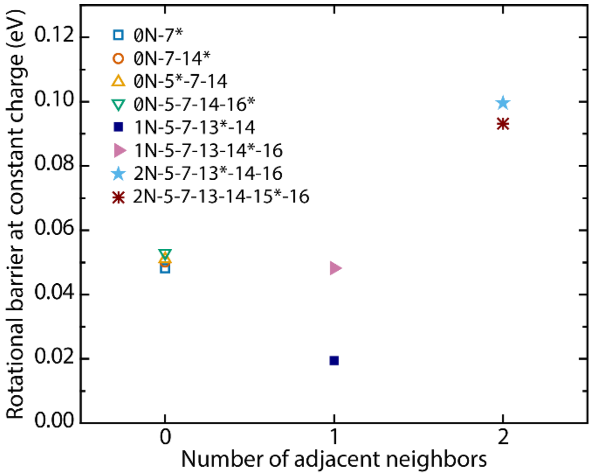

Figure 2.20 The rotational barrier for clockwise methyl rotation by 120 ° of various methyl patterns as a function of the number of neighbors adjacent to the rotating methyl. The unique methyl rotation case is specified in the legend notation as *X*N-*A[-*B*] where *X* is the number of neighbors next to the rotating methyl, *A*, *B*, etc. are the positions with methyls, and the asterisk (*) indicates the rotating methyl.**

One apparent outlier to discuss is for the 1-neighbor (1N) cases. For 1N-5-7-13-14*-16 where the rotating methyl is at the end of a group of 3 methyls in a row, the barrier height is close to those of the 0N cases at ~0.05 eV, whereas the 1N-5-7-13*-14 case where the rotating methyl is one of 2 methyls in a row resulted in a much lower barrier of 0.02 eV. This discrepancy in rotational barrier between these two 1N examples may be due to a combination of 2 factors: (1) destabilization of the most stable conformation for 1N-5-7-13*-14 relative to 0N rotations due to strain from the adjacent S13 and S14 positions, and (2) destabilization of both the stable and unstable conformations for 1N-5-7-13-14*-16 relative to 0N rotations, resulting in a similar net difference between these states (i.e., rotational barrier) compared to 0N rotations. Since 1N-5-7-13-14*-16 has 3 adjacent methyls (S13 is adjacent to S16) whereas 1N-5-7-13*-14 only has 2 adjacent methyls (S13 and S14), the S13 methyl in the former case cannot accommodate the S14 methyl rotation due to steric hinderance from the S16 methyl on the other side of S13, whereas in the latter case, the S14 methyl has no other neighbors and can accommodate the S13 methyl rotation during the rotational barrier. The relative destabilization of the rotational trough relative to 0N cases and stabilization of the rotational peak relative to 1N-5-7-13-14*-16 results in a relatively low rotational barrier for 1N-5-7-13*-14. Note that 5-7-13-14 is not the thermodynamically favored pattern for 4 methyl groups on the surface; the thermodynamically most favorable pattern is one where all methyl groups are evenly spaced, such as 5-7-14-16, which is also plotted (0N-5-7-14-16*) and has a 0.05 eV rotational barrier. From Figure 2.21 we can see that both the stable and unstable conformations for 1N rotations are destabilized relative to 0N rotations, and only the unstable conformation is destabilized for the 5-methyl examples with the same methylation pattern on the surface.

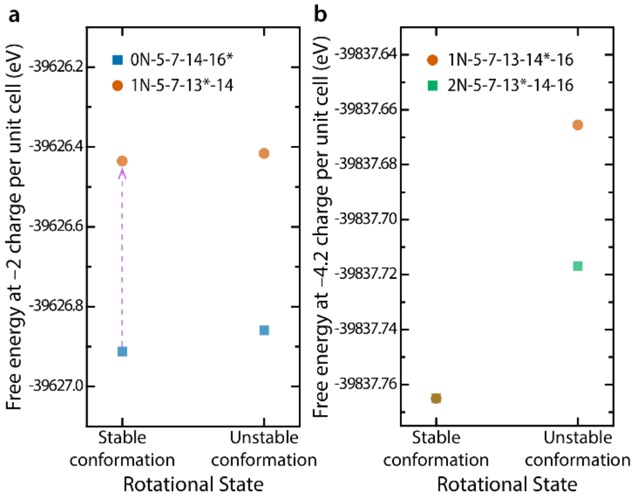

Figure 2.21 Free energies of the stable (trough) and unstable (peak) conformations during methyl rotation for (a) 4-methyl examples with 0- and 1-neighbors during rotation with arrow indicating destabilization of the 1-neighbor stable conformation, and (b) 5-methyl examples with 1- and 2-neighbors during rotation.

Another comparison is between the middle vs outermost methyl groups in a row of 3 methyl groups in the two cases with the same 5-methyl pattern (5-7-13-14-16): the rotational barrier for the middle of 3 adjacent methyls (S13) is 0.10 eV, as in 2N-5-7-13*-14-16, whereas the rotational barrier is 0.05 eV for the outermost of 3 adjacent methyls (S14), as in 1N-5-7-13-14*-16. This shows that although the outermost methyls in a row of 3 restrict the rotation of the middle methyl, the outermost methyls are not themselves restricted because of the additional space they can use to accommodate the rotation. In the extreme case where there are no "outermost methyls" to speak of, such as in 2N-5-7-13-

14-15*-16 where all low-S sulfurs within the same column are functionalized, the rotational barrier is 0.09 eV, similar to the barrier for the middle of 3 adjacent methyls (2N-5-7-13*-14-16) discussed above.

2.3.5 Models of expected coverage under various constraints

The DFT calculations performed thus far on the 4×4 1T′-MoS_2 surface would be significantly cost- and time-intensive to extend to more realistic depictions of the surface which require a substantially larger unit cell. Furthermore, numerous functionalization patterns are possible where a sulfur site with free energy closely matching the sulfur site with minimum free energy is methylated instead, producing a chain effect on the progressive methylation process where other sulfur sites are preferentially functionalized. Performing rigorous DFT analysis on each possible functionalization pattern is out of the scope of this work. Thus, five functionalization models were used to simulate random surface functionalization on a 100×100 MoS_2 surface and were constructed based on the two observations discussed above (sections 2.3.2 and 2.3.3). First, the thermodynamics and kinetics of functionalizing low-S is much more favorable than functionalizing high-S sites when both have 0 neighbors, and secondly, the thermodynamics of methylation, ΔG, for 0-neighbor reactions are substantially more favorable than 1- and 2-neighbor reactions. Also, the rotational barriers for 2-neighbor methyl groups are twice as high (0.1 eV) as the barriers for 0- and 1-neighbor methyl groups (0.05 eV), suggesting that the conformation of the transition state during a 2-neighbor methylation is more constrained and thus less likely to occur (Section 2.3.4). The coverage of methyl groups on MoS_2 was accordingly estimated assuming random surface functionalization based on the constraints of each model. Python was used to simulate the random functionalization of a surface that proceeded until no more valid reactions were available, given a set of constraints. Each simulation used a 100×100 2-D array to represent the sulfur surface and contained both high- and low-S sites (Figure 2.22). The coverage distribution and expected coverage values are based on N = 2000 simulations for each model. The goal of these simulations was to arrive at non-trivial expected lower and upper bounds for coverage that are greater than 0% and less than 100% per MoS_2, because 100% exceeds the experimentally observed coverage and would not be a useful comparison.[39] The code for all simulations discussed in this section can be found in the Appendix.

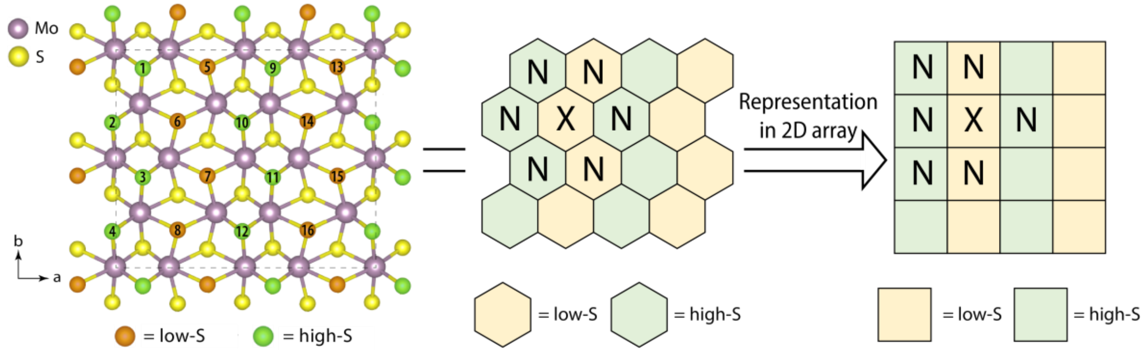

Figure 2.22 Illustration of how the layout of low-S and high-S on 1T′-MoS_2 and the neighbors surrounding each site were translated into the corresponding grid locations in the coverage simulations.

The first model, called “0-neighbor max low-S,” contained the most restrictive set of constraints. The functionalization constraint was that only low-S can be functionalized, and no neighboring functional group could be present relative to the position being considered for functionalization. Any of the 6 neighbors of each sulfur site were considered neighbors in the simulation.

The second and third models were the “global 1-neighbor max low-S” and “local 1-neighbor max low-S” models. Both models restrict functionalization to low-S but differ in that the “global” model constrained each reaction such that at most 1 neighbor could be adjacent to *any* functional group on the surface in the final state, whereas the “local” model requires that at most 1 neighbor could be adjacent only to the position being functionalized. As a result, the local model could potentially produce chains of functional groups if each addition occurred at the outermost position of the chain, whereas this result would not be possible with the constraints of the global model.

The fourth model is the “local 1-neighbor max” model, which allowed both high- and low-S positions to be functionalized and required that the functionalization position had at most only 1 neighbor. The fifth model, the “2-stage local 1-neighbor max” model, simulated functionalization of the surface in two stages. The first stage followed the constraints of the “0-neighbor max low-S” model, and the second stage followed the constraints of the “local 1-neighbor max” model. This 2-stage approach was of interest because the experimental reductant-activated functionalization results were obtained using a two-step approach to functionalization, with the reductant added in the second step.[39]

Figure 2.23 shows histograms of the coverage distributions resulting from these five models with $N = 2000$. The most restrictive model, the “0-neighbor max low-S” model, resulted in an average coverage of 43.5 ± 0.2% per MoS_2. The least restrictive model is the “local 1-neighbor max” model, which resulted in an average coverage of 75.3 ± 0.3%. Results for models that allowed up to 2 neighbors for any functional group are not presented because these constraints would allow all low-S to be functionalized (each low-S has 2 low-S neighbors) and thus any 2-neighbor model would result in a coverage of at least 100%.

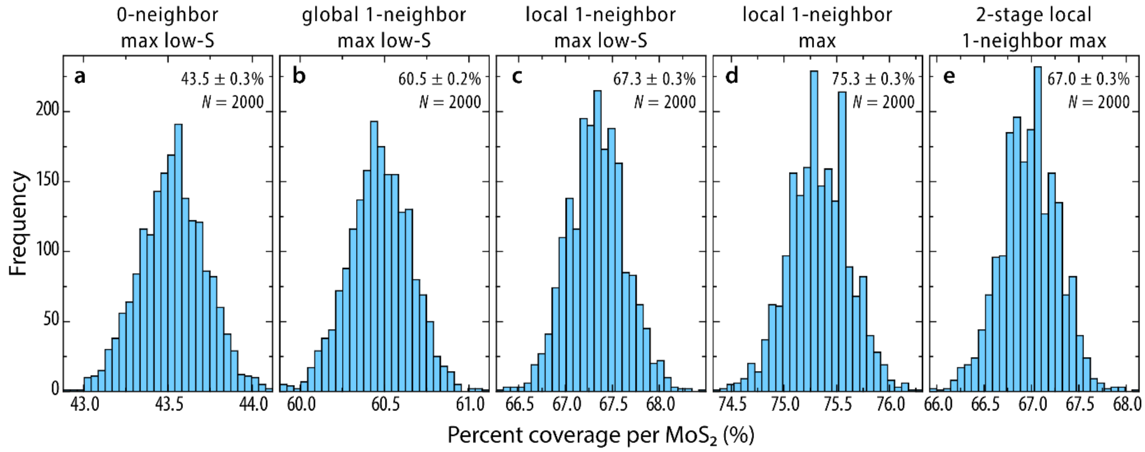

Figure 2.23 Histograms of the coverage distributions from simulations of the random functionalization of a 100×100 grid ($N = 2000$, 30 bins) of five models and the resulting average and standard deviations of coverage per MoS_2: (a) the “0-neighbor max low-S” model that only allows functionalization on positions surrounded by empty sites, (b) the “global 1-neighbor max low-S” model that allows functionalization for low-S positions if the result has no more than 1 neighbor adjacent to any group on the surface, (c) the “local 1-neighbor max low-S” model that allows functionalization for low-S position if it has at most 1 neighbor at the time of addition, (d) the “local 1-neighbor max” model that allows functionalization for any position if it has at most 1 neighbor at the time of addition, and (e) the “2-stage local 1-neighbor max” model functionalizes the surface first according to the 0-neighbor max low-S model, then according to the local 1-neighbor max model.

Table 2.1 lists the simulation coverage distributions for the five sets of constraints discussed above. In the DFT calculations of the thermodynamics of 0-neighbor methylation reactions, the ΔG did not substantially change as the number of methyl groups on the surface increased. This behavior suggests that “0-neighbor max low-S” models the lower bound of the expected coverage distribution for monolayer 1T′-MoS_2 if (a) the surface can be functionalized with at least 1 functional group, and (b) functional groups more than 2 positions away or more from the reaction site do not interfere in the reaction. The simulated coverage of 43.5% per MoS_2 produced by this model matched well with experimental observations of ~40% methyl coverage on chemically exfoliated MoS_2. Further, the maximum coverage for propyl groups using reductant-activated functionalization with a strong reductant was ~44%.[39] The propyl groups are substantially larger sterically than methyl groups and thus are more sterically hindered. Thus, on chemically exfoliated MoS_2 this model may represent an upper limit for the propyl coverage, but a lower limit for the methyl coverage.

Table 2.1 Simulated coverage per MoS_2, expressed as an average and standard deviation. The theoretical results were obtained using simulations based on different requirements for the allowed number of neighbors on a local vs global scale, on low-S vs high-S, and functionalized through a 1- vs 2-stage process.

Model Algorithm Name	Model Functionalization Constraints	Coverage per MoS_2 (100×100, $N = 2000$)
0-neighbor max low-S	No functionalization on high-S nor positions adjacent to functionalized positions	43.5 ± 0.2%
global 1-neighbor max low-S	No functionalization on high-S; at most one neighbor next to any functional group	60.5 ± 0.2%
local 1-neighbor max low-S	No functionalization on high-S; at most one neighbor next to the position being functionalized	67.3 ± 0.3%
local 1-neighbor max	At most one neighbor next to the position being functionalized	75.3 ± 0.3%
2-stage local 1-neighbor max	Functionalize surface according to 2 algorithms applied sequentially per slab: First stage: same as 0-neighbor max Second stage: same as local 1-neighbor max	67.0 ± 0.3%

With less restrictive models that still resulted in < 100% coverage, the expected coverages ranged from 60 to 75%. The most restrictive of these models, "global 1-neighbor max low-S", required that no methyl group on the surface had more than 1 neighbor and was included for completeness. This model seems unlikely to be the operating mechanism, however, based on DFT calculations discussed previously which indicate that 1-neighbor reactions that result in methyl groups with 2 neighbors, such as 1N-5-7-13-14-(16), can be more thermodynamically favorable than even 1-neighbor reactions that result in at most 1 neighbor for each methyl, such as 1N-(6)-7 or 1N-5-7-(13)-14. The least restrictive model short of allowing up to 2 neighbors, "local 1-neighbor max" allowed functionalization on both low- and high-S from the initial stages of the reaction. The models that explore fractional coverages with 1 neighbor gave an expected upper bound for *ce*MoS_2 coverage of ~75%. The highest coverage observed experimentally on *ce*MoS_2 is ~70%.[81] Given the large variation in ΔG for the 1N reactions as shown in Figure 2.16 and Figure 2.17, the 1-neighbor maximum models give an upper bound that captures a range of 1N reactions, some of which are much more favored than others.

2.3.6 Exploration of the steric hinderance of propyl-functionalized 1T′-MoS_2

Reductant-activated functionalization studies using methyl iodide and propyl iodide to functionalize *ce*MoS_2 found that the coverage of propyl groups was consistently lower than that of methyl groups at constant potential.[81] The highest propyl coverage achieved was ~44% using cobaltocene and propyl iodide to functionalize *ce*MoS_2. Since this coverage is lower than the maximum coverage of ~70% achieved using methyl iodide under the same conditions, the lower coverage of propyl groups appears to be due to increased steric hinderance induced by propyl groups' larger size, as opposed to other possibilities such as the availability of charge. We performed DFT calculations for various propyl functionalization patterns on 1T′-MoS_2 to illustrate the favored packing density of propyl groups by optimizing the structures for propyl-functionalized MoS_2 with 1, 2, 3, or 4 propyl groups on a 4×4 1T′-MoS_2 basal plane.

Similar to the case of progressive methyl functionalization, starting from unfunctionalized MoS_2, we functionalized MoS_2 with one propyl group at a time, and minimized the structures for all possible propyl functionalization patterns using the most energetically stable structure for subsequent functionalizations. Starting with the first propyl, we minimized low-S- and high-S-functionalized propyl-MoS_2 on S6, S7, S10, and S11 and found that the free energies for high-S-functionalized MoS_2 are ~0.5 eV higher in free energy compared to the low-S-functionalized MoS_2, similar to the observations for the placement of methyl groups, as shown in Figure 2.24.

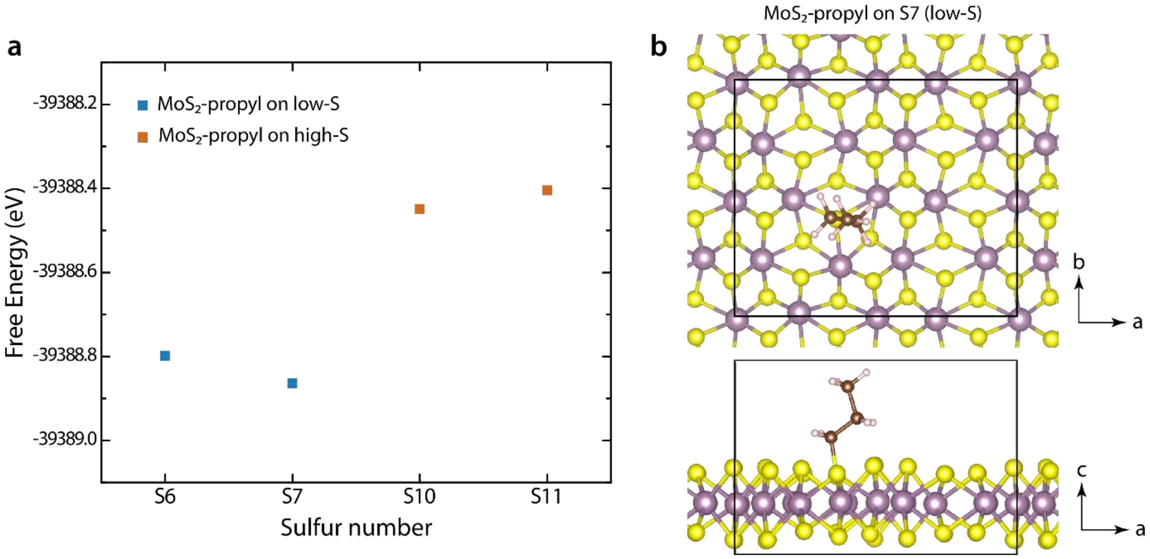

Figure 2.24 Addition of a single propyl to 1T′-MoS_2 surface. (a) Free energy of the MoS_2 slab functionalized on S6, S7, S10, or S11, optimized with $\Delta n = 1.5$ per 16 MoS_2. S6 and S7 are low-S, S10 and S11 are high-S. A substantial difference can be seen between the S6- or S7-functionalized MoS_2 compared to the S10- and S11-functionalized MoS_2. (b) Top-down and side view of the S7-functionalized MoS_2-propyl structure.

For the second propyl group, we started with the first propyl group on S7 and placed the second propyl on each of the other sulfurs in turn and minimized the structures with a constant charge of –1.5 (Δn = 1.5) per unit cell. The MoS_2 with propyl groups on S7 and S13 was found to be the lowest-energy structure (Figure 2.25). Similarly, for the third and fourth propyl groups, we found the positions S5 and S15 to be the most favorable low-S positions (Figure 2.26). Table A.2 contains the free energies and potentials for all structures discussed here. To be able to compare these structures at constant potential, several additional structures at different charges would need to be minimized for each structure, which was not performed for this work.

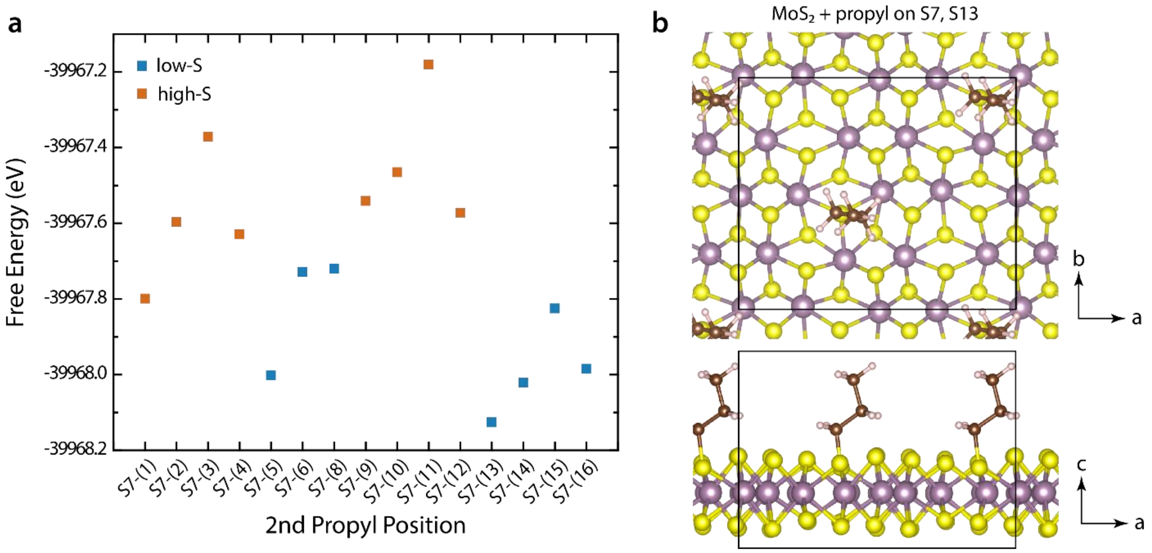

Figure 2.25 Addition of a 2nd propyl to 1T′-MoS$_2$ surface. (a) Free energy of the MoS$_2$ slab functionalized on S7 and one other position for all combinations, optimized with Δ*n* = 1.5 per unit cell (16 MoS$_2$). (b) Top-down and side view of the lowest-energy 2-propyl-functionalized MoS$_2$ structure functionalized on S7 and S13.

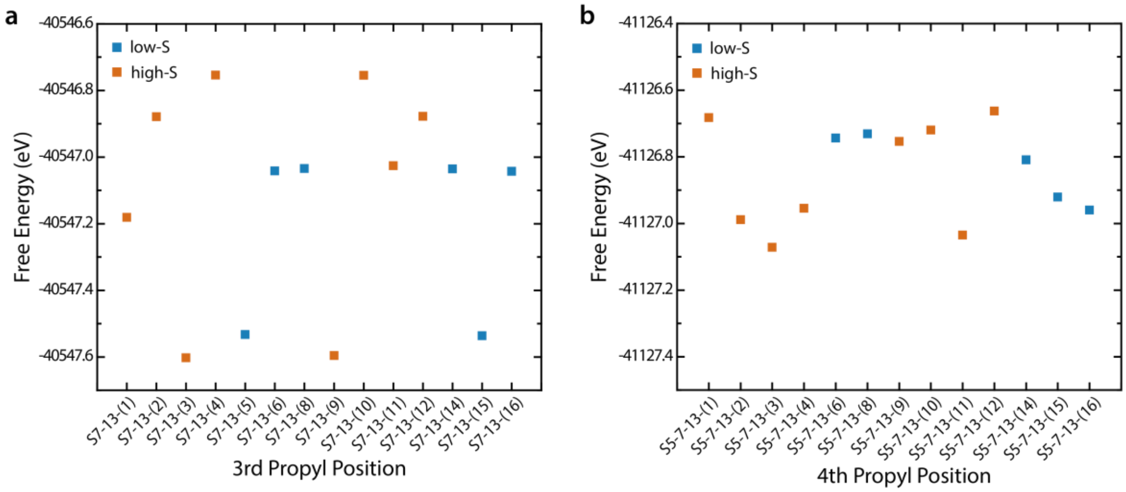

Figure 2.26 Free energies for functionalized MoS$_2$ (a) 3-propyl and (b) 4-propyl structures optimized with Δ*n* = 1.5 per unit cell (16 MoS$_2$) using VASP and single point energy calculated using jDFTx with CANDLE solvation. High- and low-S labels refer to the position being functionalized. Values plotted here are also provided in Table A.2.

Functionalizing only low-S positions, after 4 propyl groups, the functionalized positions are S5, S7, S13, and either S15 or S16. With S5, S7, S13, and S15, the propyl groups are evenly spaced as shown in Figure 2.27 and adopt a similar conformation to the first propyl group, which did not have any neighbors. However, for positions adjacent to functionalized sulfurs such as S16, the newly added propyl group is rotated to accommodate the propyl on S15. Alternative placements where the fourth propyl is placed on either a high-S sulfur that appeared to be thermodynamically favorable (S3) or a less favorable low-S sulfur (S14) are also shown in Figure 2.27. An alternative evenly-spaced propyl placement S5–S7–S14–S16 may have been the likely outcome if the second propyl group was placed on S14 or S16 instead of S13, such as in the methyl case. Note that the range of free energies from adding the 1st, 2nd, 3rd, and 4th propyl groups goes from 0.46 eV, to 0.95 eV, to 0.85 eV, to 0.41 eV, indicating that for the 4th propyl, there is less driving force to differentiate between the favorable and unfavorable positions compared to the 2nd and 3rd propyl additions.

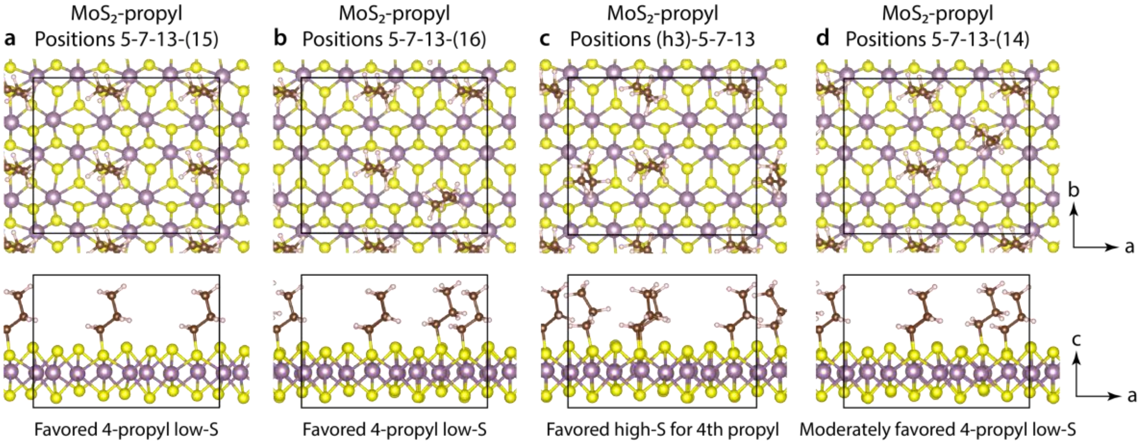

Figure 2.27 Four 4-propyl patterns to illustrate conformation of propyl groups (see Figure 2.26 and Table A.2 for free energies) with the 4th propyl position in brackets: (a) and (b) the most energetically favored 4-propyl pattern functionalized only on low-S, (c) the most energetically favored 4-propyl pattern with the 4th propyl on a high-S (S3), and (d) a moderately favored 4-propyl pattern functionalized only on low-S. Other than evenly spaced propyl groups as in (a), the fourth propyl is rotated in all other examples to accommodate for neighboring groups.

Given that we found the thermodynamics of reaction to be substantially less favored for methyl groups with two neighbors compared to zero, and methyl groups are substantially smaller than propyl groups, we believe it is unlikely that the steric hinderance of propyl groups allows for adjacent functionalized positions experimentally. Here, we have presented only a preliminary guide for future work evaluating the thermodynamics and kinetics of propyl functionalization.

2.4 Conclusions

Grand Canonical Density Functional Theory (GC-DFT) calculations for the methylation of 1T′-MoS_2 with methyl chloride predict that: (1) the thermodynamics and kinetics of methylation are more favorable as the electrochemical potential decreases, (2) the methylation of low-S sites is more favored both thermodynamically and kinetically compared to methylation of high-S sites in comparable environments; and (3) methylation of sulfur sites with no adjacent methyl groups appears to be substantially more thermodynamically favorable than methylation of sites with 1 or more neighbors. These results are all consistent with experimental observations that show an increase in coverage with increasing reductant strength. The theoretical study helps explain experimental observations that the maximum methyl coverage on chemically exfoliated MoS_2 in the presence of an electron donor appears to be ~70% per MoS_2. Simulating the random addition of functional groups on a 1T′-MoS_2 surface according to the subset of constraints that result in between 0 and 100% coverage per MoS_2 based on the number of nearest neighbors, high- vs low-S, and 1- vs 2-stage, suggests an expected coverage of ~44% for the lower and ~75% for the upper bound. Our investigation centered heavily on categorizing sites according to the sulfur type (low-S vs high-S) and the number of neighboring functional groups. Additionally, the correlations made between the simulations and experimental observations assume a dominance of monolayer MoS_2 for the synthesized *ce*MoS_2.

In the next chapter, we extend this reductant-activated electrophilic addition reaction to Si(111), a group 14 material with dramatically different electronic and structural properties. We will explore the effect of reductant strength, reductant concentration, and treatment time on surface reactivity.

Chapter 3 – Reductant-activated Surface Functionalization of Silicon(111)

3.1 Introduction

Silicon (Si) is an attractive semiconductor material for wide-ranging applications, from electronics and sensing to solar cells.[36–45] The device properties of Si can be manipulated through control over the structure and chemical composition of crystalline Si surfaces.[101,102] Self-assembled monolayers (SAMs) have been widely utilized to tailor the properties and functionality of Si surfaces for a desired application.[38,101–103] SAMs composed of strong and nonpolar C–Si linkages provide superior chemical stabilization of the Si surface against oxidation and deleterious surface states, as compared to SAMs bonded to the surface through weak or polar bonds, such as Si–X (X = Cl, I, H, N, O).[38,104] Numerous synthetic routes have been developed to functionalize Si surfaces since the formation of C–Si alkyl monolayers reported by Linford and Chidsey.[23] Starting from a freshly etched hydrogen-terminated Si(111) surface (H–Si(111)), C–Si bonds are can be introduced via a hydrosilylation reaction with unsaturated hydrocarbons (alkenes or alkynes)[24–27] or by a two-step chlorination/alkylation sequence, proceeding through a chlorine-terminated Si(111) surface (Cl–Si(111)) as an intermediate state.[28,29] Borane-catalyzed hydrosilylation on hydrogen-terminated silicon nanocrystals[105] and carbene insertions on H–Si(111) have also yielded C–Si bonds.[30] In addition, C–Si linkages have been produced by electrografting with unsaturated hydrocarbons and diazonium salts,[31,32] by scanning probe-induced cathodic electrografting with alkynes,[33] and by electrochemical derivatization of silicon surfaces by Grignards.[34] Methyl termination, formed by the two-step chlorination/alkylation reaction, provides excellent electronic passivation that resists degradation due to oxidation. Moreover, alkylation modifies the surface electronic structure by creating a surface dipole that effectively changes the electron affinity of the Si surface, resulting in modifications of the charge-transfer kinetics across Si/metal or Si/electrolyte junctions.[35]

Oxidant-activated addition of nucleophiles to planar and nano-crystalline Si surfaces has also been recently reported.[6,106] A wide range of nucleophiles, including alcohols, amines, thiols, carboxylic acids, and phosphines, can be covalently grafted onto H–Si surfaces in the presence of one-electron metallocene oxidants. Mechanistic investigations suggest that oxidant-activated reactions proceed through oxidation of the H–Si surface, followed by a nucleophilic attack. Hence, the position of the oxidation potential relative to the Si Fermi level plays an important role in determining the overall reactivity. Furthermore, reductant-activated functionalization of MoS_2 nanosheets with small molecule electrophiles has been realized using one-electron metallocene reductants.[81] The surface coverage of the MoS_2 nanosheets is partially governed by the redox potential of the metallocene reductants that controls the amount of negative charge stored in the nanosheets.

We report herein the reductant-activated addition of organic electrophiles to H–Si(111), broadening the understanding of the range of redox-activated addition reactions of Si. The analogy to the oxidant-activated nucleophilic addition suggests that reactivity trends should be sensitive to the position of the reduction potential relative to the Si Fermi level, which is close to the Si conduction band minimum (CBM), $\mathbf{E}_{\mathrm{CBM}}$ = -4.17 eV, for n-type Si and in the middle of the Si band gap for intrinsic Si.[6,44,106] The CBM of the material increases in energy with decreasing physical dimensions of the crystal in moving from bulk Si to nanoparticles. With the increase in the band gap with decreasing bulk dimensions, stronger reductants are required to activate electrophilic additions. The limiting case for Si would be the reactivity of molecular silanes such as $((CH_3)_3Si)_3Si\text{-}H$[6] that we do not expect to react by reductant-activated reactions.

The investigated reactions of acrylic acid (AA) and methyl acrylate (MA) with the H–Si(111) surface utilize metallocene-based reductants that span a wide range of reduction potentials. The proposed mechanism, illustrated in Figure 3.1, involves the injection of charge into the conduction band of the Si surface from a molecular reductant with a sufficiently negative reduction potential. The reduction of the Si surface activates an H–Si bond. The activated Si reacts with the end carbon of the α,β-unsaturated carbons of the solution-based molecule in an electrophilic-type addition reaction, resulting in the formation of a surficial C–Si bond to the AA or MA.[107–110] The formation of the C–C single bond is coupled with a surface hydrogen abstraction for balanced stoichiometry. This work expands our understanding on the utility of CB-initiated covalent surface functionalization processes, as opposed to photoexcitation of the Si surface, where transient charge injection into the CB promotes transient binding that leaves the surface intact.

We have investigated the reductant-activated addition of AA as a function of reductant concentration and reaction time for octamethylnickelocene ($(Me_4Cp)_2Ni$), cobaltocene (Cp_2Co), and decamethylcobaltocene ($(Me_5Cp)_2Co$). This series of one-electron outer-sphere redox species was selected to systematically span the range of electrochemical potentials, from 0.03 eV ($(Me_4Cp)_2Ni$) to 0.89 eV ($(Me_5Cp)_2Co$) above the Si CBM in MA (Figure 3.1) and to allow characterize of surface activation by electrophilic addition.[44,111] For the analogous oxidant-activated nucleophilic addition, oxidants with reduction potentials more negative than the potential of the Si valence band minimum were unable to activate the surface toward addition.[6,106] Thus, metallocenes with reduction potentials more positive that the potential of the Si CBM were not included in this study. The concentration range of the reductants used in this study was chosen to ensure an accessible reaction rate for surface functionalization from earlier experiments over a range of metallocene concentrations.[106]

Reductant-activated addition of MA was observed with nickelocene (Cp_2Ni), $(Me_4Cp)_2Ni$, and $(Me_5Cp)_2Co$. Use of AA and MA as electrophiles enables detection and characterization of the resulting functionalized surfaces by standard surface characterization techniques, such as X-ray photoelectron spectroscopy (XPS), Fourier transform infrared (FTIR) spectroscopy, and variable-angle spectroscopic ellipsometry. Moreover, the incorporation of reactive moieties in SAMs, such as various carbonyls, is not readily achieved in a single reaction step using commonly employed H-Si(111) hydrosilylation methodologies. The synthetic route presented in this work offers a convenient alternative for addition of reactive functional groups to the surface with short reaction times at room temperature and without use of specialized equipment.[39,112,113] Such moieties can later be utilized to anchor functional materials to the Si(111) surface, which may be beneficial for photovoltaic, sensor, and catalysis applications, among others.[114,115]

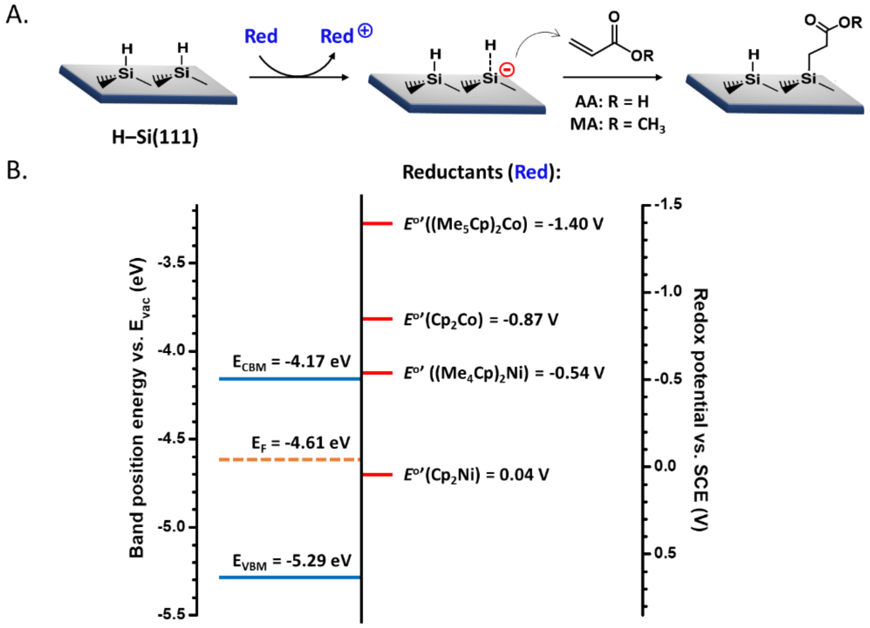

Figure 3.1 Reductant-activated addition of electrophiles to H–Si(111). (A) Proposed mechanism for the reductant (Red)-activated addition of acrylic acid (AA) and methyl acrylate (MA) to H–Si(111). (B) Energy diagram showing the positions of the Si valence-band maximum (E_{VBM}), Si conduction-band minimum (E_{CBM}), and calculated bulk Fermi level (E_F) for the Si used vs. the vacuum level (E_{Vac}). The measured formal reduction potentials ($E^{\circ\prime}$) vs SCE in MA of the molecular reductants (Red) used are indicated relative to the Si band positions.[116] The reduction potentials are aligned with the Si band energies by assuming that the absolute one electron potential of SCE is at -4.69 eV.

3.2 Experimental

3.2.1 Materials

All solvents and reagents were purchased commercially and used as received, unless stated otherwise. Aqueous buffered hydrofluoric acid (BHF(aq)) and aqueous ammonium fluoride (NH$_4$F(aq), 40% semiconductor grade) were purchased from Transene Co. Inc. NH$_4$F(aq) was deaerated by bubbling with Ar(g) (99.999%, Airgas) for ≥1 h prior to use. Dichloromethane (anhydrous 99.8%, Sigma-Aldrich) was deaerated by bubbling with Ar(g) for ≥1 h and was stored in a nitrogen (N$_2$)-purged glovebox (<5 ppm of O$_2$(g)) prior to use. Acrylic acid (AA, anhydrous 99%, Sigma-Aldrich) was degassed by three consecutive freeze-pump-thaw cycles and stored in a N$_2$-purged glove box prior to use. Methyl acrylate (MA, anhydrous 99%, Alfa Aesar), decamethylcobaltocene ((Me$_5$Cp)$_2$Co, bis(pentamethylcyclopentadienyl)cobalt(II), 98%, Sigma-Aldrich), cobaltocene (Cp$_2$Co, bis(cyclopentadienyl)cobalt(II), 98%, Sigma-Aldrich), octamethylnickelocene

($(Me_4Cp)_2Ni$, bis(tetramethylcyclopentadienyl)nickel, 98%, Alfa-Aesar), and nickelocene (Cp_2Ni, bis(cyclopentadienyl)nickel(II), 98%, Sigma-Aldrich) were stored in an argon (Ar)-filled glovebox (< 2 ppm O_2 (g)) prior to use. Float-zone-grown, phosphorus-doped n-Si(111) "intrinsic" wafers (University Wafer, Boston, MA) were double-side polished, 450 ± 10 μm thick, oriented within 0.5° of the (111) crystal plane, and had a resistivity of 5.0–5.5 kΩ·cm. Deionized water (≥18.2 MΩ·cm resistivity) was obtained from a Barnstead E-Pure system.

3.2.2 Preparation of hydrogen-terminated Si(111) surfaces

For transmission mode IR analysis, Si wafers were scored using a diamond-tipped scribe and broken into ~ 1.3 cm × 3.2 cm pieces. The Si surfaces were sonicated for 10 min sequentially with methanol (≥99.8%, BDH) and water, and then were dried under a stream of Ar(g). The samples were oxidized in a piranha solution consisting of a 3:1 (v/v) ratio of 18 M sulfuric acid (95–98% v/v, ACS Grade, EMD) to 8.8 M (30 wt % in H_2O) hydrogen peroxide (ACS grade, EMD) using a heated water bath at a temperature of 95 ± 5 °C. After etching in the piranha solution, the substrates were thoroughly rinsed with copious amounts of water and immersed for 18 s in BHF(aq). Anisotropic etching was then performed for 9 min in an Ar(g)-purged solution of 40% NH_4F(aq), resulting in atomically flat H–Si(111) surfaces.[24,117] The wafers were removed, rinsed with water, and dried under a stream of Ar(g).

3.2.3 Reductant-activated addition of electrophiles to hydrogen-terminated Si(111)

The H–Si(111) wafers were transferred to a N_2(g)-purged glovebox and immersed in neat AA or MA solutions that contained 2.0 mM, 5.0 mM, or 10.0 mM of the reductant (Cp_2Ni, $(Me_4Cp)_2Ni$, Cp_2Co, or $(Me_5Cp)_2Co$). Solutions were prepared by gentle manual shaking prior to introduction of the wafers. Reactions were performed in glass test tubes for 10-60 minutes at room temperature without additional stirring. Upon completion of the reaction, the wafers were rinsed with CH_2Cl_2, removed from the glovebox in sealed CH_2Cl_2-filled test tubes, sonicated for 10 min, and dried under a stream of Ar(g).

3.2.4 Methyl ester-terminated Si(111) hydrolysis

Si(111) surfaces functionalized with MA were subjected to acidic ester hydrolysis to form carboxylic acid-terminated Si(111) surfaces. The functionalized wafers were immersed in 1.0 M sulfuric acid and heated to 35 ± 5 ^{o}C for 24 h in a sealed pressure vessel. The wafers were removed from the solution, rinsed with copious amounts of water, and dried under Ar(g).

3.2.5 Instrumentation

Transmission infrared spectroscopy (TIRS) was performed using a Thermo Scientific Nicolet 6700 optical spectrometer equipped with an electronically temperature-controlled EverGlo mid-IR source, a KBr beam splitter, a deuterated l-alanine-doped triglycine sulfate (DLaTGS) detector, and a N_2(g) purge. The samples were mounted using a custom attachment such that the angle between the path of the beam and the surface normal was 74° (Brewster's angle for Si). The reported spectra are averages of 1500 consecutive scans collected at 4 cm^{-1} resolution. Spectra were referenced to a spectrum of a Si wafer that was covered with silicon oxide (SiO_x). Data were collected and processed using OMNIC software, version 9.2.41. The baseline was flattened, and residual water and CO_2 peaks were subtracted to produce the reported spectral data.

X-ray photoelectron spectroscopic (XPS) data were collected using a Kratos AXIS Ultra spectrometer and a Surface Science M-probe ESCA/XPS. The Kratos AXIS Ultra spectrometer was equipped with a monochromatic Al Kα X-ray source at 1486.7 eV, a hybrid electrostatic and magnetic lens system, and a delay-line detector (DLD). The photoelectron-ejection vector was 90° with respect to the sample surface plane. The electron collection lens aperture was set to sample a 700 × 300 μm spot. Survey and high-resolution spectra were collected with an analyzer pass energy of 80 and 10 eV, respectively. The chamber base pressure was $< 9 \times 10^{-9}$ Torr. The instrument energy scale and work function were calibrated using clean Au, Ag, and Cu standards. The instrument was operated by Vision Manager software v. 2.2.10 revision 5 and data were analyzed using CasaXPS software (CASA Software Ltd). The Surface Science M-Probe system had a chamber base pressure of $< 2 \times 10^{-9}$ Torr. Data were acquired using the ESCA25 Capture (Service Physics, Bend OR; V5.01.04) software. A monochromatic x-ray source illuminated the sample with 1486.7 eV Al Kα radiation that was directed at 35° to the sample surface. collected Photoelectrons were collected by a hemispherical energy analyzer with a 100 mm radius and a pass energy of 50 eV. The analyzer had a resolution of ~ 0.8 eV and a takeoff angle of 90° with respect to the sample surface. Data were evaluated using CasaXPS software (CASA Software Ltd).

High-resolution C 1*s*, O 1*s*, and Si 2*p* XPS data were analyzed using CasaXPS version 2.3.16. C 1*s* spectra were fitted using a Voigt GL(30) line function, which consisted of 70% Gaussian and 30% Lorentzian character. Bulk Si 2*p* data were fitted using a line function of the form LA(*a*, *b*, *n*), where *a* and *b* define the asymmetry of the line shape and *n* defines the Gaussian width. LA(1.53, 243) was used in this work. Contributions from surface silicon species and SiO_x were fitted using the GL(30) line shape. Spectra were analyzed using a linear background. All spectra were internally calibrated to the energy of the C 1*s* emission of the major adventitious emission (285 eV) following the precedent for analysis of Si(111).[6,81,106] Residual STD for C 1*s* and O 1*s* spectra was between 0.9 – 1.0, and 1.9 – 2.6 for Si 2*p*.

Surface-bound layer thicknesses were measured using a J.A. Woollam Alpha-SE variable-angle spectroscopic ellipsometer. The measurements were performed using a standard (10 s) data acquisition period over a 380-900 nm wavelength range and at incidence angles of 65° and 70°. The thickness of the layers was modelled with CompleteEASE software, using the “Si with transparent film” model. The functionalized surfaces were measured at ≥ 2 locations.

3.2.6 Determination of formal potentials and Si Fermi level

The formal potentials of the reductant species (10.0 mM) in MA were determined by cyclic voltammetry (CV) vs. $Cp_2Fe^{+/0}$, using a glassy carbon working electrode (3 mm diameter), a quasi-reference electrode formed from $Ag^{+/0}$ in acetonitrile, a Pt counter electrode, and 0.10 M tetra(n-butyl)ammonium hexafluorophosphate ($TBAPF_6$, Sigma-Aldrich) as the supporting electrolyte. The glassy carbon electrode was freshly polished before each measurement. The CVs were recorded at room temperature in a N_2-filled glovebox (OMNI-LAB, VAC), using a SP-200 potentiostat (Bio-logic). All CVs were electronically compensated using positive-feedback iR-compensation for 85% of the R_u, as determined by the ZIR technique at open-circuit potential.[118] The scan rate for all CVs was 25 mV s^{-1}. Formal reduction potentials ($E°'$) vs SCE ($E°'(Cp_2Fe^{+/0})$ = 0.455 V vs. SCE) were converted to absolute potentials using a value of −4.44 V for the absolute electrochemical potential of the standard hydrogen electrode (SHE) at 25 °C, and the redox potential of SCE vs. SHE (+0.24 V),[106,119] using equation 1:

$$E°' \text{ vs. vac} = -\,(E°' \text{ vs. SCE}) - 4.68\text{ V}. \quad (1)$$

The formal potentials of the reductants in AA were not determined due to large (80 kΩ) solution resistances in this electrolyte.

The Si Fermi level was determined using equation 2:

$$\mathbf{E}_{\mathrm{F}} = \mathbf{E}_{\mathrm{CBM}} + k_{\mathrm{B}}T\ \ln\left(\frac{N_d}{N_c}\right). \quad (2)$$

$\mathbf{E}_{\mathrm{CBM}}$ is the energy position of the Si conduction band minimum (–4.17 eV vs. E_{vac}). k_{B} is Boltzmann's constant, T is the temperature in Kelvin (296 K), N_{d} is the dopant density as determined from the Si resistivity (8.8×10^{11} cm^{-3}), and N_{c} is the effective density of states in the Si conduction band (2.8×10^{19} cm^{-3}).

3.3 Results and Discussion

3.3.1 Addition of Acrylic Acid to Si(111) surfaces

Figure 3.2 demonstrates the reactivity trend of the H–Si(111) surface towards AA as a function of the reduction potential of the one-electron redox species that promotes the surface functionalization process. Freshly-etched H–Si(111) exhibits a characteristic ν(H–Si) signal at 2083 cm^{-1} (Figure 3.2a).[106,117] The inverted absorbance bands at 1231 cm^{-1} and 1060 cm^{-1} correspond to the longitudinal and transverse optical modes, associated with ν(Si–O–Si),[120] and derive from the oxide-terminated Si(111) used as a reference. H–Si(111) surfaces, treated for 60 min with AA in the presence of 2.0 mM $(Me_5Cp)_2Co$ (Figure 3.2b) or Cp_2Co (Figure 3.2c), exhibited absorbance bands indicative of the resulting propionic acid-functionalized surface and acrylic acid polymerization products.[108,109] The absorbance band centered at 1717 cm^{-1} corresponds to the ν(C=O) mode of the carboxylic acid group and decreased with decreasing reductant strength. Two additional signals at 1455 cm^{-1} and 1411 cm^{-1} (Figure 3.2b) are ascribed to δ(Si–CH_2) and δ(O–H), respectively, and provide further indication of the nature of the functionalized surface and the covalent C–Si bond formation. The characteristic ν(C=O) band is absent after surface treatment with $(Me_4Cp)_2Ni$ as the reductant (Figure 3.2d) or in neat AA (Figure 3.2e). The functionalization reaction displaces the hydrogens bonded to the Si(111) surface as indicated by the reduction of 37% - 47% in the intensity of the sharp ν(H–Si) absorption. However, the H–Si bond is unstable, which makes quantitative comparison of its signal intensity difficult and impacts the observed intensity of both the initial hydride-terminated surface and the functionalized surface.[121] Treatment with increasing concentrations (5.0 mM, 10.0 mM) of $(Me_4Cp)_2Ni$ for 60 min did not result in covalent binding of AA to Si(111), as evidenced by the absence of the ν(C=O) signal in the TIRS spectra (Figure 3.3). Shorter $(Me_4Cp)_2Ni$ treatments were therefore not evaluated. Acidic conditions (*i.e.*, AA solution) produce a positive shift in the reduction potential of metallocenes),[111] placing the effective reduction potential of $(Me_4Cp)_2Ni$ below the Si CBM, consistent with the lack of observed reductant-activated addition under such reaction conditions (Figure 3.4).

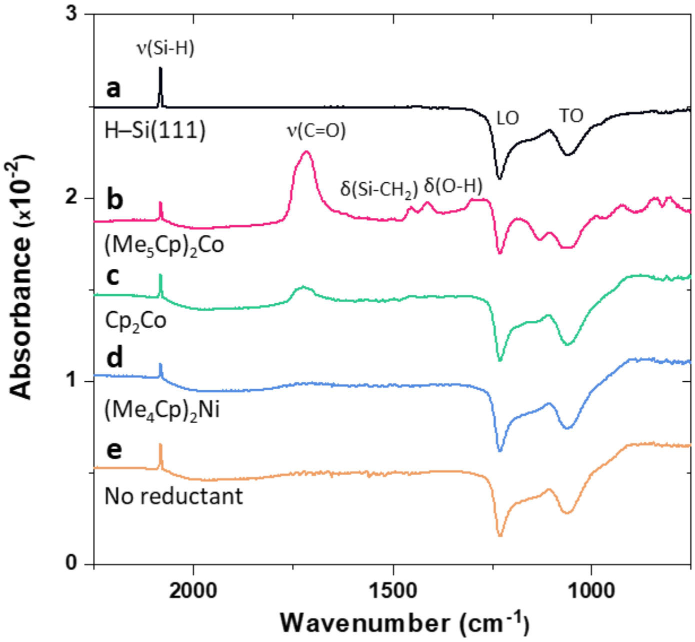

Figure 3.2 TIRS data for H–Si(111) surfaces (a) after a 60 min treatment in acrylic acid (AA) solution containing 2.0 mM of (b) $(Me_5Cp)_2Co$, (c) Cp_2Co, (d) $(Me_4Cp)_2Ni$, (e) or no reductant. The spectra are offset vertically for clarity.

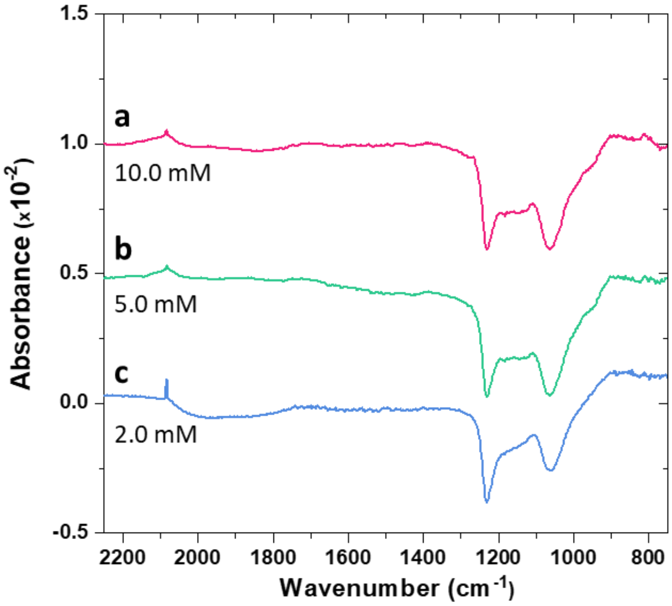

Figure 3.3 TIRS data for H–Si(111) surfaces after 60 min of reaction in acrylic acid (AA) solution containing 10.0 mM (a), 5.0 mM (b), or 2.0 mM (c) of (Me4Cp)2Ni. The spectra are offset vertically for clarity.

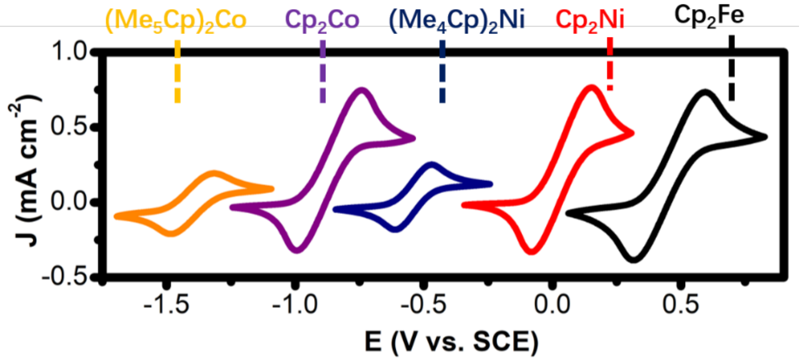

Figure 3.4 Comparison of cyclic voltammograms (CVs) for decamethylcobaltocene (orange), cobaltocene (purple), octamethylnickelocene (blue), nickelocene (red), and ferrocene (black) dissolved in methyl acrylate (MA) with 0.1 M $TBAPF_6$ supporting electrolyte. The concentrations of cobaltocene, nickelocene and ferrocene are 10 mM. Formal reduction potentials were converted from V vs. $Cp_2Fe^{+/0}$ to V vs. SCE using $E^{o'}(Cp_2Fe^{+/0})$ = 0.455 V vs. SCE. Lower current density observed for methyl-substituted metallocenes are due to their lower solubility. Scan rate: 25 mV s^{-1}.

To further characterize the effect of the $(Me_5Cp)_2Co$ and Cp_2Co reductants on the electrophilic addition reaction to H–Si(111), the reductant concentration (2.0-10.0 mM) and the surface treatment time (10-60 min) were both varied. Figure 3.5 shows the TIRS spectra of H–Si(111) surfaces treated with 5.0 mM (Figure 3.5C and D) or 10.0 mM (Figure 3.5A and B) AA solutions of $(Me_5Cp)_2Co$ (Figure 3.5A and C) or Cp_2Co (Figure 3.5B and

D). Increases in the reaction time resulted in a substantial increase in the ν(C=O) peak intensity. For longer reaction times (30 min for Cp_2Co and 20 min for $(Me_5Cp)_2Co$), increases in the concentration of reductant, from 5.0 mM to 10.0 mM, resulted in a substantial increase in the ν(C=O) peak intensity, whereas no substantial difference was observed for shorter reaction times (20 min for Cp_2Co and 10 min for $(Me_5Cp)_2Co$). For both reductant concentrations, the stronger reductant, $(Me_5Cp)_2Co$, produced higher intensity ν(C=O) peaks after 20 min of reaction than were observed after 30 min of reaction with Cp_2Co. Consistently, 10 min of reaction $(Me_5Cp)_2Co$ produced similar intensity ν(C=O) peaks to those observed after 20 min of reaction with Cp_2Co.

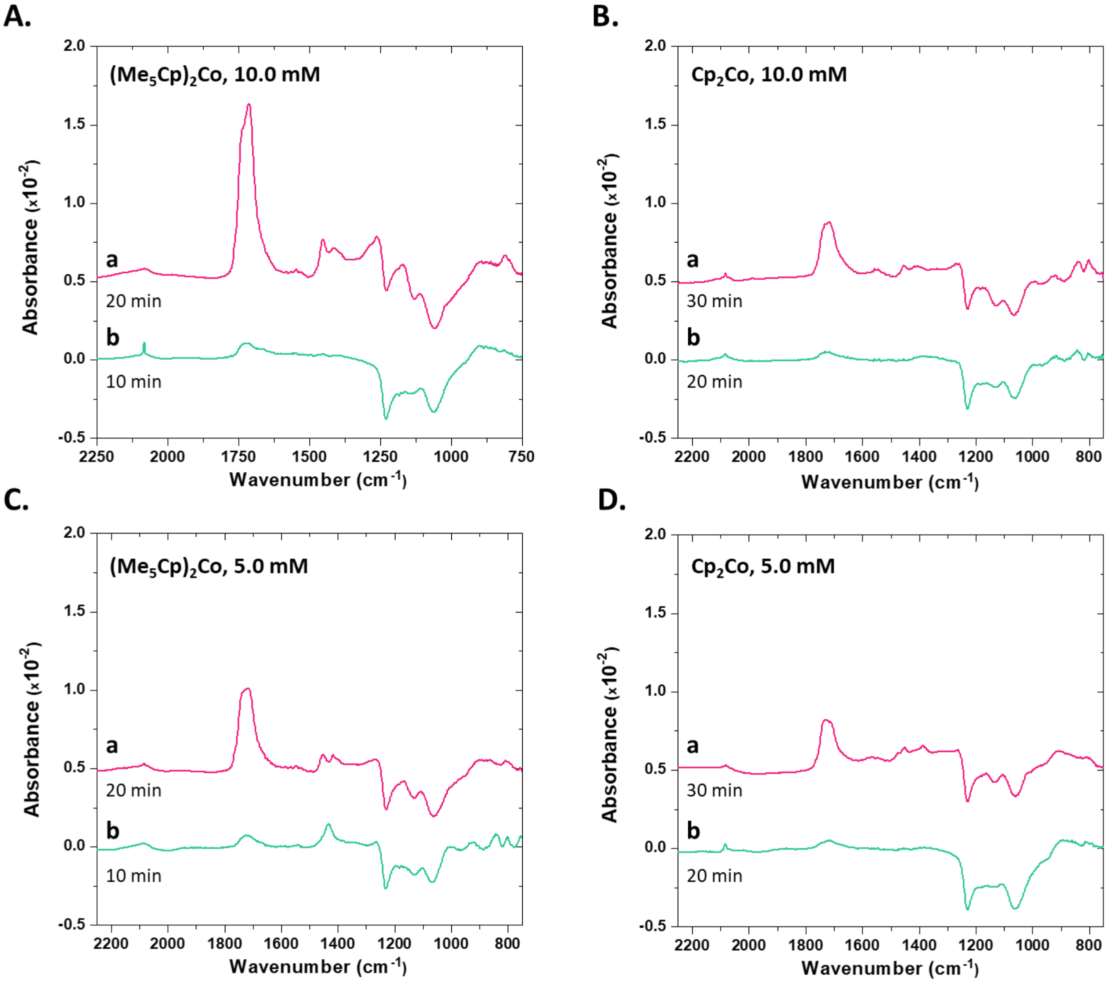

Figure 3.5 TIRS data for H–Si(111) surfaces after treatment in acrylic acid (AA) solution containing: (A) 10.0 mM $(Me_5Cp)_2Co$, (B) 10.0 mM Cp_2Co, (C) 5.0 mM $(Me_5Cp)_2Co$, and (D) 5.0 mM Cp_2Co. Surface treatment times varied between (a) 20-30 min and (b) 10-20 min for different reductants. The spectra are offset vertically for clarity.

XPS was used qualitatively to corroborate the formation of C–Si bonds and characterize the composition of the functionalized surface. In the Si XP spectra, the Si–H emission is obscured by that of Si–Si; however, in the C spectra the C-Si emission only partially overlaps that of adventitious carbon. This overlap prevented a quantitative surface coverage analysis rather representative XP spectra are presented. Figure 3.6 displays a XP spectrum of a surface-bound layer formed by treating H–Si(111) with a 10.0 mM AA solution of $(Me_5Cp)_2Co$ for 10 min. The high-resolution C 1*s* spectrum (Figure 3.6B) had a peak at 284.2 eV with a FWHM of 0.87 eV indicative of formation of a covalent C–Si bond by the reductant-activated electrophilic addition of AA to H–Si(111).[102,109]

A Monte Carlo simulation of the C 1s XP spectrum (Figure 3.7) was used to estimate the errors in the fitting and test the reproducibility. The STD of the fit was compared with the residual STD of ~ 1 observed in the noise of the background of the C 1 XP spectra.[81] A Monte Carlo simulation using 30 simulated spectra resulted in standard deviations of 0.015 and 0.030 for the peak position and full width at half maximum (FWHM), respectively, of the C–Si bond, indicating robust fitting parameters. The C 1s peaks at 285.0 (C–C and C–H) and 286.7 eV (C–O) were ascribed to adventitious carbon on the surface, contributed by multiple species. These peaks could not be deconvoluted from those associated with the C–C and C–H of covalently bound AA. The multiple C–C and C–H species that contribute to the peak at 285.0 eV give rise to a large FWHM value of 1.36 eV much larger than that observed for the C–Si signal at 284.2 eV of 0.87 eV. While the overlap between the adventitious carbon signal at 285.0 and the C–Si signal prevented quantitative comparisons of peak areas for various samples the position of the peak and robustness of fit for the C-Si emission allows the identification of AA covalently bound to the Si surface. The carbon signal observed at 288.9 eV was assigned to COOR[34] had a FWHM of 1.39 eV similar to that of the adventitious C at 285.0 suggesting that either multiple adventitious species also contribute to the signal and/or the moiety can take on multiple configures relative to the Si surface.

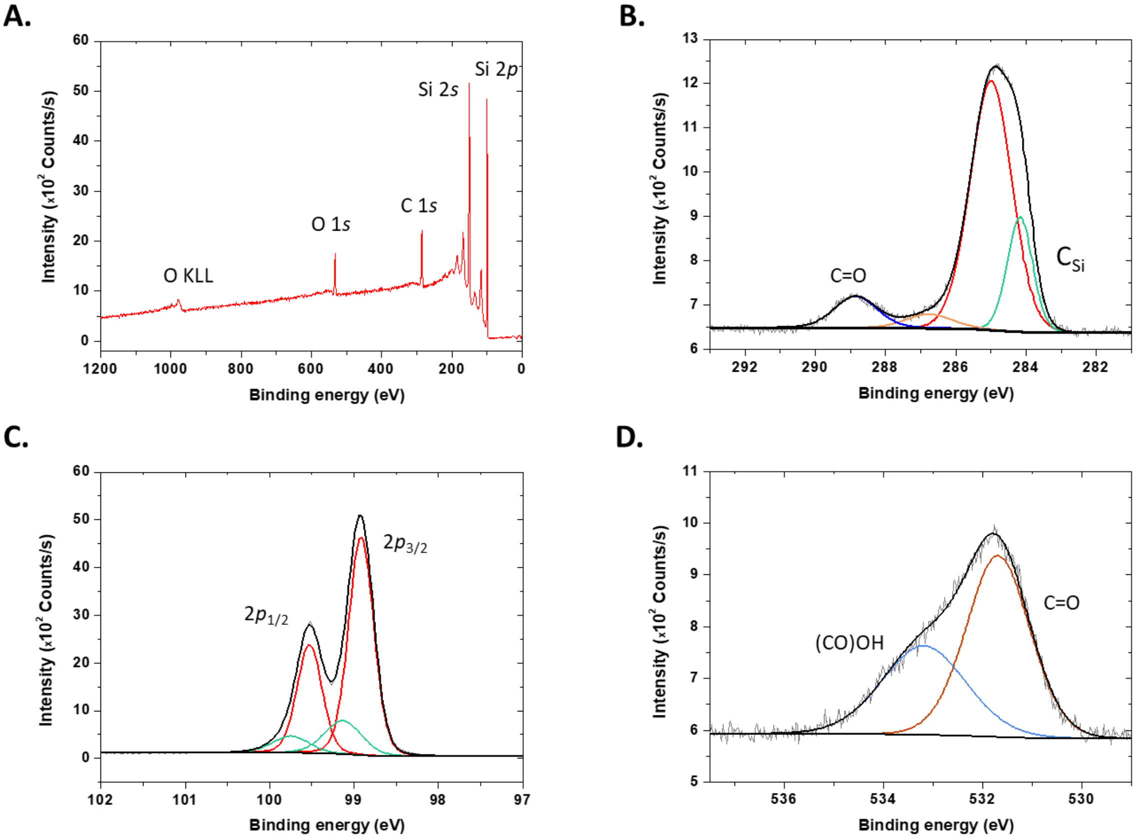

Figure 3.6 XPS (A) survey spectrum and high resolution (B) C 1*s*, (C) Si 2*p*, (D) and O 1*s* spectra of H–Si(111) surface treated with acrylic acid (AA) solution of 10 mM $(Me_5Cp)_2Co$ for 10 min.

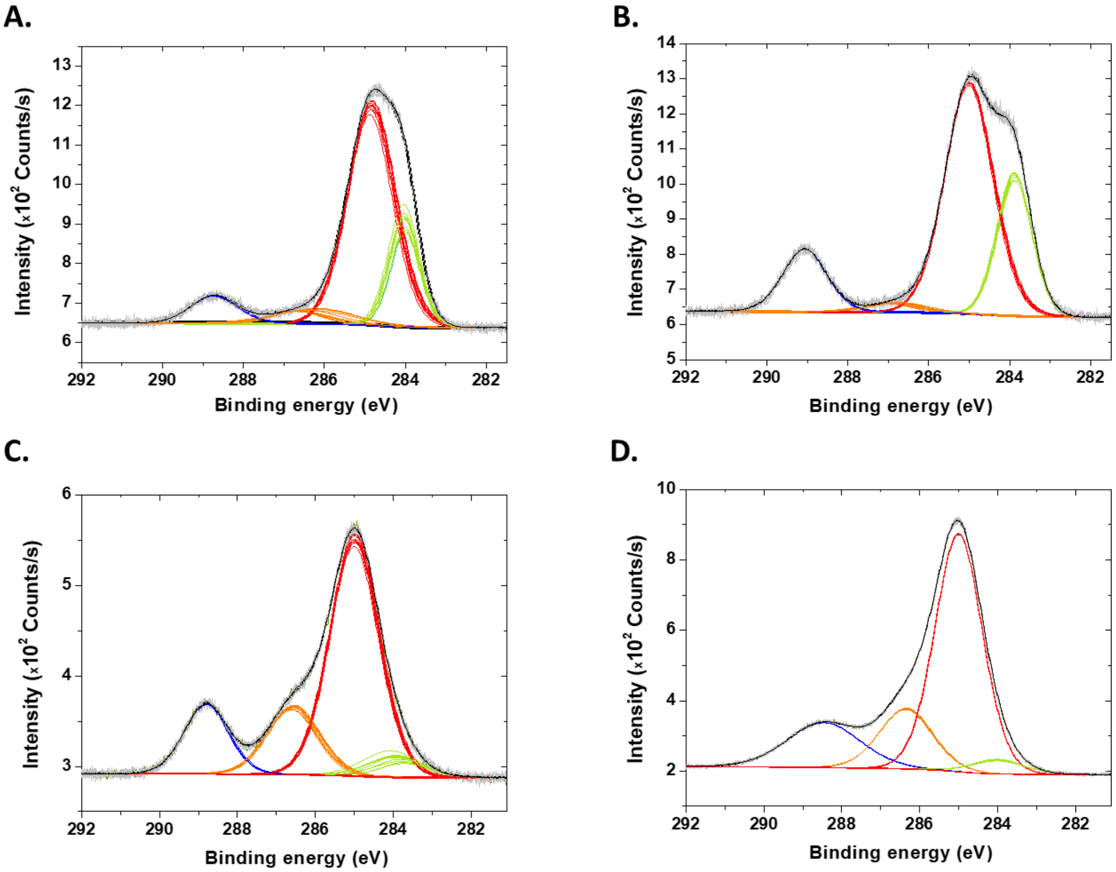

Figure 3.7 XPS high-resolution C 1*s* spectra and Monte Carlo simulations for H–Si(111) surfaces treated with A. acrylic acid (AA) solution of 10 mM $(Me_5Cp)_2Co$ for 10 min, B. AA solution of 10 mM Cp_2Co for 30 min, C. methyl acrylate (MA) solution containing 2.0 mM $(Me_5Cp)_2Co$, and D. MA solution containing 2.0 mM $(Me_5Cp)_2Co$, followed by hydrolysis in 1.0 M H_2SO_4(aq) at 35 ± 5 °C for 24 hours. 10 out of 30 representative simulated spectra are shown for clarity.

The high-resolution Si 2*p* spectrum (Figure 3.6C) showed a 2*p* doublet (2$p_{3/2}$ and 2$p_{1/2}$ peak splitting) at 99.1 and 99.7 eV, corresponding to both bulk and surface Si.[115] Signals originating from the carboxylic acid (C=O and (CO)OH) were observed in the high-resolution O 1*s* spectrum (Figure 3D; 531.7 eV and 533.2 eV, respectively). The difference between their intensities and FWHM may be attributed to oxygen-containing adventitious species introduced during post-reaction handling. Silicon oxide was not detected in the Si 2*p* and the O 1*s* spectra, and residual Co 2*p* was not detected in the survey spectrum (Figure 3.6A). We have excluded the presence of a Si–O–C linkage as Si emissions characteristic of Si–O are absent in the Si 2*p* and O 1*s* spectra while the OH group remains intact (Figure 3.6C and D).

The surface-bound layer formed by treating the H–Si(111) surface with a 10 mM AA solution of Cp_2Co for 30 min (Figure 3.5B, a) was also characterized by XPS (Figure 3.8). The high-resolution C 1*s* spectrum exhibited the adventitious carbon signal at 285.0 eV, a C–Si signal at 283.8 eV, and a carboxylic acid signal at 288.9 eV (Figure 3.8B). The ratio of the C–Si to adventitious carbon signals increased compared to Figure 3.6B and was attributed to a higher degree of surface functionalization with longer reaction times allowing the binding energy of the C–Si bond to be more accurately determined. C–Si peak fit robustness was demonstrated with Monte Carlo simulation (Figure 3.7B) that resulted in standard deviation values of < 0.01 for both peak position and FWHM. Bulk and surface Si species, as well as carboxylic acid signals, were observed, at their expected binding energies in the high-resolution Si 2*p* and O 1*s* spectra, respectively (Figure 3.8C and D). The Si 2*p* spectrum did not display SiO_x signals at high binding energies (101 eV – 102 eV). A peak at 530.9 eV in the O 1*s* region corresponds to a metal oxide, likely Co, species. A peak at 780 eV in the survey spectrum can be assigned to Co $2p_{3/2}$ and is ascribable to Cp_2Co and/or cobalt oxides absorbed on the surface that may be removed by further sonication and rinsing (Figure 3.8A) and was not further investigated.[122]

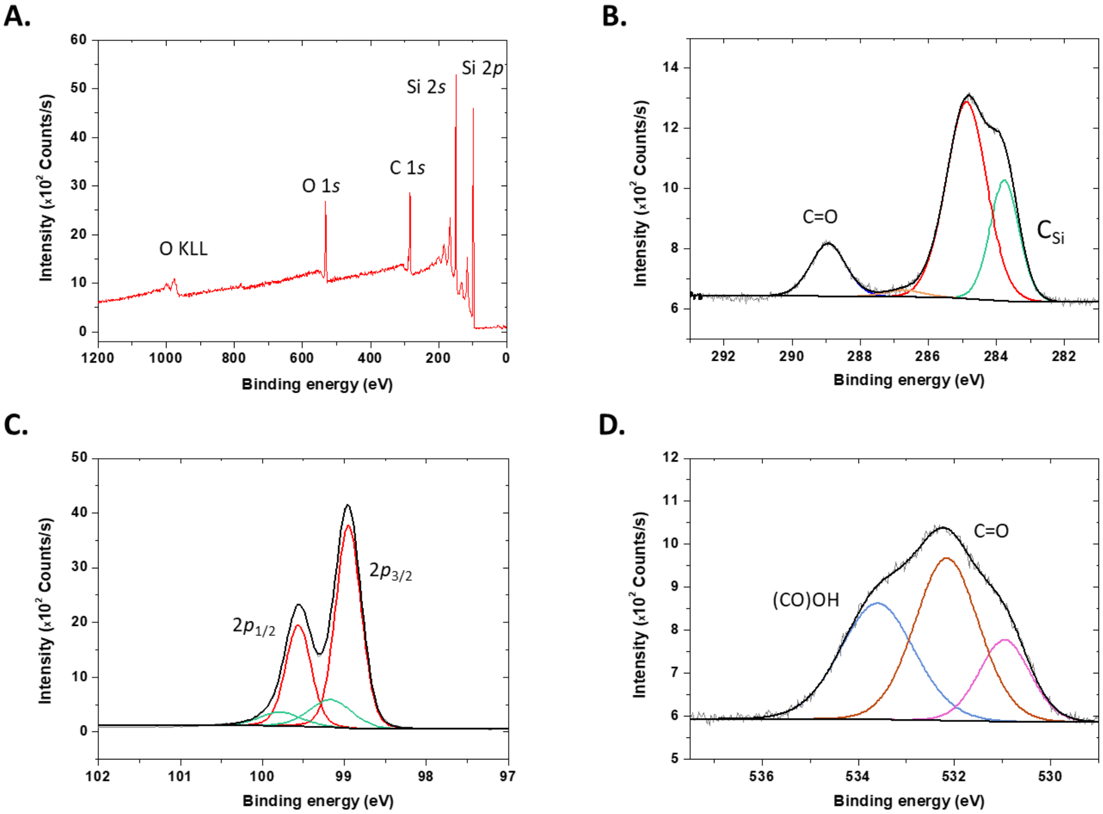

Figure 3.8 XPS survey spectrum (A) and high-resolution C 1*s* (B), Si 2*p* (C), and O 1*s* (D) spectra of H–Si(111) surface treated for 30 min with 10.0 mM Cp_2Co in acrylic acid (AA).

Surface-bound layer thicknesses were estimated using variable-angle spectroscopic ellipsometry (Table 3.1, Figure 3.9). Freshly prepared H–Si(111) resulted in an ellipsometrically measured overlayer of 1.21 ± 0.08 nm thick. Physisorbed carbon species are expected to contribute to this overlayer on the freshly prepared surface. Surface treatments with $(Me_4Cp)_2Ni$ (Figure 3.3) resulted in measured overlayer thicknesses of ~1.2 nm, indicating that AA was not bound to the surface. Treatment with 2.0 mM Cp_2Co for 60 min produced an increase in the measured overlayer thickness to ~ 1.7 nm, which is in agreement with typical values measured for SAMs.[123] $(Me_5Cp)_2Co$ treatment under nominally similar conditions produced a substantially higher measured thickness (10.25 ± 0.89 nm), consistent with polymerization after the initial SAM formation between surface-bound moieties and free AA in solution.[110] At a concentration of 2.0 mM, the stronger reductant ($(Me_5Cp)_2Co$) required intermediate reaction times (20-30 min) to produce layers of ~ 2.0 nm in measured thickness (Figure 3.10). At the same concentration, the intermediate strength reductant, Cp_2Co, resulted in an ellipsometrically measured 2.89 ±

0.01 nm thick layer after 60 min, with little or no detectable surface functionalization at shorter reaction times. Thick surface-bound layers (> 6.9 nm), formed by AA polymerization on the surface, were observed with the stronger reductant ($(Me_5Cp)_2Co$), at higher concentration (10.0 mM), and longer reaction times (20 min for $(Me_5Cp)_2Co$ and 30 min for Cp_2Co). Several combinations of reaction time and reductant concentration resulted in ellipsometric thicknesses and FTIR signals that were in accord with values measured for SAMs. However, the presence of a mixture of propionic acid SAM and polymerized products cannot be excluded because an increase in surface coverage and polymerization of the existing SAM with free AA can simultaneously occur.

Table 3.1 Spectroscopic ellipsometry-derived layer thickness (nm).[a,b]

	$(Me_5Cp)_2Co$			**Cp_2Co**			**$(Me_4Cp)_2Ni$**		
	2.0 mM	**5.0 mM**	**10.0 mM**	**2.0 mM**	**5.0 mM**	**10.0 mM**	**2.0 mM**	**5.0 mM**	**10.0 mM**
10 min	1.19 ± 0.02	3.28 ± 0.04	3.19 ± 0.08	-	0.97 ± 0.02	1.82 ± 0.05	-	-	-
20 min	1.35 ± 0.02	10.68 ± 0.59	14.46 ± 0.54	-	1.72 ± 0.01	2.47 ± 0.01	-	-	-
30 min	6.94 ± 1.01	-	-	1.25 ± 0.02	7.23 ± 0.92	11.10 ± 1.14	-	-	-
60 min	10.25 ± 0.89	-	-	2.89 ± 0.01	-	-	1.18 ± 0.02	1.04 ± 0.02	1.27 ± 0.02

[a] Reductant ($(Me_5Cp)_2Co$, Cp_2Co, $(Me_4Cp)_2Ni$) concentration: 2.0 mM, 5.0 mM, 10.0 mM.

[b] Surface treatment time: 10-60 min.

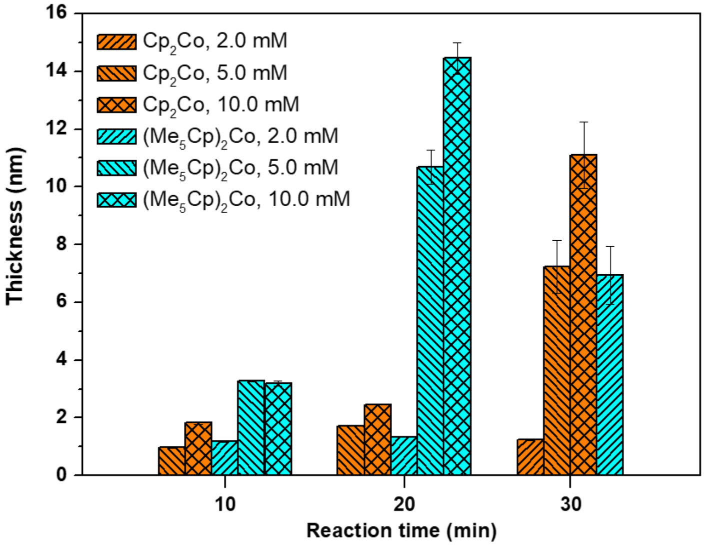

Figure 3.9 Layer thickness of H–Si(111) surfaces treated with AA solutions of Cp_2Co (orange) and (Me5Cp)$_2$Co (cyan), measured by spectroscopic ellipsometry. Reductant concentrations are represented by patterns according to the legend.

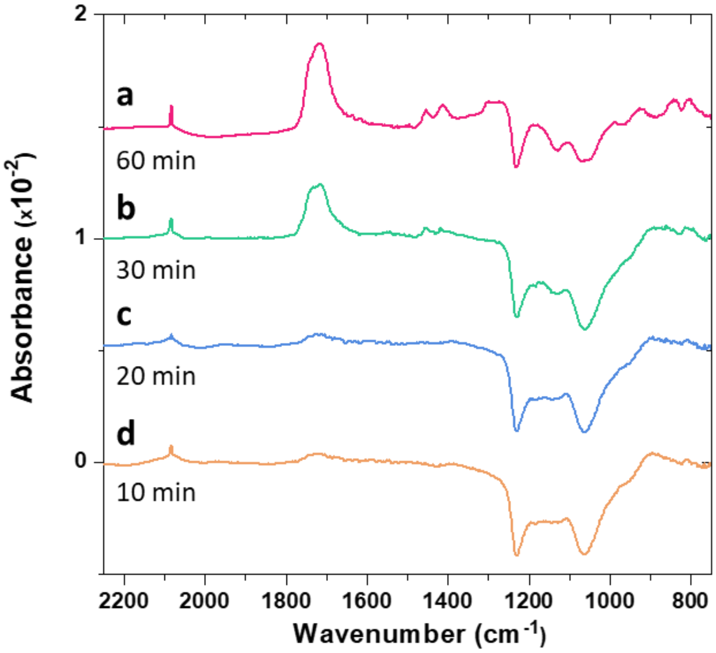

Figure 3.10 TIRS data for H–Si(111) surfaces after 10 min (d), 20 min (c), 30 min (b), and 60 min (a) treatment in acrylic acid (AA) containing 2.0 mM of $(Me_5Cp)_2Co$. The spectra are offset vertically for clarity.

3.3.2 Addition of Methyl Acrylate to Si(111) surfaces

To assess the contribution of polymeric species to the surface overlayer, polymerization during SAM formation can in principle be prevented by elimination of the –OH group on the AA, by use of MA (Figure 3.11). Figure 3.12 shows the TIRS spectra of H–Si(111) after reductant-activated addition of MA in the presence of $(Me_5Cp)_2Co$ (Figure 3.12a), $(Me_4Cp)_2Ni$ (Figure 3.12b), or Cp_2Ni (Figure 3.12c). The ν(C=O) signal associated with the ester carbonyl appeared at 1744 cm^{-1} with significantly higher intensity for the samples treated with $(Me_5Cp)_2Co$ and $(Me_4Cp)_2Ni$ compared to those treated with Cp_2Ni. This demonstrates that reductant-activated electrophilic addition is achieved when the reductant's reduction potential is more negative than the Si CBM potential. When this condition is not met, surface functionalization is not obtained. As we cannot exclude that the surface coverage of the AA-functionalized surfaces is higher than the MA-functionalized surfaces, a distinction between C=O bonds associated with monolayers and polymerized products cannot be made. Ellipsometrically-derived layer thicknesses were 1.66 ± 0.05 nm ($(Me_5Cp)_2Co$), 1.89 ± 0.01 nm ($(Me_4Cp)_2Ni$), and 1.00 ± 0.01 nm (Cp_2Ni), respectively.

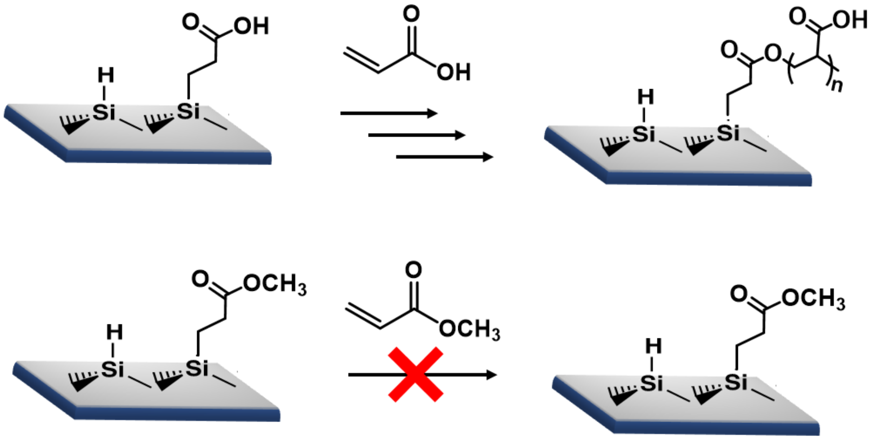

Figure 3.11 Schematic for polymerization through double bond of acrylic acid (top) and blocking of polymerization pathway via methyl ester substitution (bottom).

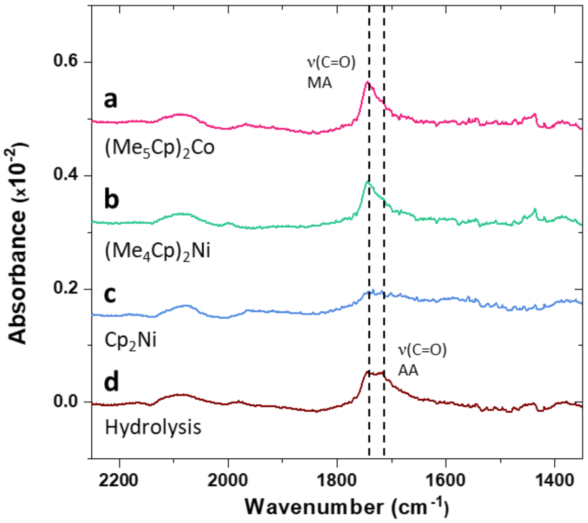

Figure 3.12 TIRS data for H–Si(111) surfaces after a 60 min treatment in methyl acrylate (MA) solution containing (a) 2.0 mM $(Me_5Cp)_2Co$, (b) 10.0 mM $(Me_4Cp)_2Ni$, and (c) 10.0 mM Cp_2Ni. H–Si(111) surface treated with $(Me_5Cp)_2Co$ was subjected to (d) hydrolysis in 1.0 M H_2SO_4 at 35 ± 5 °C for 24 hours. The spectra are offset vertically for clarity.

Ester hydrolysis of the surface-attached MA was performed with the $(Me_5Cp)_2Co$-treated surface for 24 h in 1.0 M H_2SO_4 at 35 ± 5 °C. The hydrolysis resulted in the appearance of the characteristic carboxylic acid ν(C=O) signal at 1717 cm^{-1}, whereas the 1744 cm^{-1} signal intensity decreased (Figure 3.12d), indicating partial hydrolysis. After hydrolysis, the ellipsometricallly measured overlayer thickness was 1.45 ± 0.01 nm. High-resolution C 1*s* XPS analysis of the MA-based SAM (Figure 3.13) was in accord with the TIRS data, showing a 20% increase in the ratio between the area of the carbonyl (~ 288.5 eV) and methyl (~ 286.5 eV) peaks. Moreover, the FWHM of the carbonyl peak increased from 1.3 eV to 2.2 eV after hydrolysis, indicating the presence of two carbonyl species, as expected from partial ester hydrolysis. Although MA hydrolysis is expected to result in a decreased the XPS C–C emission, the decrease is obscured by an increase in surface adventitious carbon following exposure to solvents and air during MA hydrolysis. Monte Carlo simulations indicate a robust fit model for the C 1*s* peaks (Figure 3.7C and D).

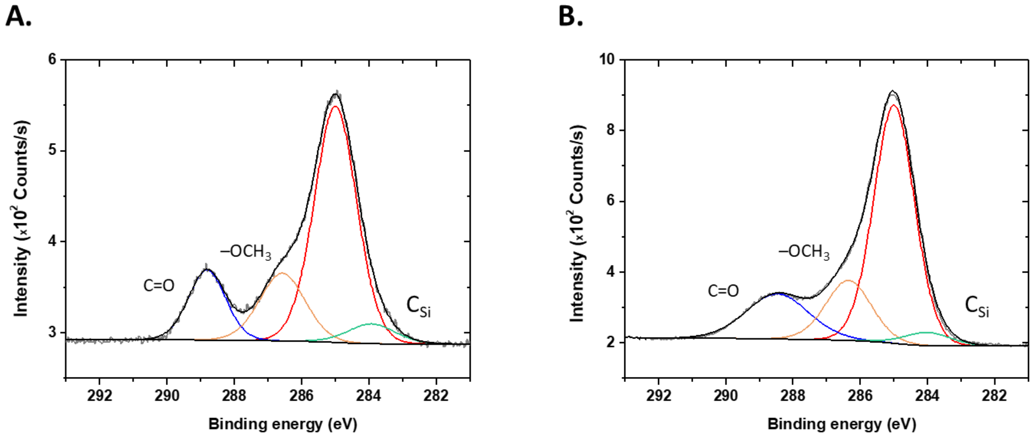

Figure 3.13 XPS high-resolution C 1*s* spectra for H–Si(111) surfaces after a 60 min reaction time in methyl acrylate (MA) solution containing 2.0 mM $(Me_5Cp)_2Co$ (A), and after hydrolysis in 1.0 M $H_2SO_4(aq)$ at 35 ± 5 ºC for 24 hours (B). The spectra are offset vertically for clarity.

3.4 Conclusions

In summary, we have demonstrated the reductant-activated electrophilic addition reaction to H–Si(111) surfaces using AA and MA. Reaction initiation requires the presence of a reductant with a reduction potential above the Si CB edge. For functionalization with AA or MA, the proposed mechanism involves the activation of the Si surface by injection of charge from a molecular reductant in solution. The activated surface then loses a H atom and is attacked by the C_β of the free AA/MA in solution with the formation of a C-Si bond (Figure 3.1). AA functionalized surfaces can further react through the carboxylate group of the surface bound acrylate by reacting with the C_β of free AA in solution with subsequent polymerization occurring through the carbon double bond (Figure 3.11).[109,110] Radical-initiated solution-based acrylate polymerization, reactions that require the presence of a radical initiator, UV irradiation, or elevated temperatures, which were not present during the reductant- activated surface functionalization, were unlikely to occur. The presence of the C 1s XPS emission, due to the C–Si bond, confirms the presences of the covalently bound acrylate (AA or MA) to the Si surface. XPS and FTIR data for both AA and MA indicate the presence of carboxylic acid and ester groups, respectively, which also confirms that functionalization occurs through the double bond end of the AA or MA.

Polymerization of surface bound MA did not take place, as seen by the similar thickness values obtained with different reductants, which supports the proposed polymerization mechanism when AA is present. Moreover, use of MA as the electrophile minimizes protonation of the metallocenes, which enables the reaction to occur with mild reductants, such as $(Me4Cp)_2Ni$. H–Si(111) surface functionalization with AA and MA results in the consumption of H–Si bonds, which in turn will result in changes to the surface dipole and position of Si CBM relative to the solution electrochemical potential. These changes can impact the reactivity of the remaining Si surface atoms. Moreover, as the coverage increases, especially above the ~50% surface coverage levels observed herein, steric interactions between adjacent AA or MA groups would occur and significantly change the energetics of the reaction, making it harder to functionalize these sites.

Reductant-activated electrophilic addition enables the formation of stable C–Si bonds while simultaneously enabling the incorporation of additional functional groups in the SAM. Reactive functional groups can be utilized for subsequent surface reactions and be used to covalently cross-link different Si surfaces for optoelectronic applications. This work expands our understanding on the utility of CB-initiated covalent surface functionalization processes.

In the next chapter, we expand this surface functionalization method to silicon nanocrystals with diameters of 8 nm, 5 nm, and 3 nm, and explore the reaction dependence on reductant strength and nanocrystal size. This study will provide a deeper understanding of interplay between the reductant solution potential and the CB edge, which differs across the various sized silicon nanocrystals.

Chapter 4 – Reductant-activated Surface Functionalization of Silicon Nanocrystals

4.1 Introduction

Over the last decade, silicon nanocrystals (Si NCs) have emerged as a non-toxic, biocompatible alternative to the more commonly employed II-VI, IV-VI, and III-V semiconductor QDs.[124,125] Silicon is comparatively less expensive than other QDs as it is an earth abundant material, making up approximately 28% of the earth's crust.[48,125,126] Moreover, planar silicon has dominated the microelectronics industry for decades, leading to widespread knowledge about its mechanical, electronic, and optical properties.[48,125,126] In addition to these qualities that motivate the use of Si NCs as an alternative to other QDs, Si NCs also present distinctive optical and electronic properties that are not present in the bulk Si material such as observable photoluminescence.

The properties of Si NCs can be tuned through chemical modification of the surface via covalent attachment of small organic moieties. Functionalization enables passivation of surface defects and protection from oxidation at ambient conditions,[127] tuning of the band gap and resulting optical properties,[6,128] tailoring of the NC solubility for desired applications,[51] and covalent linkage to other structures or molecular catalysts.[52] Current surface functionalization methods available for these materials include thermal hydrosilylation, radical and Lewis acid-mediated routes, photochemical hydrosilylation, and microwave methods.[48] However, each of these functionalization pathways present certain disadvantages that limit the types of Si linkages that can be formed and the diversity of ligands that can be used. For example, thermal hydrosilylation must be conducted at very high temperatures often exceeding 170 °C with high boiling point solvents. In contrast, microwave methods allow for lower boiling point solvents, but require the use of specialized instrumentation. Radical and Lewis acid-mediated functionalization methods can be carried out with more mild synthesis conditions but cannot be used to attach ligands with multiple reactive ends or certain functional groups (e.g., alcohols). Photochemical functionalization can be performed without an initiator but is limited to NCs of diameters smaller than their Bohr exciton radius of 5 nm. These disadvantages impose a need for new surface functionalization routes to expand the types of ligands and linkages that can be applied to Si NCs.

Prior work demonstrated a new surface functionalization method for Si surfaces based on the addition of a one-electron, outer-sphere oxidant to facilitate attachment of nucleophilic ligands. This reaction was first shown by attaching methanol onto the bulk Si(111) surface through a Si–O linkage using a number of metallocene-based oxidants, where stronger oxidants enabled higher surface coverages.[106] Oxidant-activated nucleophilic addition was then performed on various sizes of Si NCs to explore the relationship between the material's electronic structure and the redox potential of the oxidant used.[6] These reactions demonstrated that the redox potential of the oxidant must be more positive or near the valence band of the Si NC material as a requirement for successful attachment of organic moieties. In addition, this reaction allowed access to a diverse set of Si linkages through Si–O, Si–N, Si–S, and Si–P bonds. Recently, an analogous reductant-activated surface functionalization route was developed to attached electrophiles (i.e., alkyl halides) onto 1T´-MoS_2 nanosheets, where the surface coverage similarly increased with reductant strength.[81] This work was easily expanded to functionalize WS_2 surfaces with methyl groups, demonstrating the reaction's potential for broad applicability to other semiconductor surfaces.[129]

We report herein the analogous reductant-activated electrophilic addition to Si NC surfaces and explore the relationship between the Si NC electronic structure and the redox potential of the reductants employed. Figure 4.1 illustrates the functionalization route explored, in which hydride-terminated Si NCs with diameters of 3, 5, or 8 nm were reacted with methyl acrylate (MA) in the presence of two one-electron metallocene reductants including cobaltocene (Cp_2Co) and a stronger reductant, decamethylcobaltocene ($Me_{10}Cp_2Co$). Although the analogous electrophile acrylic acid has already been attached to Si NC surfaces using various functionalization routes,[108,109] MA was selected as the electrophile for this work due to the lack of reactivity of its ester group toward oligomerization through the Michael addition reaction as discussed in Chapter 3,[110] allowing for more facile and accurate characterization of the resulting monolayer (Figure 3.11).

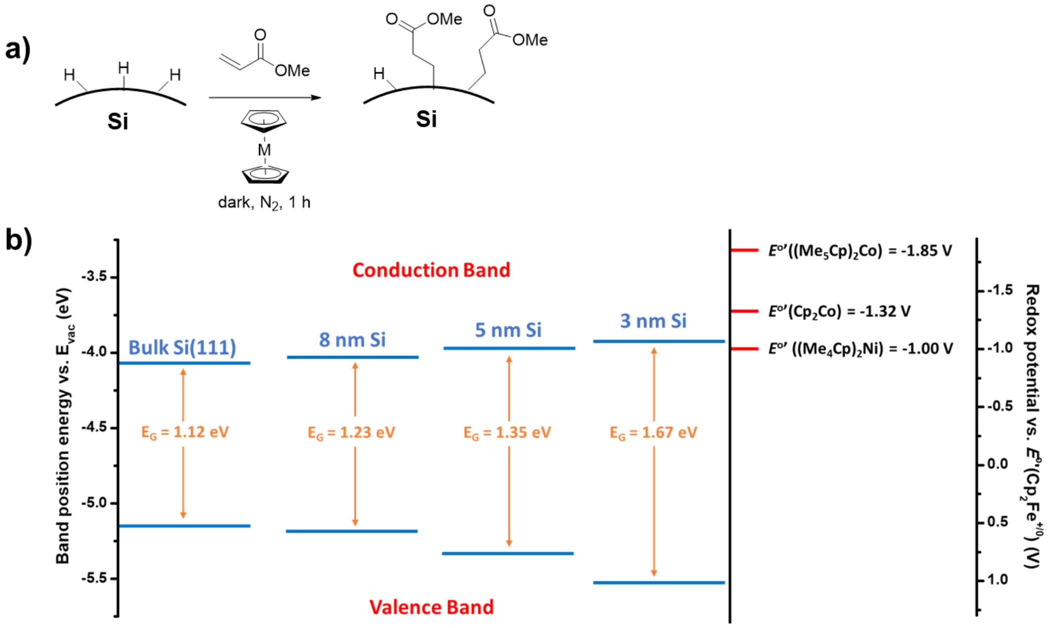

Figure 4.1. Reductant-activated addition of electrophiles to hydride-terminated Si NCs. (a) Reaction scheme for surface functionalization of hydride-terminated Si NCs under the presence of the one-electron outer-sphere metallocene reductants. (b) Band diagram comparing bulk Si and various sizes of Si NC band edges relative to E_{vac} and redox potentials of metallocenes used to activate electrophilic addition reaction.

4.2 Experimental

4.2.1 Materials

Trichlorosilane (99%, Aldrich), anhydrous ethanol (200 proof, Koptec), hydrofluoric acid (49%, semiconductor grade, Transene), anhydrous methanol (99.8%, Sigma-Aldrich) were used as received. Methyl acrylate (%, Sigma-Aldrich) was degassed with three freeze-pump-thaw cycles prior to use. Water (resistivity ≥ 18.2 MΩ-cm) was obtained from a Barnstead E-pure system. Forming gas (5% hydrogen/balance nitrogen) and argon (ultra-high purity 5.0 grade) were purchased from Airgas. Unless specified, solvents were purchased as ACS grade and used as received. Decamethylcobaltocene and cobaltocene (technical grade, Aldrich) were used as received. Quartz tubes (22 × 25 mm, 4 ft. length) were purchased from GM Associates, and quartz boats (100 mm L × 17 mm W × 10mm H) from MTI Corporation. Alumina tubes (99.8%, 18 × 24 mm, 4 ft. length) were purchased from Anderman Industrial Ceramics, and alumina boats (99.8%, 70 mm L × 14 mm W × 10 mm H) from Coorstek Incorporated.

4.2.2 Synthesis of Si NC composite

Preparation of the Si NC/SiO_2 composite was accomplished in two steps: synthesis of a sol-gel polymer precursor and its subsequent thermal processing.[47,48] The sol-gel polymer precursor $(HSiO_{1.5})_n$ was synthesized by first adding trichlorosilane (4.5 mL, 45 mmol) to a Schlenk flask and cooling to 0 °C under inert atmosphere. While stirring vigorously, water (1.6 mL, 90 mmol) was added in one rapid injection while venting to remove hydrochloric acid vapors formed during the reaction, and the mixture was allowed to warm to room temperature for one hour. The resulting translucent white precipitate was then dried completely for at least three hours under vacuum. Due to its air-sensitivity, the sol-gel polymer was used immediately after its synthesis. To prepare it for further processing, the large chunks of dried polymer were ground briefly (< 5 min.) via vigorous stirring under inert atmosphere, yielding a fine white powder. The sol-gel polymer precursor was then quickly transferred to a quartz boat and heated in a tube furnace to produce a composite of 3, 5, or 8 nm diameter Si NCs at a peak processing temperature of 1100, 1200, or 1300 °C, respectively, for 1 hour under a slightly reducing atmosphere provided by flowing forming gas (95% nitrogen/5% hydrogen) at a flow rate of ~5 mL/s. A ramp rate of 10 °C/min was used to reach the peak processing temperature. After heating, the composite was cooled to below 50 °C under forming gas flow before removal from the furnace.

4.2.3 Preparation of hydrogen-terminated Si NC surfaces

The hydride-terminated Si NC surface provides a highly reactive starting point for most surface functionalization methods. In a typical procedure, the Si NC/SiO_2 composite (0.25 g) was added to a 50 mL polymethylpentene (PMP) beaker with a Teflon stirbar. The powder was then suspended by sonication for 30-60 seconds in a solvent mixture of ethanol and water (1:1 v/v, 6 mL total). To this, hydrofluoric acid (3 mL) was added, and the brown mixture was stirred for 1 hour under subdued light. The completion of the etching process can be qualitatively confirmed by the golden color of the mixture. The liberated, hydrophobic Si NCs were then extracted with toluene (3 × 15 mL). The suspensions were centrifuged (3100 rpm, 10 min.), and the supernatant was quickly removed. The centrifuge tubes containing the NC pellets were immediately backfilled with argon and then transferred to a nitrogen-filled glovebox for subsequent reactions.

4.2.4 Addition of methyl acrylate to hydrogen-terminated Si NC surfaces

Under inert atmosphere, Si NCs were suspended in degassed MA (20 mL) and partitioned evenly into four foil-covered vials containing the reductant (10 mM) or no reductant. The reaction solutions were stirred in the dark for 1 hour. The suspensions were centrifuged (3100 rpm, 10 min.), and the supernatant was removed in the glovebox. The Si NC pellets were rinsed with 5 mL methanol via sonication (2 min.) and centrifuged (3100 rpm, 10 min). The supernatant was removed under inert atmosphere, and this process was repeated once more for a total of 2 times. The NCs were prepared for sample characterization by removing the supernatant and dropcasting the NCs with minimal solvent.

4.2.5 Instrumentation

The infrared (IR) spectra were collected by performing attenuated total reflectance Fourier transform infrared spectroscopy (ATR-FTIR) on a Thermo Scientific Nicolet 6700 optical spectrometer equipped with a thermoelectrically cooled deuterated *L*-alanine-doped triglycine sulfate (DLaTGS) detector, an electronically temperature-controlled (ETC) EverGlo mid-IR 13 source, a nitrogen gas purge, and a KBr beam splitter. Functionalized Si NCs were drop casted onto a diamond window and allowed to dry before measurement.

X-ray photoelectron spectroscopy (XPS) data was collected using a Kratos AXIS Ultra spectrometer equipped with a hybrid magnetic and electrostatic electron lens system and a delay-line detector (DLD). The photoelectron-ejection vector was 90° with respect to the sample surface plane. XPS data were collected using a monochromatic Al Kα X-ray source (1486.7 eV) at pressures < 9 × 10-9 Torr. The electron-collection lens aperture was set to sample a 700 × 300 µm spot. The analyzer pass energy was 80 eV for survey spectra and was 10 eV for high-resolution spectra. The electron-collection lens aperture was set to a 55 µm spot size and the analyzer pass energy was 5 eV. The instrument energy scale and work function were calibrated using clean Au, Ag, and Cu standards. Si NC samples were prepared by dropcasting on Cu foil and allowed to dry under inert atmosphere and transferred to the XPS. The instrument was operated using Vision Manager software v. 2.2.10 revision 5 and data were analyzed using CasaXPS software (CASA Software Ltd).

4.3 Results and Discussion

4.3.1 Influence of reductant strength on Si NC reactivity

Figure 4.2 displays a representative set of FT-IR spectra for hydride-terminated Si NCs treated in the absence of reductant and in the presence of reductant, with characteristic sharp Si–H stretching vibrations at ca. 2255 cm^{-1}, strong Si–O–Si vibrations from ca. 1000-1300 cm^{-1}, and H–Si–O hybrid vibrations from ca. 800-900 cm^{-1} present in all spectra, corresponding well to the FTIR spectra reported by Henderson et al.[47] Peaks associated with methyl acrylate were also observed in all three spectra, with characteristic C–H stretches at 2925 cm^{-1}, C=O stretches at 1700 cm^{-1}, C–H_2 scissoring mode at 1450 cm^{-1}, and a C–O stretch at 1395 cm^{-1}. A small sharp peak for C=C was displayed at 1550 cm^{-1} for samples treated in the absence of reductant. The presence of the C–H_2 peak indicates successful attachment of MA due to the saturation of the C=C peak in the free molecule upon covalent binding to the Si surface.[109] The higher intensity of this peak in samples treated with reductant compared to those treated without reductant demonstrates that the presence of the reductant increases the reactivity of the Si surface toward electrophilic addition. This is corroborated by the significantly greater intensity of the C=O and C–O peaks relative to the Si–H stretch in samples treated with reductant. Moreover, samples treated with the stronger reductant, decamethylcobaltocene, illustrate even greater relative C=O peak intensity, suggesting that stronger reductants increase surface coverage. However, the presence of Si–O vibrations associated with oxidation of the Si surface convolutes the exact MA coverage achieved due to the conversion of Si–H bonds to both Si–CH_2 and Si–O bonds. No surface reacted with MA is completely rid of the hydride species, which may lead to oxidation during the rinsing process or during measurements.

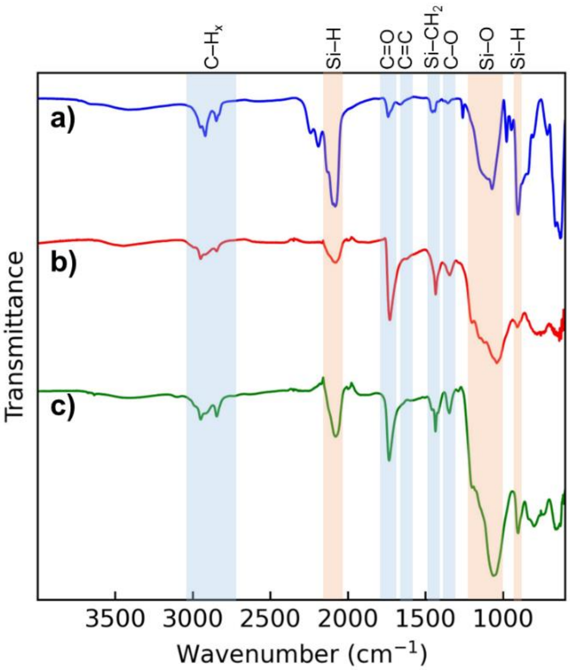

Figure 4.2 Representative FT-IR spectra measured for 5 nm diameter Si NCs treated with neat MA under the presence of (a) no reductant, (b) decamethylcobaltocene, and (c) cobaltocene. Highlighted peaks in orange represent vibrations associated with Si bonds, and highlighted peaks in blue represent vibrations associated with MA.

To corroborate the IR spectra, XP spectra were also collected for each of the samples. Figure 4.3 demonstrates a representative set of spectra measured for Si NCs with a diameter of 5 nm treated with MA in the presence of decamethylcobaltocene and cobaltocene and in the absence of reductant. In the absence of reductant, the Si 2*p* spectra demonstrates peaks at 100.5 eV and 101.6 eV corresponding to Si(0) atoms and Si–C bonds resulting from functionalization with MA through the C=C bond (Figure 4.3a). The presence of the small Si–C peak corroborates the presence of C–H, C=O, and Si–CH$_2$ vibrations in the IR spectra (Figure 4.2a), indicating that minimal surface functionalization occurs even in the absence of reductant. The Si 2*p* spectra of the Si NCs treated in the presence of decamethylcobaltocene illustrate peaks at 98.3 eV, 98.9 eV, and 102.4 eV corresponding to Si(0) atoms, Si–C bonds, and silicon oxide species, respectively (Figure 4.3b). Si NCs treated with MA in the presence of cobaltocene display peaks at 98.7 eV, 99.6 eV, and 102.9 eV corresponding to Si(0) atoms, Si–C bonds, and silicon oxide species (Figure 4.3c). In both cases where the Si NCs were treated with MA in the presence of a reductant, the Si–C peak appears with greater area than the samples treated in the absence of reductant due to the formation of a surficial Si–C bond through the C_β atom of the C=C bond in MA. The presence of oxide species in the samples treated with reductant may be attributed to oxidation of the surface due to small amounts of oxygen introduced during the sonication and centrifugation process or during sample preparation prior to measurement.

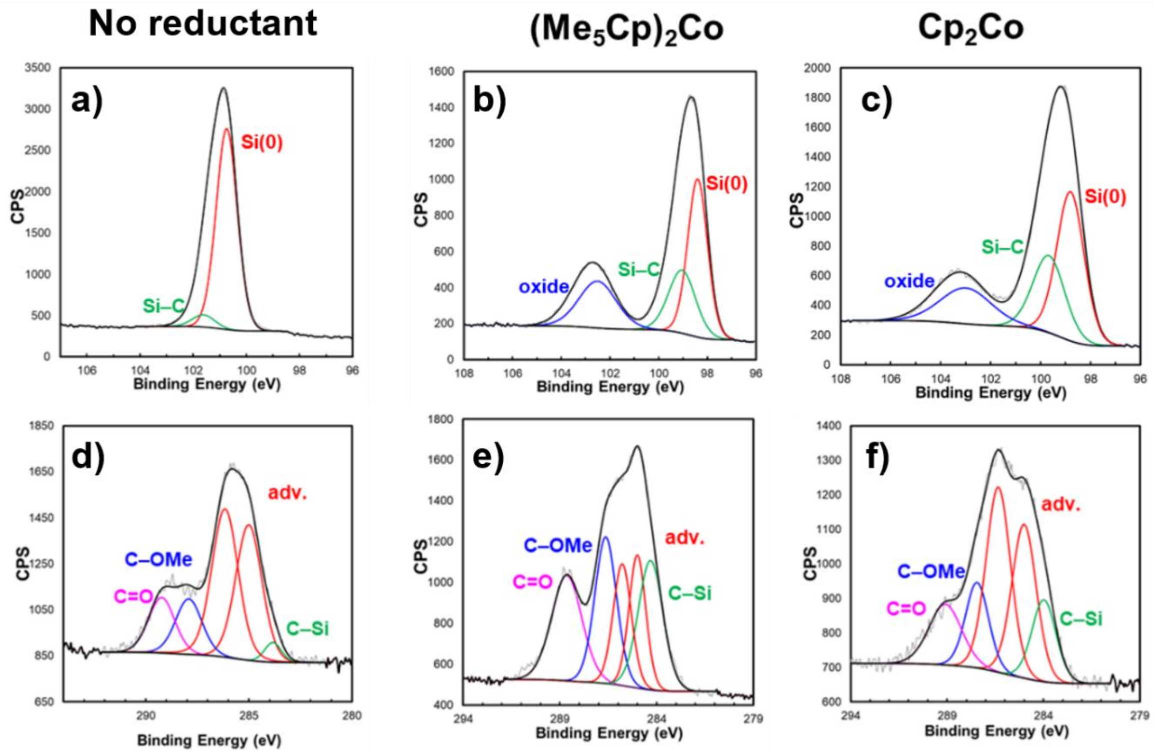

Figure 4.3 Representative XP spectra measured for Si NCs of 5 nm diameter treated with neat MA in the presence of (a, d) no reductant, (b, e) decamethylcobaltocene, and (c, f) cobaltocene. Each column represents each reductant condition tested. The top row represents Si 2*p* XP spectra and the bottom row displays C 1*s* XP spectra.

Figure 4.3d-f displays a representative set of C 1*s* XP spectra of 5 nm diameter Si NCs treated with MA in the presence of decamethylcobaltocene and cobaltocene and in the absence of reductant. Si NCs treated with MA in the absence of reductant illustrate peaks at 283.7 eV, 285.1 eV, 286.0 eV, 287.8 eV, and 289.5 eV corresponding to C–Si, adventitious C–C, adventitious C=C, C–OMe, and C=O bonds, respectively (Figure 4.3d). The presence of a small C–Si peak indicates that a small amount of MA reacted with the Si NC surface. The C–OMe and C=O peaks in the XP spectra likely result from a combination of a small amount of surface functionalization as well as adsorbed residual MA. Si NCs treated in the presence of decamethylcobaltocene show peaks at 284.0 eV, 285.0 eV, 285.7 eV, 286.6 eV, and 288.6 eV can be attributed to C–Si, adventitious C–C, adventitious C=C, C–OMe, and C=O bonds, respectively. Samples treated with cobaltocene display peaks at 283.8 eV, 284.9 eV, 286.2 eV, 287.5 eV, and 289.0 eV represent C–Si, adventitious C–C, adventitious C=C, C–OMe, and C=O bonds, respectively. In contrast to the Si NCs treated without reductant, samples treated with decamethylcobaltocene and cobaltocene display stronger C–Si peaks due to greater extent of covalent functionalization. Furthermore, the C=O peak present in the spectra of Si NCs treated with decamethylcobaltocene appear with greater intensity than the C=O peak of Si NCs reacted with cobaltocene, which appears as a weaker shoulder. This further demonstrates that reductant strength increases the reactivity of the surface toward electrophilic addition, validating the reductant strength trends observed in the IR spectra (Figure 4.2b and c).

4.3.2 Si NC size dependency of surface reactivity

To determine the NC size dependency of the reaction, 8 nm and 3 nm diameter hydride-terminated Si NCs were treated similarly with neat MA under the presence of no reductant, decamethylcobaltocene, or cobaltocene. Figure 4.4 displays zoomed-in regions containing the Si–H, C=O, and Si–O vibrations. The spectral trends observed for the 5 nm diameter Si NCs hold for each size tested, where the peak intensity of C=O increases dramatically with respect to the hydride peak when treated with stronger reductants. However, no distinct trend was observed correlating the size of the Si NC to the relative intensity of the C=O peak, indicating that there is no strong reaction dependency on Si NC size. This contrasts oxidant-activated addition,[6] where NC size strongly influenced the extent of the reaction, displaying a distinct “on-off” mechanism in which the weakest reductant tested only activated 8 nm Si NCs toward nucleophilic addition and zero reactivity was observed for smaller NCs. In oxidant-activated nucleophilic addition, a major requirement for reactivity is that the redox solution potential of the oxidant must lie near or above the valence band of the Si NC used. Analogously, it was expected that the redox solution potential of the reductant must lie near or above the conduction band edge of the Si NC for reductant-activated electrophilic addition. Here, the lack of Si NC size dependency in reductant-activated addition may be attributed to the significantly smaller energy difference between the conduction bands of the different sized Si NCs (Figure 4.1b) compared to the valence bands.

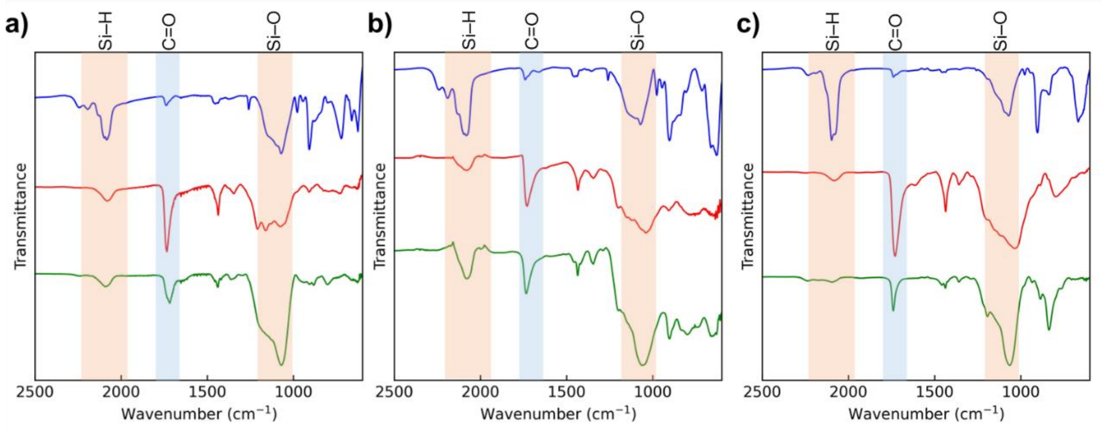

Figure 4.4 Zoomed-in regions of FT-IR spectra for (a) 8 nm, (b) 5 nm, and (c) 3 nm diameter Si NCs treated with neat MA under the presence of no reductant (top, blue), decamethylcobaltocene (middle, red), or cobaltocene (bottom, green). Highlighted peaks in orange represent vibrations associated with Si bonds, and highlighted peaks in blue represent vibrations associated with MA.

To further investigate the dependency of Si NC size on the reactivity of the surface toward electrophilic addition, XPS was performed and the size dependency of the reaction was compared using the C 1*s* XP spectra (Figure 4.5). Similar spectral trends were observed correlating reactivity to reductant strength as in Figure 4.3, where Si NCs treated with neat methyl acrylate in the presence of decamethylcobaltocene resulted in C=O peaks with greater area than the samples treated in the presence of cobaltocene. Those treated with cobaltocene result in a C=O peak that appears as a weak shoulder compared to decamethylcobaltocene-treated samples where the C=O peak is more distinct. As in Figure 4.3, samples treated in the absence of reductant displayed a very weak to no C–Si peak indicating poor reactivity of the surface toward electrophilic addition, and peaks attributed to C=O and C–OMe can be associated with residual adsorbed methyl acrylate remaining from incomplete washing. No distinct trend was observed across the 8 nm, 5 nm, and 3 nm sized Si NCs, confirming the lack of size dependency of the reaction observed in the IR spectra (Figure 4.4).

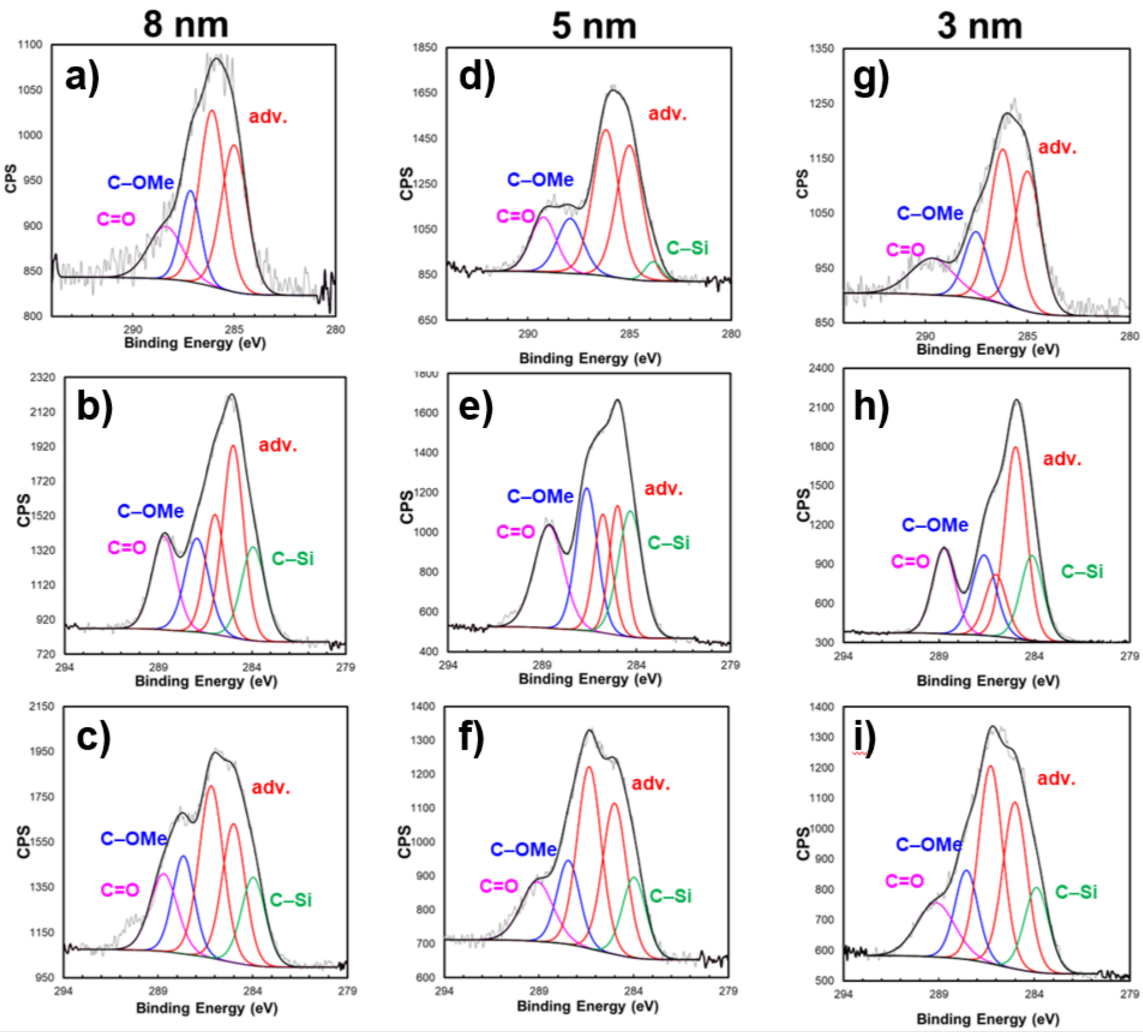

Figure 4.5 C 1*s* XP spectra collected for Si NCs with diameters of (a-c) 8 nm, (d-f) 5 nm, and (g-i) 3 nm treated with neat methyl acrylate in the presence of (top row) no reductant, (middle row) decamethylcobaltocene, and (bottom row) cobaltocene.

4.4 Conclusions

In summary, reductant-activated electrophilic addition of methyl acrylate to hydride-terminated Si NC surfaces was demonstrated, in which methyl acrylate adds to the surface through a covalent Si–C bond. When a reductant with a redox solution potential near or above the conduction band of the Si NC material is added, the surface becomes sufficiently electrophilic, allowing for the C_β atom of methyl acrylate to bind to the surface, producing a covalent Si–CH_2 bond. Thus, the reactivity of the surface toward electrophilic addition depends on the strength of the reductant, where stronger reductants resulted in greater extent of functionalization and the absence of reductant resulted in minimal to no reactivity.

This reductant strength dependency is observed across all sizes of Si NCs tested, including 8 nm, 5 nm, and 3 nm diameters. Although oxidant-activated nucleophilic addition demonstrates a strong dependency on Si NC size, no trend was observed correlating Si NC size to the extent of electrophilic addition, which may be attributed to the small energy differences between the conduction band edges of the differently sized Si NCs in comparison to their valence bands. This work completes our experimental understanding of redox-activated surface reactions of Si materials, providing a new avenue for functionalization that is mild, requires no specialized equipment, and agnostic to functional groups in the small molecule bound to the surface. Furthermore, this work allows for more precise control over the Si surface at an atomic level. This novel functionalization route enables various applications and purposes, including electronic structure-selective purifications, new surface moieties with accessible functional groups that would otherwise be incompatible with conventional Si surface functionalization methods, as well as achievement of more complex 3D architectures by linking Si materials to other materials.

In the final chapter, we present a new method of synthesizing Si NCs using a time-dependent thermal annealing process and use oxidant-activated addition to form a mixed monolayer based on Si–O linkages. This reaction will provide a method for controlling the functional group that adds to the Si NC surface, while preserving the other functional group for further reactions. At the end of this chapter, we present a strategy for crosslinking Si NCs using the intact functional group with an orthogonal reaction to form a mesostructured material.

Chapter 5 – Time-dependent Silicon Nanocrystal Synthesis and Mixed Monolayer Surface Functionalization to Achieve Mesostructured Materials

5.1 Introduction

Quantum dots (QDs) are semiconductor nanocrystals that have revolutionized a wide variety of important technological fields including biological imaging and therapeutics,[130–132] sensing of chemically and biologically relevant compounds,[133–136] environmental remediation,[137,138] and photovoltaics[139–142] owing to the unique size-tunable or shape-tunable optical and electronic properties that arise from quantum confinement. However, most QDs are binary compounds composed of group II-VI, IV-VI, and III-V elements, leading to high toxicity and issues with biocompatibility.[143] Over the last decade, silicon nanocrystals (Si NCs) have emerged as a non-toxic, biocompatible alternative to these more commonly employed II-VI, IV-VI, and III-V semiconductor QDs.[124,125] Silicon is comparatively less expensive than other QDs as it is an earth-abundant material, making up about 28% of the earth's crust.[48,125,126] Moreover, planar silicon has dominated the microelectronics industry for decades, leading to widespread knowledge about its mechanical, electronic, and optical properties.[48,125,126] In addition to these qualities that motivate the use of Si NCs as an alternative to other QDs, Si NCs also present distinctive optical and electronic properties that are not present in the bulk material.

Si NCs have already found limited successful applications in biomedical imaging,[49] light-emitting diodes,[51] sensing,[52] and photodiodes.[50] However, the challenges associated with wide-spread implementation of Si NC-based materials stem from their susceptibility to oxidation and poor solution dispersibility.[16-18] To address these concerns, researchers have developed a myriad of covalent surface functionalization techniques for Si NCs utilizing thermal, radical-initiated, Lewis acid-mediated, photochemical, and microwave-heating methods.[48] In addition to improving passivation against oxidation and solution dispersibility, functionalization enables tuning of optical properties, development of purification techniques, and formation of various three-dimensional architectures.

Despite considerable progress in improving the passivation and solution dispersibility of Si NCs, there are few experimental demonstrations using Si NCs in optoelectronic applications.[128] The relative lack of examples has been attributed to the bulky, insulative alkyl chains that are used to yield solution-dispersible particles. These well-passivated surfaces are formed at the cost of reduced charge transport between NCs. However, with proper interfacial design, Si NCs may display a host of promising properties for optoelectronic applications, including ready absorption of photons and efficient exciton transport, tunable absorption and emission properties by NC size and functionalization, essentially defect-free surfaces for very small NC diameters, and the potential for multiple-exciton generation and hot carrier collection paradigms.[144] Thus, interfacial design is critical to the successful implementation of Si NCs in optoelectronic applications.

Researchers have explored several strategies for assembling Si NCs to enable more efficient energy harvesting. To date, the most promising methods encapsulate the NCs in either an amorphous inorganic matrix or an organic polymer blend to reduce the spacing between NCs. In the former strategy, a bulk heterojunction is formed at the interface of the inorganic matrix and the NCs. At this interface, excitons dissociate and then move between the NCs more efficiently due to the reduced QD spacing imposed by the inorganic matrix. Wang et al. demonstrated this concept with lead sulfide (PbS) QDs embedded within a zinc sulfide (ZnS) matrix.[145] This encapsulation resulted in a nearly 10-fold reduction of the QD spacing from over 100 nm to fewer than 15 nm, and afforded high stability through a facile solution-based *in situ* process. However, this method requires precise control over the NC size and spacing and has yet to be achieved with Si NC systems. In the latter encapsulation strategy, Si NCs are blended with an organic polymer, within which excitons can dissociate. This matrix can form an electron-selective or hole-selective contact with other materials based on the energy level alignment at the interface. Kortshagen et al. demonstrated this concept with Si NCs embedded in a P3HT matrix, which provided a large interfacial area in which the donor-acceptor separation was within an exciton diffusion length of the absorption site.[146] However, despite its appeal for solution processing, this method suffers from instability in ambient conditions and poor control over the interface morphology, lowering its overall practicality.[144]

These limitations motivate the development of an assembly method with more precise control over the NC spacing and enhanced stability of the system in ambient conditions. These goals may be realized through an alternative route in which Si NCs are assembled by covalently crosslinking the NCs via conjugated ligands (Figure 5.1). Synthesis of such a mesomaterial may result in promising optoelectronic properties such as improved hole transport through shorter, fixed distances between NCs. In addition, this assembly may yield greater charge separation, in which the conjugated crosslinking ligands provide a means for overcoming the high exciton binding energies present in Si NCs such that electrons can move through the ligand while holes are allowed to "hop" between NCs. Recently, the Lusk group demonstrated the viability and promise of such a system through computational studies for two Si_{147} NCs, showing that linkage by a single short, conjugated molecule increased carrier hopping rates by at least three orders of magnitude and outpaced photoluminescence rates.[144]

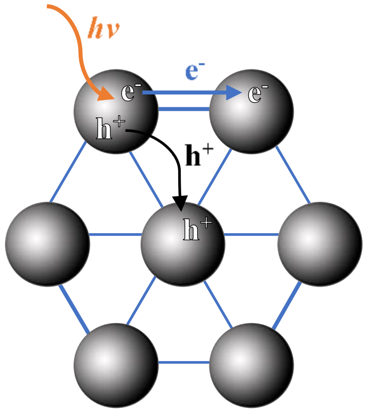

Figure 5.1 Schematic diagram of a novel optoelectronic mesomaterial based on an assembly of covalently crosslinked Si NCs (grey spheres). Photoexcitation (orange) of the material induces formation of an electron-hole pair. Here, charge separation follows such that holes (h^+) can hop across NCs while electrons (e^-) are transported through conjugated crosslinking ligands (blue).

Given these promising results, we propose to experimentally demonstrate these computational results through the synthesis of a novel optoelectronic mesomaterial. Our group has recently developed an oxidant-activated functionalization route that opens up new possibilities for synthesizing Si NCs with a wide variety of nucleophiles and Si linkages.[6] Thus, we will use this method to develop a mesomaterial comprised of Si NCs linked by short conjugated ligands and passivated by small methoxy groups. Herein, this report summarizes our progress in synthesizing and passivating these NCs, initial results in building the crosslinking ligand, and the outlook of this work toward achieving a mesomaterial with improved optoelectronic properties.

5.2 Experimental

Trichlorosilane (99%, Aldrich), anhydrous ethanol (200 proof, Koptec), hydrofluoric acid (49%, semiconductor grade, Transene), decane (≥99%, Sigma-Aldrich), 1-decene (94%, Aldrich), anhydrous methanol (99.8%, Sigma-Aldrich), anhydrous tetrahydrofuran (≥99.9%, Sigma-Aldrich), and 4-formylbenzoic acid (97%, Aldrich) were used as received. Water (resistivity ≥ 18.2 MΩ-cm) was obtained from a Barnstead E-pure system. Forming gas (5% hydrogen/balance nitrogen) and argon (ultra high purity 5.0 grade) were purchased from Airgas. Unless specified, solvents were purchased as ACS grade and used as received. Ferrocenium tetrafluoroborate (technical grade, Aldrich) was recrystallized prior to use. Quartz tubes (22 × 25 mm, 4 ft. length) were purchased from GM Associates, and quartz boats (100 mm L x 17 mm W x 10mm H) from MTI Corporation. Transmission electron microscopy grids (C-flat holey carbon grid, 1.2 μm hole, 1.3 μm space, 200 mesh) were purchased from Electron Microscopy Sciences.

5.2.1 Synthesis of Si NC/SiO_2 composite

A typical preparation of the Si NC/SiO_2 composite was accomplished in two steps: synthesis of a sol-gel polymer precursor and its subsequent thermal processing. The sol-gel polymer precursor $(HSiO_{1.5})_n$ was synthesized by first adding trichlorosilane (4.5 mL, 45 mmol) to a Schlenk flask and cooling to 0 °C under inert atmosphere (nitrogen or argon). While stirring vigorously, water (1.6 mL, 90 mmol) was added in one rapid injection while venting to remove hydrochloric acid vapors formed during the reaction, and the mixture was allowed to warm to room temperature for one hour. The resulting translucent white precipitate was then dried completely for at least three hours under vacuum. Due to its air-sensitivity, the sol-gel polymer must be used immediately after its synthesis. To prepare it for further processing, the large chunks of dried polymer were ground briefly (< 5 min.) via vigorous stirring under inert atmosphere, yielding a fine white powder.

The sol-gel polymer precursor was then quickly transferred to a quartz boat and heated in a 3-zone quartz tube furnace at a peak processing temperature of 1100 °C for 1 hour under a slightly reducing atmosphere provided by flowing forming gas (95% nitrogen/5% hydrogen) at a flow rate of ~5 mL/s. A ramp rate of 18 °C/min was used to reach the peak processing temperature. After heating, the composite was cooled to below 50 °C under forming gas flow before removal from the furnace.

5.2.2 Annealing of Si NC/SiO_2 composite for crystal growth

After removal from the furnace, the orange-brown Si NC/SiO_2 composite was first mechanically ground to a very fine powder using an agate mortar and pestle with sodium chloride salt in a ~2:1 mass ratio of composite to salt. To prevent the formation of particulate dust, the mixture was wetted with ethanol to form a brown slurry. The composite grains that flowed freely in the supernatant of the ethanol mixture were collected by pipette while the larger grains were ground further with more ethanol. The freely flowing composite suspensions were combined and centrifuged (3100 rpm, 12 min.). The supernatant was discarded, and the salt was removed by suspending the pellet in deionized water (~14 mL), followed by vigorously shaking and centrifuging the mixture using the same settings. This rinsing process was repeated twice more. To remove the water for more efficient drying, the pellet was rinsed with acetone or methanol and centrifuged. The supernatant was discarded, and ~1-3 mL of acetone were used to form a thick slurry of the composite that was then transferred by pipette to a scintillation vial. Completely drying the composite under gentle flowing air for at least 2 hours yielded approximately 800-900 mg of a very fine orange-brown powder.

Two methods were employed to grow the Si NCs: annealing by either varying the peak processing temperature or varying the peak processing time. In both procedures, the previously prepared composite was heated once more using nitrogen instead as the flowing gas delivered at a rate of ~5 mL/s. For both methods, the dry finely-ground orange-brown powder was first transferred to a quartz boat and loaded into the tube furnace. To grow the NCs using the former method, the composite was then heated using a ramp rate of ~18 °C/min. to a peak processing temperature of 1200 °C or 1250 °C. The composite was annealed at this temperature for 1 hour and then cooled under gas flow to below 50 ℃ before removal from the furnace to yield a brown composite.

In this report, most of the experiments use composites that were annealed by the latter growth method. Here, the finely-ground orange-brown powder was heated using a ramp rate of 18 ℃/min. to 1100 ℃ and then annealed at that temperature for a longer processing time ranging from 5-11 hours. The composite was then cooled to below 50 ℃ under gas flow before removal from the furnace to yield a brown composite.

5.2.3 Hydride-termination of Si NCs by etching with hydrofluoric acid

The hydride-terminated Si NC surface provides a highly reactive starting point for the majority of surface functionalization methods. In a typical procedure, the Si NC/SiO_2 composite (0.25 g) was added to a 50 mL polymethylpentene (PMP) beaker with a Teflon stirbar. The powder was then suspended by sonication for 30-60 seconds in a solvent mixture of ethanol and water (1:1 v/v, 6 mL total). To this, hydrofluoric acid (3 mL) was added, and the brown mixture was stirred for 1 hour under subdued light. The completion of the etching process can be qualitatively confirmed by the golden color of the mixture.

The liberated, hydrophobic Si NCs were then extracted with a nonpolar solvent, i.e., toluene (3 × 15 mL) or decane (1 × 15 mL) and 1-decene (1 × 15 mL). When extracted with decane and 1-decene, the hydride-terminated NCs were immediately used in thermal hydrosilylation reactions. For hydride-terminated NCs extracted with toluene, the suspensions were centrifuged (2170 rpm, 10 min.), and the supernatant was quickly removed. The NC pellets were then combined, suspended in 15 mL of toluene, and centrifuged using the same settings for a rinsing process that was repeated a total of 2 times. The final pellets of hydride-terminated Si NCs were then suspended in 25 mL of anhydrous tetrahydrofuran for use in oxidant-activated nucleophilic addition reactions.

5.2.4 Functionalization of Si NC surfaces with 1-decene

The hydride-terminated Si NCs extracted with decane and 1-decene in the previous section were collected in an oven-dried Schlenk flask under a nitrogen atmosphere. Dissolved gases were then removed from the cloudy golden solution with three freeze, pump, thaw cycles. While stirring, the degassed solution was heated at 170 ℃ for 24 hours under a nitrogen atmosphere. Subsequent cooling to room temperature yielded a transparent golden solution that was centrifuged (3100 rpm, 10 min) to form a very small brown pellet that is believed to be colloidally unstable large Si NCs and other decomposition products.

The solvent and unreacted ligand was removed from the collected supernatants by rotary evaporation, leaving an orange solid that was then dissolved in toluene. To remove trace grease impurities, the dissolved Si NCs were then purified further by anti-solvent precipitation with methanol followed by centrifugation (3100 rpm, 15 min), and the process was repeated twice more. The purified functionalized Si NCs were suspended in toluene for further characterization.

5.2.5 Functionalization of Si NC surfaces with methanol

The hydride-terminated Si NCs extracted with toluene and suspended in 25 mL of anhydrous tetrahydrofuran in Section 5.2.3 were transferred to an oven-dried Schlenk flask and maintained under inert atmosphere (nitrogen or argon). Dissolved gases were removed from the cloudy golden solution with three freeze, pump, thaw cycles. During this process, a 1 mM oxidant solution was prepared by dissolving ferrocenium tetrafluoroborate (Fc^+) with a small excess (3.0 mg, 0.011 mmol) in anhydrous methanol (10 mL). The blue oxidant solution was similarly degassed with three freeze, pump, thaw cycles. After the Si NC suspension completely warmed to room temperature, the flask was wrapped in aluminum foil, and 1.0 mL of the Fc^+ solution was quickly added by syringe. The reaction mixture was stirred for 30 min. or 24 hours at room temperature under inert atmosphere.

Following the reaction, the foil was removed, and the solvent and unreacted ligand was removed *in vacuo* until only ~3 mL remained. The NCs were then purified by suspension in the following solvent mixture: 10 mL ethanol, 1 mL methanol, 0.5 mL toluene, followed by centrifugation (3100 rpm, 7-8 min). The supernatant was removed, and the rinsing process was repeated for a total of 3 times. The resulting pellet of NCs was rinsed with 12 mL of methanol and centrifuged using the same settings. The supernatant was then removed, and a small portion of the functionalized Si NCs were suspended in toluene for further characterization.

5.2.6 Functionalization of Si NC surfaces with methanol and 4-formylbenzoic acid

The hydride-terminated Si NCs extracted with toluene and suspended in 25 mL of anhydrous tetrahydrofuran in Section 5.2.3 were transferred to an oven-dried Schlenk flask and maintained under an argon atmosphere. Dissolved gases were removed from the cloudy golden solution with three freeze, pump, thaw cycles. During this process, a 2, 10, or 100 mM ligand solution was prepared by dissolving the respective amount of 4-formylbenzoic acid (6.0 mg, 0.040 mmol; 15 mg, 0.10 mmol; 150 mg, 1.0 mmol) in anhydrous methanol (20 mL; 10 mL; 10 mL). The clear solution was then similarly degassed with three freeze, pump, thaw cycles. After the Si NC suspension completely warmed to room temperature, the flask was wrapped in aluminum foil, and solid Fc^+ (300 mg, 1.10 mmol) was added directly to the flask. The mixture was stirred for 2 min. under an argon atmosphere, and then 1.5 mL of the ligand solution was quickly added by syringe. The reaction was allowed to proceed for 24 hours at room temperature under an argon atmosphere.

Following the reaction, the foil was removed, revealing a dark blue-green mixture. The solvent and unreacted ligand was removed *in vacuo* until only ~3 mL remained, and the NCs were then purified by suspension in the following solvent mixture: 10 mL ethanol, 1 mL methanol, 0.5 mL toluene. The dark mixture was shaken vigorously and centrifuged (2480 rpm, 12 min.), and the supernatant was carefully removed and discarded. The NCs were rinsed using this process two more times, then similarly rinsed once with 12 mL methanol, yielding a dark brown pellet of functionalized Si NCs. The supernatant was discarded, and a small portion of the Si NCs was also dissolved in a variety of solvents ranging in polarity index for further characterization.

5.2.7 Instrumentation

The infrared (IR) spectra were collected by performing attenuated total reflectance Fourier transform infrared spectroscopy (ATR-FTIR) on a Thermo Scientific Nicolet 6700 optical spectrometer equipped with a thermoelectrically cooled deuterated *L*-alanine-doped triglycine sulfate (DLaTGS) detector, an electronically temperature-controlled (ETC) EverGlo mid-IR source, a nitrogen gas purge, and a KBr beam splitter. Functionalized Si NCs were drop casted onto a diamond window.

Powder X-ray diffraction (XRD) patterns were collected on a Bruker D2 Phaser equipped with a copper tube and LynxEye 1-dimensional detector with a 2.3° Soller slit. Samples were prepared by drop casting onto a silicon crystal specimen holder or by filling specimen well of a PMMA ring with dry powder. Patterns were measured using a step size of 0.01 2θ, variable rotation of 5.0 min^{-1}, and X-ray generation with 30 kV voltage and 10 mA current.

Transmission electron micrographs (TEM) were obtained using a FEI Tecnai F30ST electron microscope with an accelerating voltage of 300 kV and equipped with a high angle annular dark field detector and a Gatan Ultra Scan 1000XP camera. TEM samples were prepared by drop casting the Si NC suspension in toluene on a holey carbon-coated Cu grid. The NC size distributions were determined using ImageJ (version 1.51).

5.3 Results and Discussion

5.3.1 Synthesis of Si NCs with controllable crystal growth by reductive thermal processing

Si NCs embedded in an oxide matrix were successfully synthesized by procedures outlined by the Veinot group, involving the reductive thermal processing of the sol-gel condensation polymer $(HSiO_{1.5})_n$ at 1100 °C for 1 hour.[47] ATR-FTIR was employed the investigate the chemical composition of these materials. Figure 5.2a shows the FTIR spectra of the sol-gel polymer $(HSiO_{1.5})_n$, with a characteristic sharp Si–H stretching vibration at ca. 2255 cm^{-1}, strong Si–O–Si vibrations from ca. 1000-1300 cm^{-1}, and H–Si–O hybrid vibrations from ca. 800-900 cm^{-1}. These results correspond well to the FTIR spectra reported by Henderson et al.[47] Figure 5.2b displays the FTIR spectra of the Si NC/SiO_2 composite formed upon thermal processing of the polymer precursor, with an intense broad Si–O–Si vibration from 900-1300 cm^{-1} and lacks the Si–H stretch of $(HSiO_{1.5})_n$. These results indicate the polymer was successfully converted to an oxide matrix upon thermal processing.

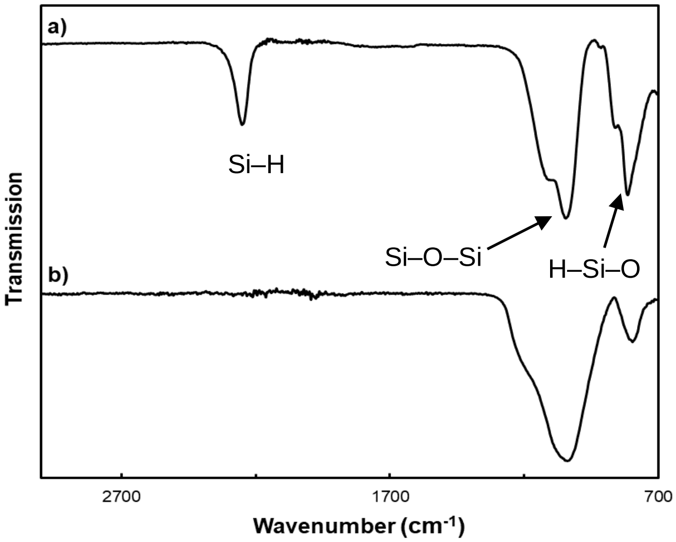

Figure 5.2 ATR-FTIR spectra of (a) $(HSiO_{1.5})_n$ polymer precursor and (b) Si NC/SiO_2 composite after reductive thermal processing. Disappearance of the Si–H peak at 2255 cm^{-1} indicates successful conversion from the polymer to the composite.

The Si NCs were also initially grown using a method reported by the Veinot group, in which the composites are first ground and then reprocessed at a higher temperature for 1 hour under an inert atmosphere.[47] XRD is a method widely-employed to assess the quality of the synthesized Si NC/SiO_2 composite and qualitatively monitor nanocrystal growth.[48] XRD patterns for the Si NC/SiO_2 composites synthesized at initially 1100 °C and then further processed at 1200 °C or 1250 °C are shown in Figure 5.3. All composites display broad reflections at ca. 28°, 47°, and 56°, which can be readily indexed to the (111), (220), and (311) crystal planes of silicon.[47] Furthermore, the patterns illustrate clear peak broadening and increased intensity upon reheating the initial composite, but minimal change is observed between composites reheated at 1200 °C versus 1250 °C. This change can likely be attributed to the similar size distribution of the embedded Si NCs when reprocessed at these temperatures.

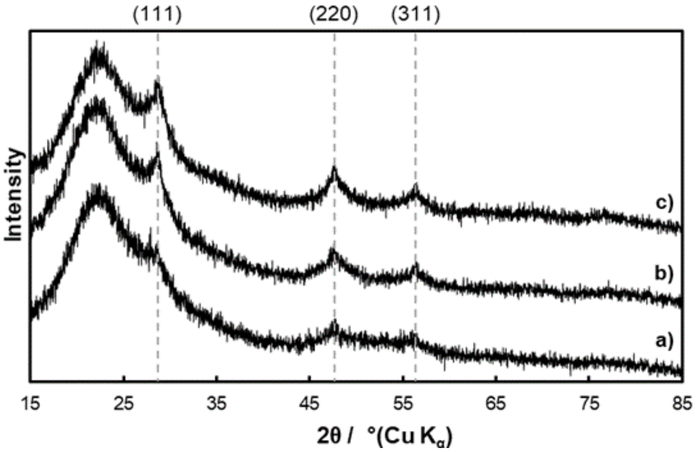

Figure 5.3 XRD patterns of (a) initially synthesized composite from thermal processing of polymer at 1100 °C, and composites subsequently reheated at (b) 1200 °C or (c) 1250 °C. All patterns display characteristic reflections indexed to the (111), (220), and (311) crystallographic planes of Si diamond structure. Clear peak broadening and intensification is shown for reheating the initial composite, but minimal change is observed between composites reheated at 1200 °C versus 1250 °C.

Hydride-terminated Si NCs were liberated by etching the oxide matrix grown at 1250 °C with hydrofluoric acid. Figure 5.4 shows the FTIR spectra of the Si NCs embedded in the oxide matrix and the hydride-terminated Si NCs. After etching, the Si–O–Si vibrations from 900-1300 cm^{-1} disappeared, and the hydride-terminated Si NCs display new stretching and scissoring frequencies at ca. 2100 and 910 cm^{-1} that are characteristic of Si–H,[47] indicating successful removal of the matrix. This result is further validated by XRD; the large broad peak associated with amorphous oxide decreases upon etching, indicating the removal of the matrix (Figure 5.5).

Following release of the hydride-terminated Si NCs, ferrocenium-activated methoxylation was attempted following procedures reported by Dasog et al. to achieve passivation of the Si NCs for use in our mesomaterial.[6] The reaction proceeds by the transfer of an electron from the Si NC to the oxidant when the following conditions are met: 1) the solution redox energy is less than the surface resonance energy and 2) the solution redox energy is below or near the valence band edge of the Si NC.[6] The first condition is met for all Si NC sizes, but the valence band edge shifts to more negative energies as the NC size decreases. Thus, smaller NCs with valence band edges below the redox energy of ferrocene/ferrocenium will not undergo methoxylation. Although the methoxylation procedure appeared straightforward, characterization of the functionalized particles by IR spectroscopy showed that the initial attempt resulted in incomplete methoxylation as evidenced by a residual sharp Si–H peak. This result indicated that the size of the Si NCs may present a challenge in achieving a well-passivated surface.

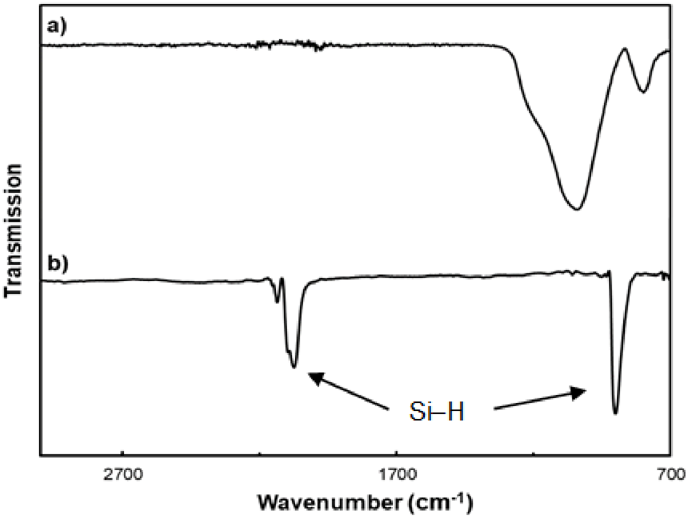

Figure 5.4 ATR-FTIR spectra of (a) Si NC/SiO$_2$ matrix and (b) hydride-terminated Si NCs after etching with hydrofluoric acid. Disappearance of the Si–O–Si peak at 900-1300 cm^{-1} and appearance of Si–H frequencies at ca. 2100 and 910 cm^{-1} indicate successful etching of the oxide matrix.

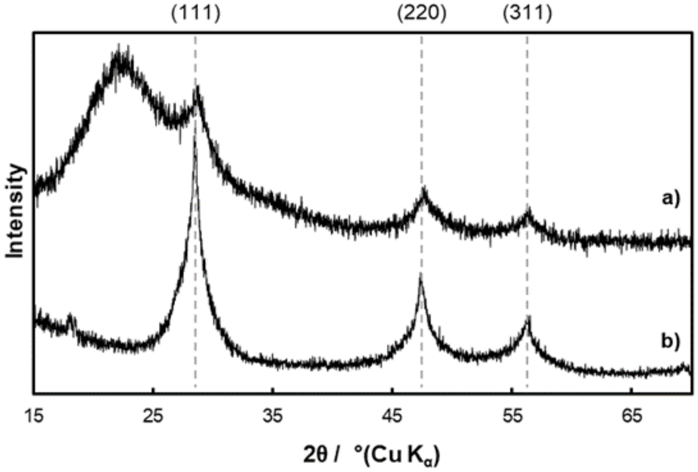

Figure 5.5 XRD patterns of (a) Si NC/SiO$_2$ composite reprocessed at 1250 °C and (b) hydride-terminated Si NCs after hydrofluoric acid etching. Reduction of the large broad peak associated with amorphous oxide indicates successful removal of the matrix and release of the Si NCs.

Because the functionalization route is size-dependent and was previously demonstrated for NCs of approximately 8 nm in diameter, we investigated the size distribution of the hydride-terminated NCs by TEM. Figure 5.6 shows representative TEM images in which the crystalline structure of the particles can be observed at high magnification. However, the hydride-terminated surface renders the NCs colloidally unstable, so the NCs tend to form secondary aggregates upon drop casting as evidenced by the imaged NC films. This agglomeration presents a significant challenge in determining the size distribution of our particles, as the NCs cannot be easily distinguished from one another. Moreover, the large NCs used within the ferrocenium-activated methoxylation study were grown at higher temperatures than our furnace could achieve. Thus, the incomplete functionalization may have resulted from using particles that were too small for the chosen oxidant. Similarly, using NCs with a wide size distribution may have led to incomplete methoxylation for smaller nanoparticles than the oxidant could activate. To resolve these issues, three modifications were made to the Si NC synthesis procedure.

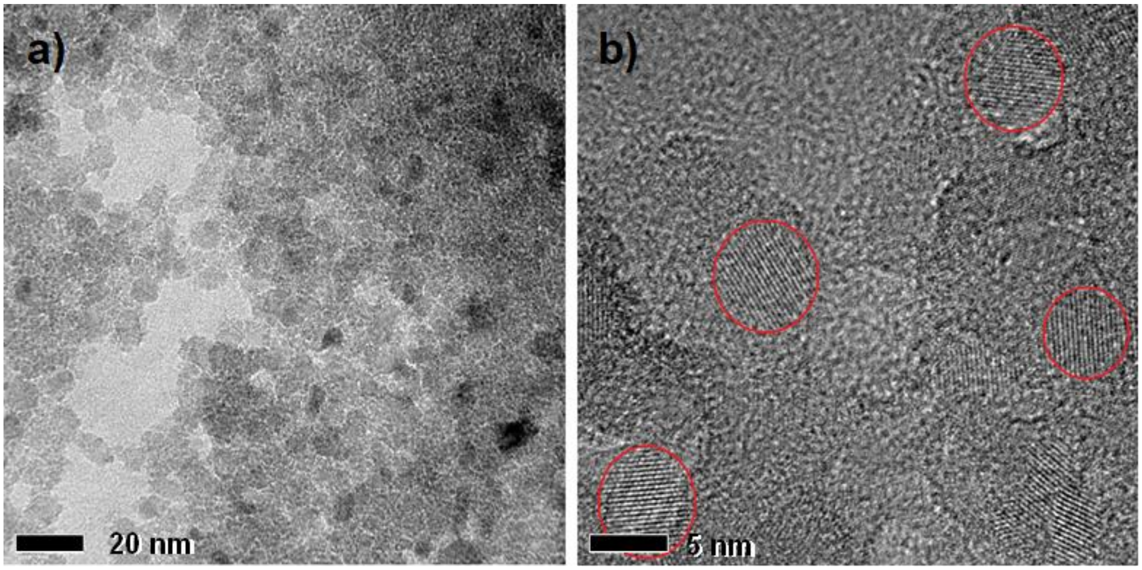

Figure 5.6 TEM of hydride-terminated Si NCs grown at 1250 °C. (a) Poor colloidal stability of the NCs yields secondary aggregates upon drop casting, and (b) magnification displays Si NC films. This agglomeration presents a challenge in obtaining the size distribution due to difficulty in distinguishing individual NCs.

We addressed the first challenge in controlling the average particle diameter during crystal growth by extending the peak temperature processing time instead of the peak processing temperature to induce Si NC growth. Various sol-gel polymer precursors may be used to synthesize Si NC/SiO_2 composites. The reductive thermal disproportionation of the precursors leads to elemental Si that diffuses through the oxide matrix to form Si-rich nanodomains that eventually crystallize and grow to yield Si NCs.[147] This growth mechanism may be influenced by the structure of the polymer precursor, which affects the diffusion kinetics of the Si atoms within the oxide matrix.[147] The $(HSiO_{1.5})_n$ precursor used in this work possesses a network structure (Figure 5.7a). It was found that Si NCs in a silicon oxycarbide (SiOC) glass derived from a similarly structured polysiloxane precursor could be grown by increasing the peak temperature processing time.[148] In contrast, hydrogen silsesquioxane (HSQ) possesses a more open cage structure (Figure 5.7b) that was shown to initially yield larger Si NCs, but these NCs could not be grown further using the same method. These differing observations suggest that the precursor structure can influence the NC growth. Because our precursor possesses a network structure like that used to derive the SiOC glass, we anticipated that we could grow our Si NCs using a similar method.

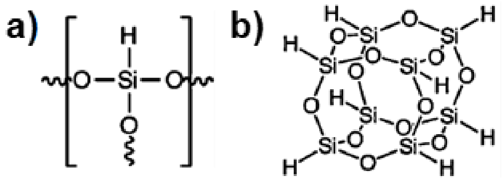

Figure 5.7 The polymer precursors (a) $(HSiO_{1.5})_n$ (network struture) and (b) HSQ (cage structure) possess different structures that may impact the growth mechanism of Si NCs by affecting the diffusion kinetics of Si atoms within the oxide matrix.

To improve the size distribution of the Si NCs, Si NC/SiO_2 composites must be ground to reduce the grain size and maximize their homogeneity.[48] Otherwise, non-uniform grains will complete etching and release the embedded Si NCs at different rates, such that the freestanding NCs also begin etching and decreasing in size while additional Si NCs are released. These different rates of etching completion effectively widen the size distribution and may hinder the oxidant-activated functionalization route. Thus, we increased the homogeneity of our composite grains by manually grinding them with sodium chloride salt prior to etching, which has been previously shown to ensure narrow NC size distributions.[47]

Finally, to resolve the challenge in attaining images of disperse Si NCs for statistical analysis, we functionalized the Si NCs with 1-decene by thermal hydrosilylation.[149] This functionalization route was selected for its facile synthesis and purification procedures that yield good surface coverage. Additionally, the size-independent nature of the reaction allows for more accurate determination of the NC size distribution by including smaller

NCs that could not be rendered dispersible by oxidant-activated functionalization.[48] Using the three techniques discussed, we processed different Si NC/SiO_2 composites for 5, 6, and 7 hours at 1100 °C.

From Figure 5.8, TEM showed that this procedure afforded NCs with good colloidal stability, such that individual particles could be distinguished for more efficient and accurate diameter measurement. Figure 5.9 shows that processing times of 5, 6, and 7 hours yielded size distributions of 7.6 ± 1.5 nm (83 particle count), 8.0 ± 1.5 nm (176 particle count), and 8.8 ± 1.8 nm (282 particle count), respectively. This data indicates that we successfully controlled the NC growth by extending the thermal processing period of our composites. However, these measurements may be susceptible to possible overestimation due to the low image contrast and very small particle size relative to the TEM carbon grid background. Nevertheless, this process could feasibly provide particles of suitable diameter and size distribution to carry out oxidant-activated methoxylation and achieve passivation of the NC mesomaterial.

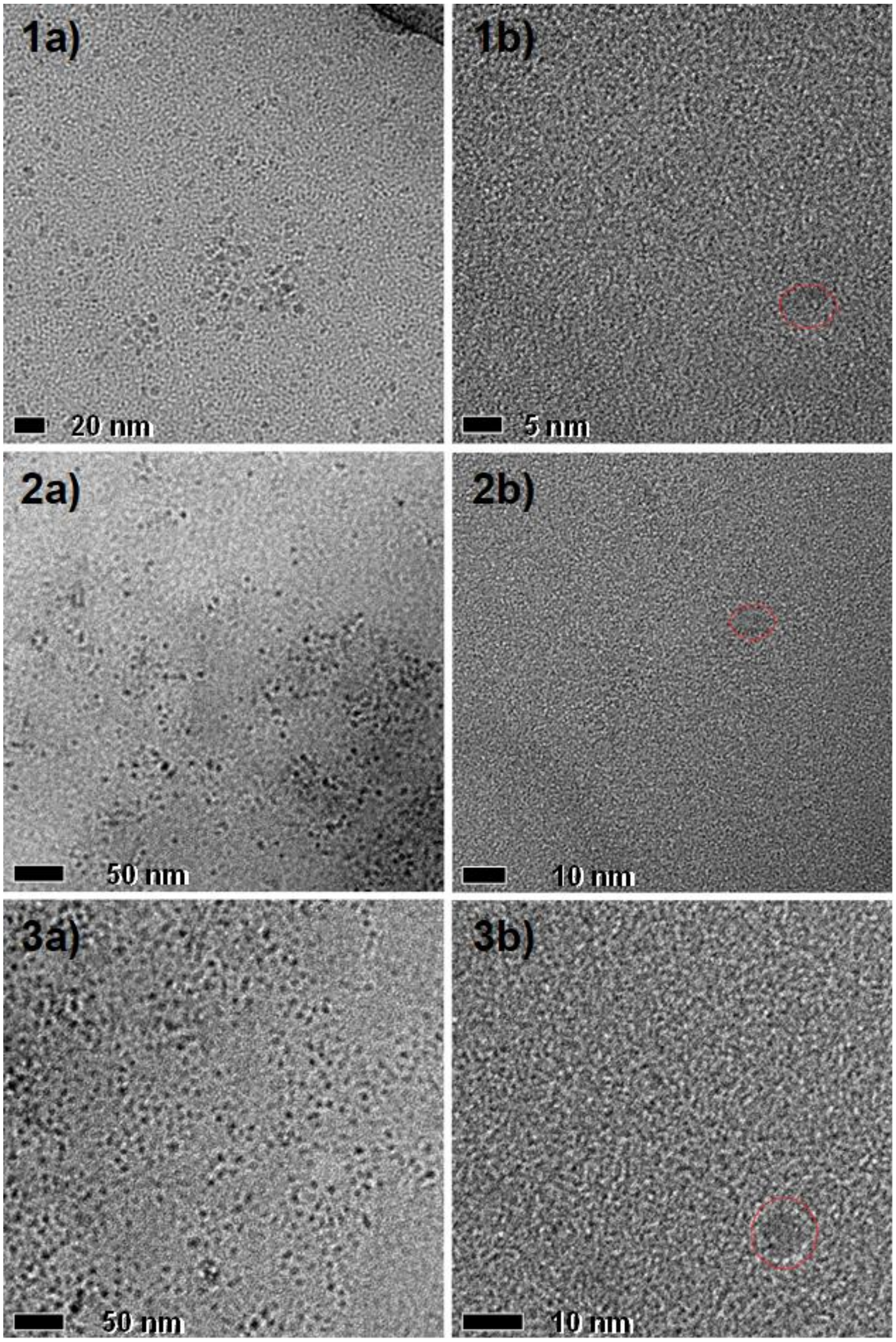

Figure 5.8 TEM of Si NCs functionalized with 1-decene using Si NC/SiO$_2$ composites thermally processed for (1a) 5 h, (2a) 6 h, and (3a) 7 h at 1100 °C demonstrate good colloidal stability allowing for efficient size measurement of individual particles. Magnification of the particles displays their crystalline lattice (1b, 2b, 3b).

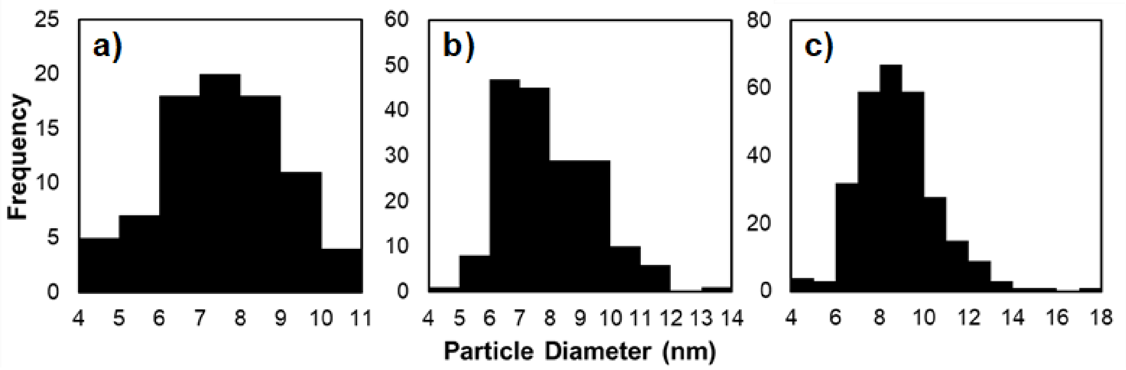

Figure 5.9 Size distributions of Si NCs taken by measuring the particle diameter along its longest dimension. Heating at a peak temperature of 1100 °C for (a) 5 h, (b) 6 h, and (c) 7 h afforded NCs with size distributions of 7.6 ± 1.5 nm (83 particle count), 8.0 ± 1.5 nm (176 particle count), and 8.8 ± 1.8 nm (282 particle count), respectively. This trend indicates that increasing the processing time yields controllable crystal growth.

5.3.2 Methoxy-terminated surface functionalization of Si NCs

The hydride-terminated Si NCs grown at longer processing times were methoxylated through ferrocenium-activated functionalization in the dark under an inert atmosphere. Figure 5.10 displays the ATR-FTIR spectra for the functionalized Si NCs that were grown for 6, 7, 10, and 11 hours at 1100 °C. Upon comparison to IR spectra taken for methanol by Falk and Whalley,[150] the spectra for our methoxylated-Si NCs displayed characteristic C–H stretches at ~2925 cm^{-1}, weak C–H bending vibrations at ~1445 cm^{-1}, and strong C–H rocking vibrations at ~1256 cm^{-1}. The C–O stretching vibration that was previously reported at ~1029 cm^{-1} may be convoluted with the Si–O–Si vibration from ~915-1205 cm^{-1}. Residual Si–H vibrations were observed at 2100 and 910 cm^{-1} for functionalized NCs that were grown for 6, 7, and 10 hours, but are nearly absent for NCs grown for 11 hours.

Although statistical analysis showed that Si NCs grown for 6 hours possessed a size distribution matching the distribution used in previous reports, incomplete methoxylation indicated that the particle size may have been overestimated due to the difficulties in imaging the Si NCs, so the NCs were further grown using longer processing times. We observed the trend that the C–H stretch increased in intensity relative to the Si–H stretch, indicating that with growing NC size, ferrocenium-activated oxidation achieved more complete methoxylation. This observation corresponded well to the results reported by Dasog et al. for the dependence of methoxylation completion on NC size.[6] The inset shown in Figure 5.10 shows the qualitative red-orange photoluminescence of the successfully methoxylated NCs in toluene under UV-excitation, demonstrating the good colloidal stability of the NCs that remains even after storage under ambient conditions for a few days.

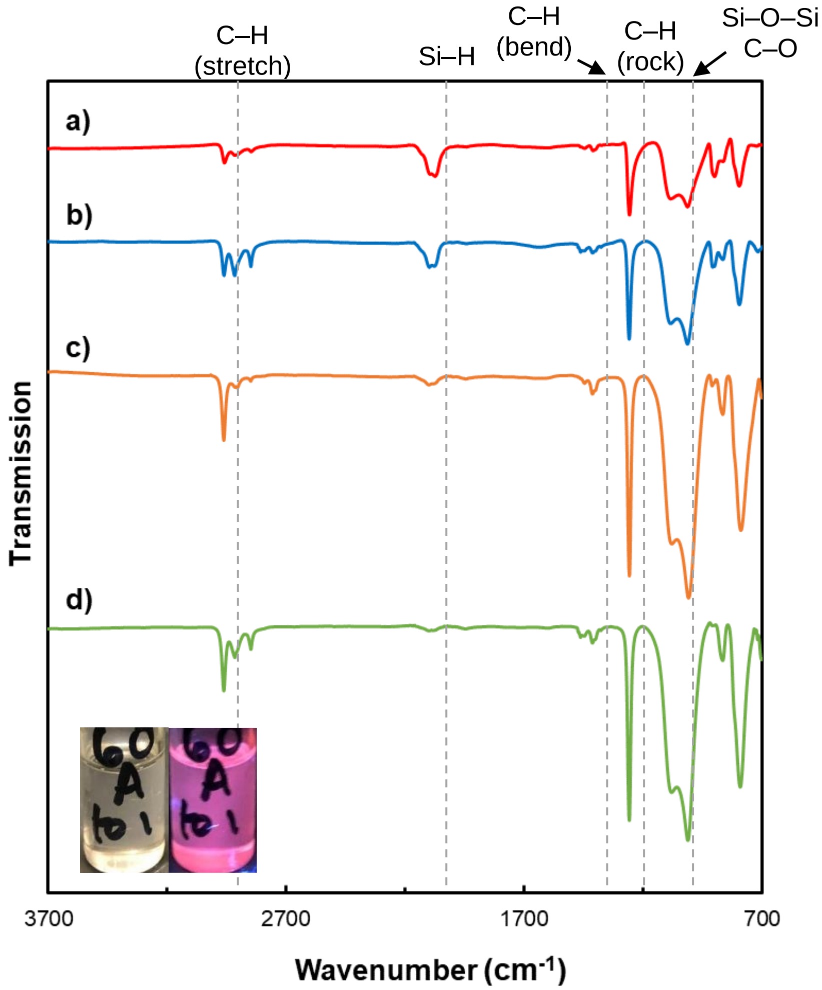

Figure 5.10 ATR-FTIR spectra of the methoxylated Si NCs grown from composites thermally processed at 1100 °C for (a) 6 h, (b) 7 h, (c) 10 h, (d) 11 h. Characteristics C–H vibrations observed at ~2925, ~1445, and ~1256 cm^{-1}. Expected C–O stretch at ~1029 cm^{-1} may be convoluted with Si–O–Si stretch from ~910-1205 cm^{-1}. Relative intensity of C–H stretch and Si–H stretches at 2100 and 910 cm^{-1} indicate greater methoxylation completion with increasing NC size. Inset displays photoluminescence of methoxylated Si NCs (11 h grown) in toluene under UV irradiation.

5.3.3 Mixed monolayer functionalization of Si NCs with 4-formylbenzoic acid and methanol

After achieving methoxylation of the Si NCs that will provide passivation for the desired mesomaterial, we ran initial reactions aiming to build the crosslinking ligand illustrated by

Figure 5.11 by a two-step imine formation from dehydration of a carbinolamine intermediate. To simplify the required characterization, we divided the process into two orthogonal steps: functionalization of the Si NCs with a molecule containing exposed aldehyde groups, and subsequent reaction of these groups with a diamine to yield the imine crosslinking ligand.

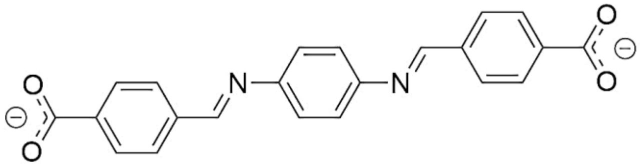

Figure 5.11 Crosslinking ligand to be employed in the Si NC mesomaterial synthesis. The ligand will be formed by oxidant-activated addition of 4-formylbenzoic acid to the Si NCs followed by imine formation upon p-phenylenediamine addition.

This procedure presents several synthetic advantages that enable more efficient characterization over using a single molecule with two binding sites to form the linkage between NCs. In the first step, we can employ oxidant-activated addition of a molecule containing a nucleophilic group as well as the aldehyde group, i.e., 4-formylbenzoic acid, in order to control and ensure the aldehyde groups remain unbound and available for the following imine formation reaction. Second, the crosslink formed upon addition of the diamine forms a nitrogen linkage that can be readily characterized by ATR-FTIR, XPS, and solid-state NMR. Because this reaction is not carried out using oxidant-activated addition, these nitrogen bonds can only form upon crosslinking rather than during the initial functionalization step, which provides a simpler route for characterizing and confirming synthesis of the desired mesomaterial.

The first step of the crosslinking procedure utilizes the oxidant-activated addition of 4-formylbenzoic acid and methanol (Figure 5.12) to produce a mixed monolayer where 4-formylbenzoic acid provides the building block of the crosslinking ligand and methoxylation passivates the NCs. Figure 5.13 shows the ATR-FTIR spectra of Si NCs grown for 11 hours and functionalized by the oxidant-activated addition of the aldehyde in concentrations of 2, 10, and 100 mM in methanol under an inert atmosphere in the dark. Broad peaks from approximately ~1500-1800 cm^{-1} not present on simply methoxylated surfaces appear for all aldehyde concentrations. For the addition of 10 and 100 mM aldehyde solutions, we also observe that peaks corresponding to methoxylated particles increased in intensity when the aldehyde concentration was decreased. It is well-known that vibrations associated with aldehyde and carboxylate groups typically appear from approximately 1630-1740 cm^{-1},[151] which lies within the range that we observe the new vibrations, making it likely that 4-formylbenzoic acid was added to the surface. However, further characterization with XPS and solid-state NMR of the exact monolayer composition is still needed to confirm this hypothesis. Figure 5.14 displays images of the Si NCs reacted with a 10 mM aldehyde solution dispersed in solvents of ranging polarity index (i.e., THF, dimethyl sulfoxide (DMSO), *N*,*N*-dimethylformamide (DMF), ethanol, and isopropyl alcohol (IPA)) under visible and UV-radiation. Weak photoluminescence was observed for Si NCs dispersed in DMSO and DMF, but it is still unclear whether this photoemission originates from functionalized NCs.

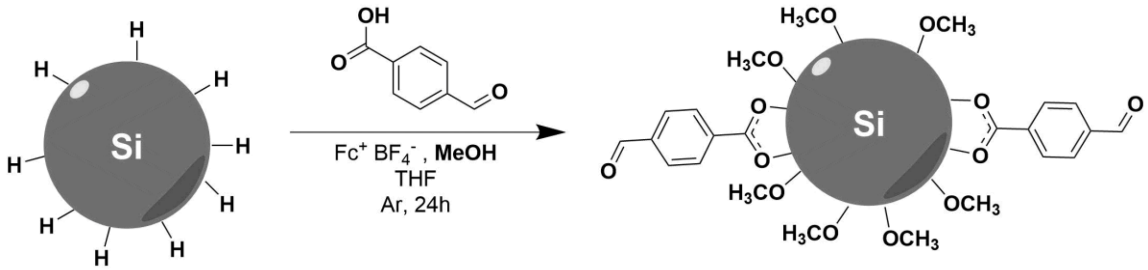

Figure 5.12 Synthetic scheme for the mixed monolayer functionalization of Si NCs with 4-formylbenzoic acid and methanol under argon via ferrocenium-activated nucleophilic addition.

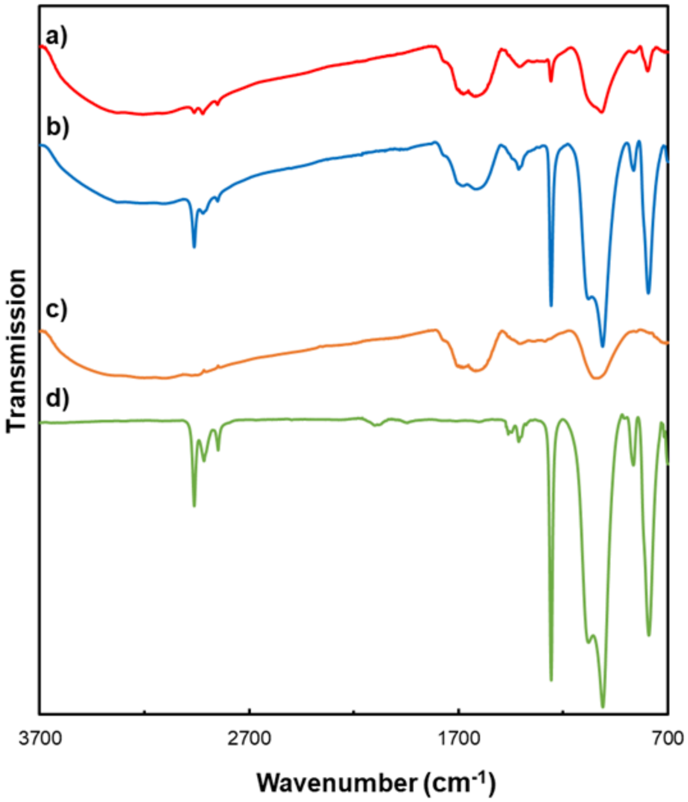

Figure 5.13 ATR-FTIR spectra of 11h-grown Si NCs reacted with 4-formylbenzoic acid in concentrations of (a) 100 mM, (b) 10 mM, and (c) 2 mM in methanol through ferrocenium-activated addition under inert atmosphere in the dark. (d) Methoxylated Si NC IR spectra is provided for comparison. New vibrations observed in ~1500-1800 cm^{-1} range that may be associated with carboxylate and aldehyde groups, but further characterization is still required to confirm this hypothesis.

Figure 5.14 Images of Si NCs reacted with 10 mM aldehyde in methanol solution under visible light (top) and under UV light (bottom). The NCs are dispersed in solvents of varying polarity, i.e., THF, DMSO, DMF, ethanol, and IPA (left to right). Weak photoluminescence observed for dispersion in DMSO and DMF, but its origin is still unclear.

5.4 Conclusions and Outlook

We have reported our efforts toward the synthesis of a novel Si NC mesomaterial passivated by methoxylation and comprised of particles linked together by a short conjugated molecule through imine formation. The size distribution and average particle diameter of Si NCs was controlled by extending the thermal processing time at 1100 °C of Si NC/SiO_2 composites synthesized from the thermal disproportionation of the polymer precursor $(HSiO_{1.5})_n$. Using this method to grow the Si NCs, we then achieved ferrocenium-activated methoxylation of Si NCs with good solution dispersibility as confirmed by ATR-FTIR. This methoxylation was a necessary step to passivate the desired mesomaterial. We then began building the ligand that would link the Si NCs to each other by a two-step orthogonal process involving imine formation through the reaction of exposed aldehydes to a diamine. We reported the preliminary ATR-FTIR spectral results of the first step of this crosslinking procedure, in which we aimed to synthesize Si NCs with exposed aldehydes by reacting hydride-terminated NCs with various concentrations of 4-formylbenzoic acid in methanol. Although the exact composition of the surface monolayer of the Si NCs cannot be confirmed by ATR-FTIR spectroscopy alone, new peaks within the 1500-1800 cm^{-1} range appeared along with IR vibrations matching those of the methoxylated surface. The clear change in the IR spectra for these reactions holds promise for the possible achievement of a mixed monolayer. Further work will determine whether this bond vibration can be definitively associated with the aldehyde and carboxylate group by characterization with XPS and solid-state ^1H and ^{13}C NMR.

Upon successful binding of a ligand containing exposed aldehyde groups to Si NCs, reacting these aldehydes by imine formation will build the conjugated crosslinking ligand. To achieve this, *p*-phenylenediamine will be added to the functionalized NCs and heated to drive the dehydration reaction to completion (Figure 5.15). ATR-FTIR spectroscopy, XPS, and solid-state ^1H and ^{13}C NMR spectroscopy will be employed to characterize this linkage by the appearance of C–N in the IR spectra, a new nitrogen peak in the N 1*s* XP spectrum, and the disappearance of the aldehyde signal in the NMR spectra.

Once we can achieve a mesomaterial comprised of Si NCs crosslinked by a conjugated molecule, we will devise fabrication methods to form films of the mesomaterial. The film morphology and Si NC spacing will be characterized by microscopy and X-ray scattering techniques. These films will then be used to investigate the effect of crosslinking on the carrier mobilities and on solar cell performance using device fabrication and characterization methods analogous to those employed for colloidal lead sulfide quantum dot inks.[152]

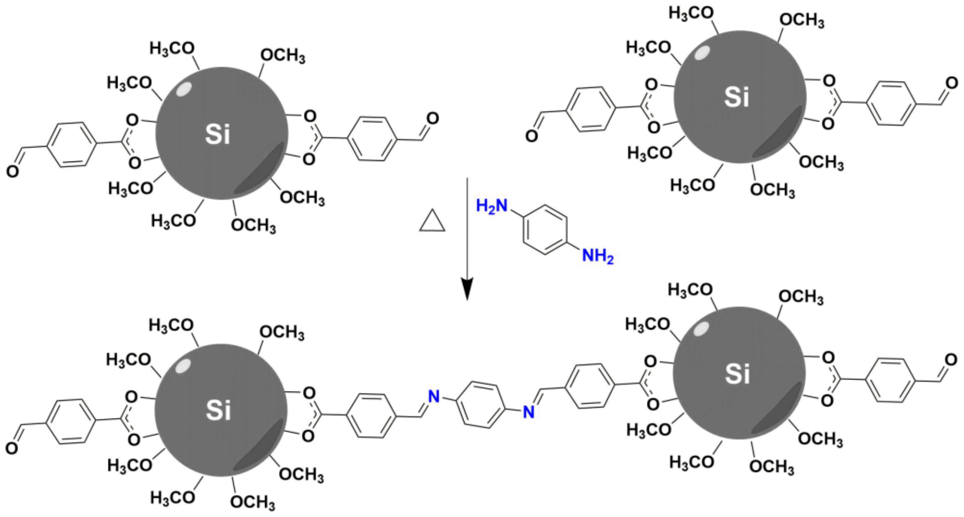

Figure 5.15 Synthetic scheme for building crosslinking ligand by imine formation upon addition of p-phenylenediamine to exposed aldehydes on functionalized Si NCs, where heat is used to drive the reaction to completion.

Appendix

Calculations used in Chapter 2

1. DFT Modeling of Grand Canonical Potential Free Energy

We used a published method to relate traditional Quantum Mechanics (QM), where the number of electrons is fixed throughout a reaction, to Grand Canonical QM, where the potential is fixed by allowing the charge to change. This method, called Grand Canonical Density-function Theory (GC-DFT), allows us to model reactions at fixed potential to make comparisons with experimental data. The relationship between the voltage-dependent grand canonical potential (GCP) for surface states can be derived from traditional fixed-electron free energies using a Legendre transformation.[10] The result is that GCP depends quadratically on the applied potential (U) and on the number of electrons, allowing a continuous description of the evolution of the initial state, final state, and transition state of a reaction with respect to potential, shown in Eq. 1:

$$G(n; U) = F(n) - ne(U_{\mathrm{SHE}} - U) \qquad (1)$$

where G is the grand canonical free energy, which depends on the applied voltage U vs SHE and the number of electrons n, e is the unit electronvolt in energy, F is the total free energy as a function of n, and U_{SHE} is the electronic energy at the standard hydrogen electrode (SHE) condition which is –4.44 V. U is defined such that the sign relates directly to the experimental potential, i.e., $U = 0.4$ V corresponds to 0.4 V vs SHE. For $G(n; U)$ to be used as a *thermodynamic* potential, the number of electrons in the system must be equilibrated to the applied voltage and in order to obtain the value of G at equilibrium, $F(n)$ must be minimized with respect to n, and thus the form of $F(n)$ must be at least quadratic. Although $F(n)$ appears to be linear with respect to n, as shown in the top row of plots in Figure 2.4, this apparent linearity is largely due to the linear contribution of the free energy of electrons. Linearly correcting for the free energies of electrons by plotting $F(n) - nU_{\mathrm{SHE}}$ as shown in the plots in the bottom row of Figure 2.4 reveals that $F(n)$ is quadratic with respect to n.

To determine how the potential varies with charge for a particular state along the reaction, whether it is the initial state, final state, or transition state of a reaction, we fitted $F(n)$ quadratically to obtain the quadratic coefficients a, b, and c that can then be used to calculate the thermodynamic GCP free energy by Eq. 2:

$$F(n) = a(n - n_0)^2 + b(n - n_0) + c \quad (2)$$

where n_0 is the number of electrons in a neutral system.

To obtain the coefficients a, b, and c specific of the structures (all initial, transition, and final states) mentioned in this thesis, we obtained the optimized geometries using VASP at charges that span the potential of interest, then used jDFTx with CANDLE solvation to obtain the free energy and potential (V vs SHE) of the optimized geometry. The fluid was modeled to include fluoride anion and potassium cation components at concentrations of 0.1 M. Figure 2.4 shows the fitting for $F(n) - nU_{\mathrm{SHE}}$ vs $n - n_0$ for the initial states, transition states, and final states for the reactions MoS_2 + $ClCH_3$ on S7 (a low-S sulfur), and on S10 (a high-S sulfur). The initial states and final states for MoS_2 reactions involving one or more sulfurs on the surface were also fitted using this method.

2. Conversion from JDFT Output to Electrochemical Potential

To convert μ, the potential relative to vacuum in hartrees, obtained from the JDFT calculation to a potential vs SHE, we multiplied μ by –27.2116 to get the potential relative to E_{Vac}, and used the relationships E_{SHE} = –4.44 V vs E_{Vac} to obtain the following conversion:

$$E \text{ vs } E_{\mathrm{SHE}} = \mu \times -27.2116 - 4.44\text{ V}. \quad (3)$$

3. Conversion of Electrochemical Potential Values

The relationship E_{SHE} = –0.4 V vs $E(\mathrm{Fc}^{+/0})$ was used to convert the potential obtained from our electrochemical measurement of the open-circuit voltage of the dropcast *ce*MoS_2 electrode, as well as the potentials referenced in previously reported experimental reductant-activated work to a potential relative to SHE, to obtain the following table. The starred values were obtained from previous work.[11]

Reductant (A^-) **(50:1 red:ox)**	**Potential vs $E(\mathrm{Fc}^{+/0})$ (V)**	**Potential vs E_{SHE} (V)**
Open circuit voltage	–0.1	0.3
Nickelocene	–0.52*	–0.12
Octamethylnickelocene	–1.05*	–0.65
Cobaltocene	–1.26*	–0.86

4. Calculations Using the Boltzmann Distribution and Eyring Equation

The Boltzmann distribution for the relative probabilities of two states to be populated based on their free energies is given by:

$$p_i/p_j = exp(-(E_i - E_j)/k_B T) \qquad (4)$$

where p_i is the probability of the system being in state *i*, $\underline{E}_i$ is the energy of state *i*, k_B is the Boltzmann constant, T is the temperature. In this work, we used the energy of the state in eV, $k_B = 8.617E\text{-}5$ eV/K, and $T = 298$ K.

The Eyring equation used to obtain the rate constant of a reaction based on the barrier height is given by:

$$k = (k_B T/h)exp(-\Delta G^{\ddagger}/RT) \qquad (5)$$

where k is the reaction rate constant, k_B is the Boltzmann constant, T is the temperature, h is Planck’s constant, and R is the gas constant. We used the barrier height $\Delta G^{\ddagger}$ values converted to J/mol, $k_B = 1.38E\text{-}23$ J/K, $T = 298$ K, $h = 6.63E\text{-}34$ J·s, and $R = 8.31$ J/(K·mol).

Table A.1 List of free energies and electrochemical potentials for methyl-functionalized MoS_2 structures calculated using jDFTx with CANDLE solvation following optimization using VASP. Sulfur numbers refer to positions functionalized with propyl groups – see Figure 2.5 in main manuscript for numbering overlaid on unit cell. S1–S4 and S9–S12 are high-S, and S5–S8 and S13–S16 are low-S.

Methyl-functionalized Positions	Excess Charge $(\Delta n = n - n_0)$	Free Energy (eV)	Potential (V vs SHE)
S6	2	–39015.62194	–0.1451678652
S7	2	–39015.56757	–0.1581176480
S10	2	–39015.07457	–0.1110112934
S11	2	–39015.07597	–0.1124483108
S7–S1	2	–39219.03720	–0.2158277643
S7–S2	2	–39218.71193	–0.2303384589
S7–S3	2	–39218.57902	–0.2639103078
S7–S4	2	–39218.81809	–0.2001626449
S7–S5	2	–39219.31858	–0.2041571445
S7–S6	2	–39218.93827	–0.2066235223
S7–S8	2	–39218.90332	–0.2173222254
S7–S9	2	–39218.74437	–0.2156520590
S7–S10	2	–39218.56138	–0.2547164061
S7–S11	2	–39219.04605	–0.1037662594
S7–S12	2	–39218.71646	–0.2264322881
S7–S13	2	–39219.08074	–0.2129471988
S7–S14	2	–39219.37704	–0.2148767189
S7–S15	2	–39219.04942	–0.2322386177
S7–S16	2	–39219.28967	–0.2405164408
S7–S14–S1	2	–39422.73083	–0.3342205923
S7–S14–S2	2	–39422.37121	–0.3650879075
S7–S14–S3	2	–39422.29908	–0.3614640026
S7–S14–S4	2	–39422.77784	–0.2822863285
S7–S14–S5	2	–39423.14055	–0.2431903887
S7–S14–S6	2	–39422.63582	–0.3340990653
S7–S14–S8	2	–39422.60484	–0.3299136219
S7–S14–S9	2	–39422.27783	–0.3679436560
S7–S14–S10	2	–39422.30825	–0.3421299431
S7–S14–S11	2	–39423.27163	–0.1683163107
S7–S14–S12	2	–39422.55564	–0.2877080493
S7–S14–S13	2	–39422.66948	–0.3428003009
S7–S14–S15	2	–39422.56295	–0.3789889261
S7–S14–S16	2	–39423.14198	–0.2433804617
S5–S7–S14–S1	2	–39626.37219	–0.4572531613
S5–S7–S14–S2	2	–39626.38574	–0.4505781286
S5–S7–S14–S3	2	–39626.28589	–0.4394758230
S5–S7–S14–S4	2	–39626.35928	–0.4414186768
S5–S7–S14–S6	2	–39626.22129	–0.4670748345
S5–S7–S14–S8	2	–39626.30293	–0.4385793640
S5–S7–S14–S9	2	–39625.96078	–0.4492161336

S5–S7–S14–S10	2	–39625.99037	–0.4516703478
S5–S7–S14–S11	2	–39626.07737	–0.4442290364
S5–S7–S14–S12	2	–39626.05340	–0.4507323367
S5–S7–S14–S13	2	–39626.34658	–0.4214947515
S5–S7–S14–S15	2	–39626.32287	–0.4376117195
S5–S7–S14–S16	2	–39626.91271	–0.2602234897
S5–S7–S14–S16–S1	4.2	–39837.78754	–1.438823928
S5–S7–S14–S16–S2	4.2	–39837.75893	–1.418702365
S5–S7–S14–S16–S3	4.2	–39837.76080	–1.419020986
S5–S7–S14–S16–S4	4.2	–39837.59129	–1.404813374
S5–S7–S14–S16–S6	4.2	–39837.77007	–1.470188481
S5–S7–S14–S16–S8	4.2	–39837.77159	–1.470006027
S5–S7–S14–S16–S9	4.2	–39837.46449	–1.463542864
S5–S7–S14–S16–S10	4.2	–39837.46278	–1.463826218
S5–S7–S14–S16–S11	4.2	–39837.46483	–1.464397336
S5–S7–S14–S16–S12	4.2	–39837.46251	–1.464285441
S5–S7–S14–S16–S13	4.2	–39837.76509	–1.470329927
S5–S7–S14–S16–S15	4.2	–39837.76305	–1.470693828
S5–S7–S13–S14–S16–S1	4.2	–40040.18582	–1.416895025
S5–S7–S13–S14–S16–S2	4.2	–40040.03326	–1.396416582
S5–S7–S13–S14–S16–S3	4.2	–40040.35048	–1.529160671
S5–S7–S13–S14–S16–S4	4.2	–40040.46668	–1.394890855
S5–S7–S13–S14–S16–S6	4.2	–40040.36025	–1.563442525
S5–S7–S13–S14–S16–S8	4.2	–40040.35948	–1.565256723
S5–S7–S13–S14–S16–S9	4.2	–40039.94323	–1.548095863
S5–S7–S13–S14–S16–S10	4.2	–40040.07683	–1.570291821
S5–S7–S13–S14–S16–S11	4.2	–40040.01706	–1.576574190
S5–S7–S13–S14–S16–S12	4.2	–40040.07341	–1.565660815
S5–S7–S13–S14–S16–S15	4.2	–40040.36494	–1.570038726

Table A.2 List of free energies and electrochemical potentials for propyl-functionalized MoS_2 structures calculated using jDFTx with CANDLE solvation following optimization using VASP. Sulfur numbers refer to positions functionalized with propyl groups – see Figure 2.5 in main manuscript for numbering overlaid on unit cell. S1–S4 and S9–S12 are high-S, and S5–S8 and S13–S16 are low-S.

Propyl-functionalized Positions	Excess Charge ($\Delta n = \Delta n - n_0$)	Free Energy (eV)	Potential (V vs SHE)
S6	1.5	–39388.79865	–0.02410696711
S7	1.5	–39388.86435	0.001618770685
S10	1.5	–39388.44943	–0.008178384932
S11	1.5	–39388.40469	–0.007362499530
S7–S1	1.5	–39967.79949	–0.1067574129
S7–S2	1.5	–39967.59688	–0.1796247442
S7–S3	1.5	–39967.37173	–0.1499892437
S7–S4	1.5	–39967.62871	–0.09478912532
S7–S5	1.5	–39968.00263	–0.07991199937
S7–S6	1.5	–39967.72919	–0.07052203813
S7–S8	1.5	–39967.72022	–0.09868794894
S7–S9	1.5	–39967.54099	–0.1252863355
S7–S10	1.5	–39967.46523	–0.1354528342
S7–S11	1.5	–39967.18064	–0.1214119751
S7–S12	1.5	–39967.57250	–0.09686166962
S7–S13	1.5	–39968.12635	–0.0880166751
S7–S14	1.5	–39968.02122	–0.1263387714
S7–S15	1.5	–39967.82536	–0.1557426739
S7–S16	1.5	–39967.98513	–0.1299585945
S7–S13–S1	1.5	–40547.18107	–0.05973892461
S7–S13–S2	1.5	–40546.87846	–0.2114407102
S7–S13–S3	1.5	–40547.60282	0.009880675042
S7–S13–S4	1.5	–40546.75350	–0.2103362458
S7–S13–S5	1.5	–40547.53284	–0.05015902641
S7–S13–S6	1.5	–40547.04140	–0.1850752277
S7–S13–S8	1.5	–40547.03435	–0.1684045035
S7–S13–S9	1.5	–40547.59601	0.009254644973
S7–S13–S10	1.5	–40546.75434	–0.2098032794
S7–S13–S11	1.5	–40547.02616	–0.1311133459
S7–S13–S12	1.5	–40546.87749	–0.2122160503
S7–S13–S14	1.5	–40547.03539	–0.1675663318
S7–S13–S15	1.5	–40547.53636	–0.04753506624
S7–S13–S16	1.5	–40547.04250	–0.1853094107
S5–S7–S13–S1	1.5	–41126.68208	–0.1677352887
S5–S7–S13–S2	1.5	–41126.98848	–0.1700037293
S5–S7–S13–S3	1.5	–41127.07137	–0.1746474976
S5–S7–S13–S4	1.5	–41126.95469	–0.1713118997
S5–S7–S13–S6	1.5	–41126.74362	–0.1472847916
S5–S7–S13–S8	1.5	–41126.73089	–0.1449886768
S5–S7–S13–S9	1.5	–41126.75362	–0.1497482578
S5–S7–S13–S10	1.5	–41126.71972	–0.1507592231

S5–S7–S13–S11	1.5	–41127.03528	–0.1693951963
S5–S7–S13–S12	1.5	–41126.66282	–0.1589866776
S5–S7–S13–S14	1.5	–41126.80911	–0.1772509675
S5–S7–S13–S15	1.5	–41126.92102	–0.1639144807
S5–S7–S13–S16	1.5	–41126.95990	–0.1685755284

Code for Coverage Simulations

Python v. 3.8.5 was used to simulate the random addition of surface functional groups within a given set of constraints. For each model of coverage distribution, N = 2000 simulations were performed of random surface functionalization on 100×100 grids. Half of the positions represent low-S and half represent high-S sulfurs, for a total of 5000 MoS_2 units. Each position has 6 neighbors, as shown in Figure 2.22.

Section 1 is the "0-neighbor max low-S" model, which restricts functionalization to low-S positions and does not allow any functional groups to have nearest neighbors; Section 2 is the "global 1-neighbor max low-S" model, which restricts functionalization to low-S positions and allows a maximum of 1 neighbor for any functionalized position after each step; Section 3 is the "local 1-neighbor max low-S" model, which restricts functionalization to low-S positions and allows a maximum of 1 neighbor next to the position being functionalized; Section 4 is the "local 1-neighbor max" model, which allows a maximum of 1 neighbor next to the position being functionalized whether it is low- or high-S; and Section 5 is the "2-stage local 1-neighbor max" model, which functionalizes the surface first according to the "0-neighbor max low-S" constraints, then according to the "local 1-neighbor max" constraints.

The corresponding coverage per MoS_2 from the simulations below can be calculated by taking the fraction of functionalized positions out of the total (number of functionalized positions divided by the total number of positions) multiplied by 2 to express the fractional coverage per MoS_2 to follow convention with previous studies:

Model coverage per MoS_2 = 2 × Number of Functionalized Positions / Total Number of Positions

1. Coverage distribution model for low-S with no neighbors ("0-neighbor max low-S")

The pseudocode and code to model the coverage distribution under the constraints that (1) low-S sulfurs can be functionalized with a maximum of 0 neighbors and (2) no high-S sulfurs can be functionalized, is given below. The pseudocode is:

1. Initialize a grid of 0's (i.e., not functionalized) with length SHEET_SIZE that is divisible by 2. Even-indexed columns are high-S and odd-indexed columns are low-S. Create a set of positions that correspond to low-S sulfur which is the set of odd numbers between 0 and (SHEET_SIZE – 1)^2.

2. Randomly select a number from this set of odd positions if it is not empty and convert it to the (row, column) location in the grid.

3. Check the value in of the corresponding position in the grid. If it is 0 (i.e., not functionalized), functionalized it (i.e., change it to 1). Then, remove this position and the position above and below it from the set of positions available (all other adjacent positions are either not neighbors or are high-S).

4. Repeat steps 2–3 until the set of available positions is empty.

The Python code written in Jupyter Notebook used to obtain the coverage distribution is provided below.

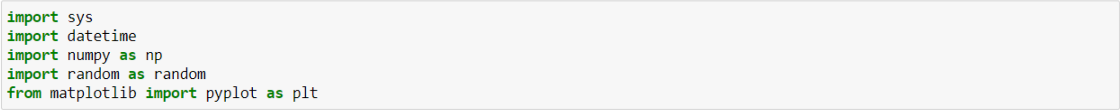

```python
import sys
import datetime
import numpy as np
import random as random
from matplotlib import pyplot as plt
```

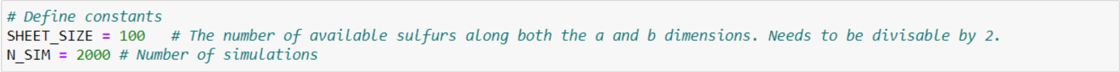

```python
# Define constants
SHEET_SIZE = 100   # The number of available sulfurs along both the a and b dimensions. Needs to be divisable by 2.
N_SIM = 2000 # Number of simulations
```

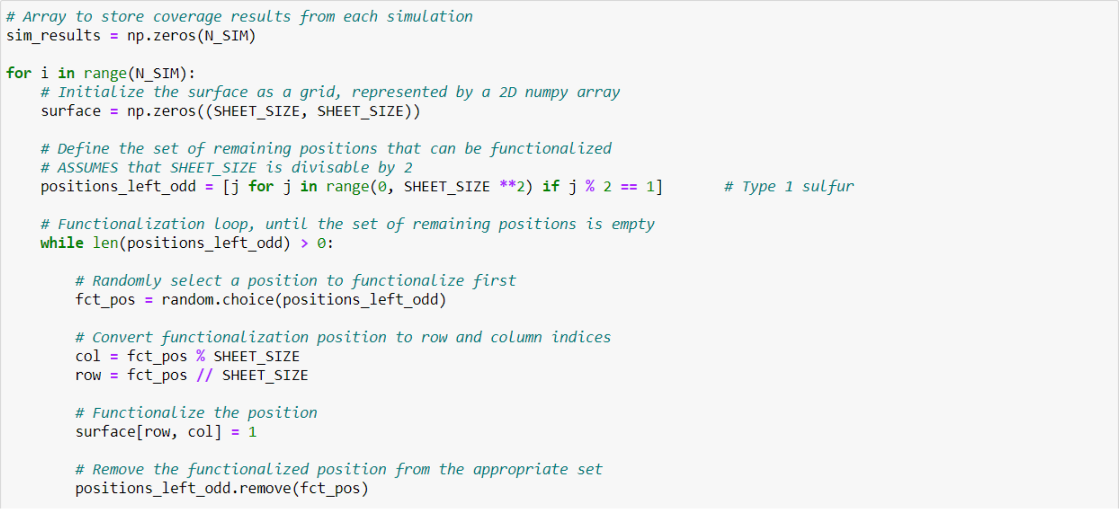

```python
# Array to store coverage results from each simulation
sim_results = np.zeros(N_SIM)

for i in range(N_SIM):
    # Initialize the surface as a grid, represented by a 2D numpy array
    surface = np.zeros((SHEET_SIZE, SHEET_SIZE))

    # Define the set of remaining positions that can be functionalized
    # ASSUMES that SHEET_SIZE is divisable by 2
    positions_left_odd = [j for j in range(0, SHEET_SIZE **2) if j % 2 == 1]        # Type 1 sulfur

    # Functionalization loop, until the set of remaining positions is empty
    while len(positions_left_odd) > 0:

        # Randomly select a position to functionalize first
        fct_pos = random.choice(positions_left_odd)

        # Convert functionalization position to row and column indices
        col = fct_pos % SHEET_SIZE
        row = fct_pos // SHEET_SIZE

        # Functionalize the position
        surface[row, col] = 1

        # Remove the functionalized position from the appropriate set
        positions_left_odd.remove(fct_pos)
```

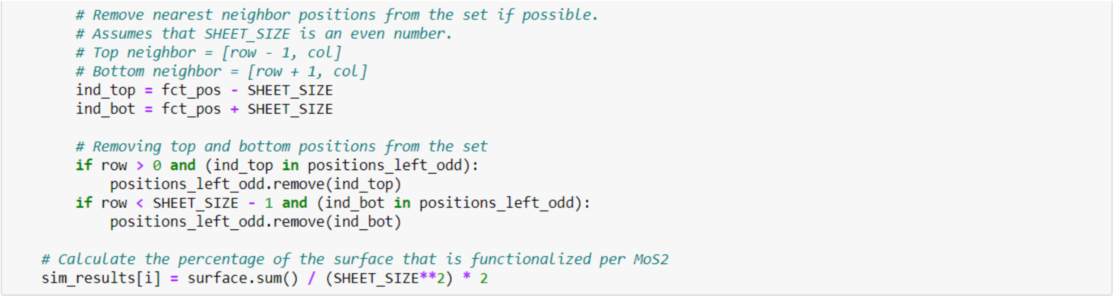

```
        # Remove nearest neighbor positions from the set if possible.
        # Assumes that SHEET_SIZE is an even number.
        # Top neighbor = [row - 1, col]
        # Bottom neighbor = [row + 1, col]
        ind_top = fct_pos - SHEET_SIZE
        ind_bot = fct_pos + SHEET_SIZE

        # Removing top and bottom positions from the set
        if row > 0 and (ind_top in positions_left_odd):
            positions_left_odd.remove(ind_top)
        if row < SHEET_SIZE - 1 and (ind_bot in positions_left_odd):
            positions_left_odd.remove(ind_bot)

    # Calculate the percentage of the surface that is functionalized per MoS2
    sim_results[i] = surface.sum() / (SHEET_SIZE**2) * 2
```

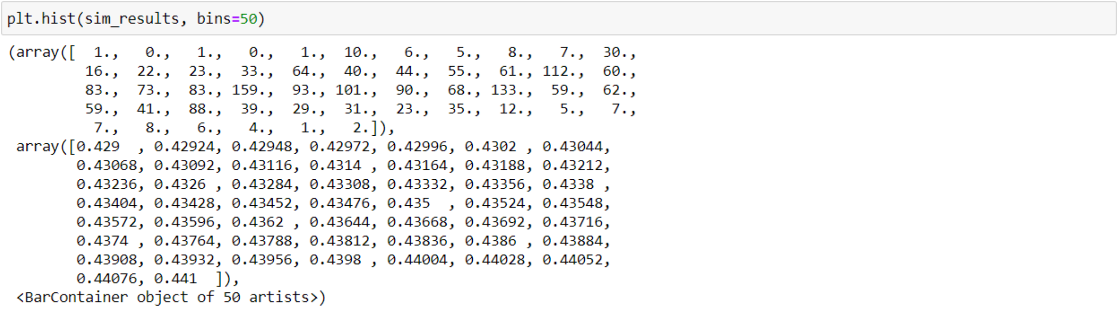

```
plt.hist(sim_results, bins=50)
```

```
(array([  1.,   0.,   1.,   0.,   1.,  10.,   6.,   5.,   8.,   7.,  30.,
         16.,  22.,  23.,  33.,  64.,  40.,  44.,  55.,  61., 112.,  60.,
         83.,  73.,  83., 159.,  93., 101.,  90.,  68., 133.,  59.,  62.,
         59.,  41.,  88.,  39.,  29.,  31.,  23.,  35.,  12.,   5.,   7.,
          7.,   8.,   6.,   4.,   1.,   2.]),
 array([0.429  , 0.42924, 0.42948, 0.42972, 0.42996, 0.4302 , 0.43044,
        0.43068, 0.43092, 0.43116, 0.4314 , 0.43164, 0.43188, 0.43212,
        0.43236, 0.4326 , 0.43284, 0.43308, 0.43332, 0.43356, 0.4338 ,
        0.43404, 0.43428, 0.43452, 0.43476, 0.435  , 0.43524, 0.43548,
        0.43572, 0.43596, 0.4362 , 0.43644, 0.43668, 0.43692, 0.43716,
        0.4374 , 0.43764, 0.43788, 0.43812, 0.43836, 0.4386 , 0.43884,
        0.43908, 0.43932, 0.43956, 0.4398 , 0.44004, 0.44028, 0.44052,
        0.44076, 0.441  ]),
 <BarContainer object of 50 artists>)
```

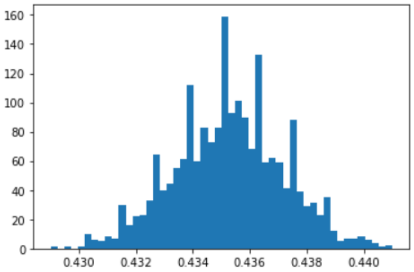

Example surface after a simulation of a 12 × 12 grid:

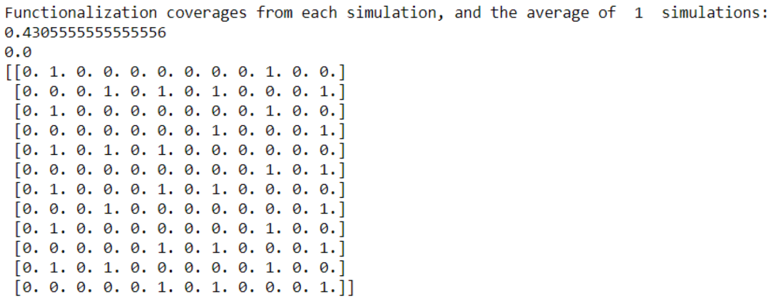

```
Functionalization coverages from each simulation, and the average of  1  simulations:
0.43055555555555556
0.0
[[0. 1. 0. 0. 0. 0. 0. 0. 0. 1. 0. 0.]
 [0. 0. 0. 1. 0. 1. 0. 1. 0. 0. 0. 1.]
 [0. 1. 0. 0. 0. 0. 0. 0. 0. 1. 0. 0.]
 [0. 0. 0. 0. 0. 0. 0. 1. 0. 0. 0. 1.]
 [0. 1. 0. 1. 0. 1. 0. 0. 0. 0. 0. 0.]
 [0. 0. 0. 0. 0. 0. 0. 0. 0. 1. 0. 1.]
 [0. 1. 0. 0. 0. 1. 0. 1. 0. 0. 0. 0.]
 [0. 0. 0. 1. 0. 0. 0. 0. 0. 0. 0. 1.]
 [0. 1. 0. 0. 0. 0. 0. 0. 0. 1. 0. 0.]
 [0. 0. 0. 0. 0. 1. 0. 1. 0. 0. 0. 1.]
 [0. 1. 0. 1. 0. 0. 0. 0. 0. 1. 0. 0.]
 [0. 0. 0. 0. 0. 1. 0. 1. 0. 0. 0. 1.]]
```

2. Coverage distribution model allowing a maximum of two functional groups in a row on low-S (“global 1-neighbor max low-S”)

The pseudocode and code to model the coverage distribution under the constraints that (1) low-S sulfurs can be functionalized if the result is no more than two adjacent functional groups and (2) no high-S sulfurs can be functionalized, is given below. The pseudocode is:

1. Initialize a grid of 0’s with length SHEET_SIZE that is divisible by 2. Even-indexed columns are high-S and odd-indexed columns are low-S. Create a set of positions that correspond to low-S sulfur which is the set of odd numbers between 0 and (SHEET_SIZE – 1)^2.

2. Randomly select a number from this set of odd positions if it is not empty and convert it to the (row, column) location in the grid. Functionalize this position. (i.e., set the value in the grid to 1).

3. If functionalization yields more than 2 functional groups in a row, remove this functional group: check every window within which this position is contained for more than 2 functional groups in a row. If there is more than 2, stop checking and remove this functional group (i.e., set the value to 0).

4. Remove this position from the set of positions available to be functionalized.

5. Repeat steps 2–4 until the set of available positions is empty.

The Python code written in Jupyter Notebook used to obtain the coverage distribution is provided below.

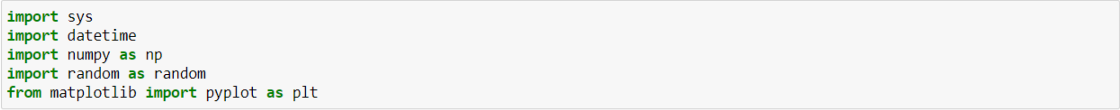

```
import sys
import datetime
import numpy as np
import random as random
from matplotlib import pyplot as plt
```

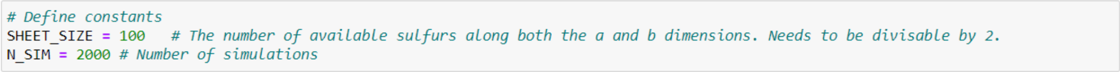

```
# Define constants
SHEET_SIZE = 100   # The number of available sulfurs along both the a and b dimensions. Needs to be divisable by 2.
N_SIM = 2000 # Number of simulations
```

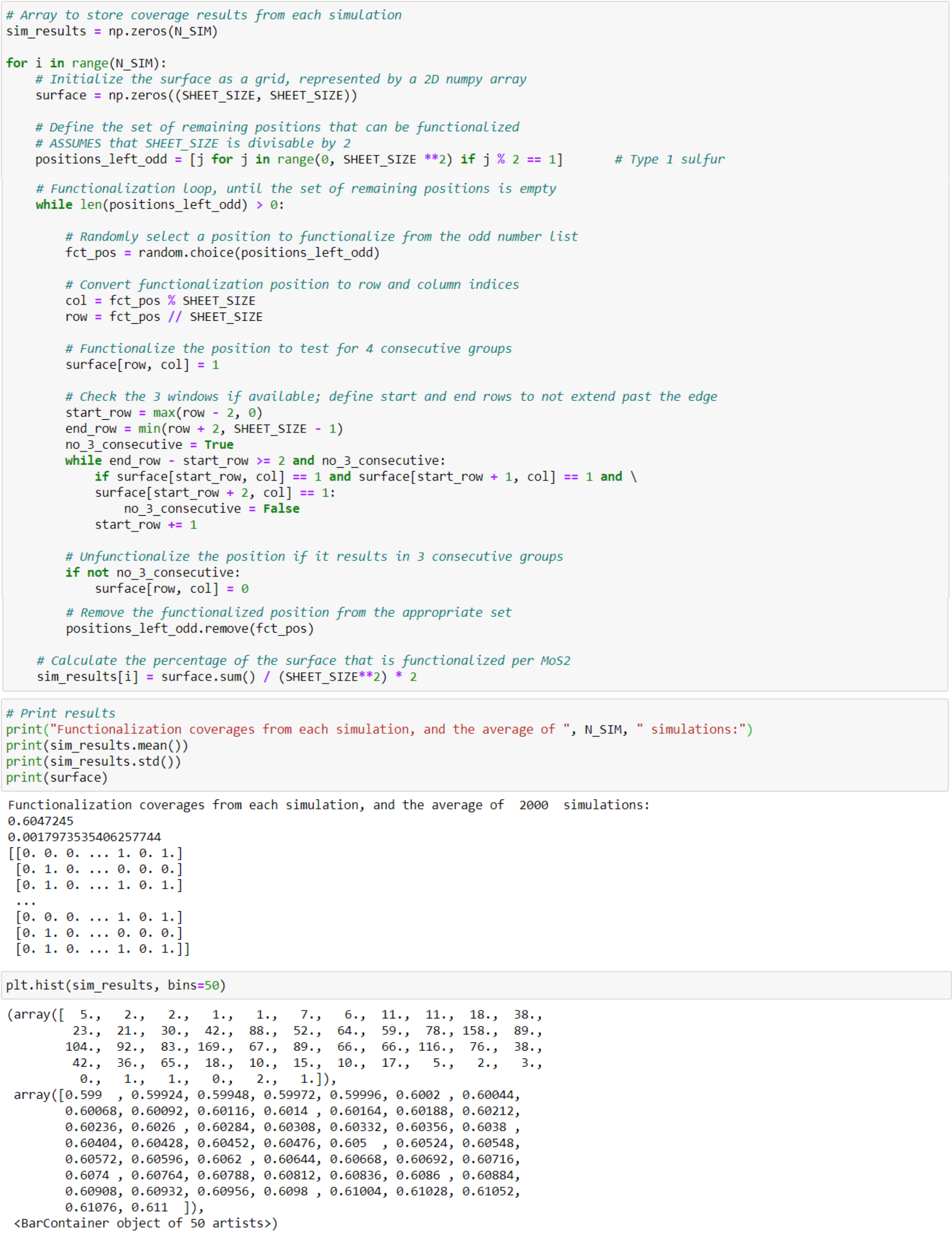

```
# Array to store coverage results from each simulation
sim_results = np.zeros(N_SIM)

for i in range(N_SIM):
    # Initialize the surface as a grid, represented by a 2D numpy array
    surface = np.zeros((SHEET_SIZE, SHEET_SIZE))

    # Define the set of remaining positions that can be functionalized
    # ASSUMES that SHEET_SIZE is divisable by 2
    positions_left_odd = [j for j in range(0, SHEET_SIZE **2) if j % 2 == 1]       # Type 1 sulfur
    # Functionalization loop, until the set of remaining positions is empty
    while len(positions_left_odd) > 0:

        # Randomly select a position to functionalize from the odd number list
        fct_pos = random.choice(positions_left_odd)

        # Convert functionalization position to row and column indices
        col = fct_pos % SHEET_SIZE
        row = fct_pos // SHEET_SIZE

        # Functionalize the position to test for 4 consecutive groups
        surface[row, col] = 1

        # Check the 3 windows if available; define start and end rows to not extend past the edge
        start_row = max(row - 2, 0)
        end_row = min(row + 2, SHEET_SIZE - 1)
        no_3_consecutive = True
        while end_row - start_row >= 2 and no_3_consecutive:
            if surface[start_row, col] == 1 and surface[start_row + 1, col] == 1 and \
            surface[start_row + 2, col] == 1:
                no_3_consecutive = False
            start_row += 1

        # Unfunctionalize the position if it results in 3 consecutive groups
        if not no_3_consecutive:
            surface[row, col] = 0
        # Remove the functionalized position from the appropriate set
        positions_left_odd.remove(fct_pos)

    # Calculate the percentage of the surface that is functionalized per MoS2
    sim_results[i] = surface.sum() / (SHEET_SIZE**2) * 2
```

```
# Print results
print("Functionalization coverages from each simulation, and the average of ", N_SIM, " simulations:")
print(sim_results.mean())
print(sim_results.std())
print(surface)
```

```
Functionalization coverages from each simulation, and the average of  2000  simulations:
0.6047245
0.0017973535406257744
[[0. 0. 0. ... 1. 0. 1.]
 [0. 1. 0. ... 0. 0. 0.]
 [0. 1. 0. ... 1. 0. 1.]
 ...
 [0. 0. 0. ... 1. 0. 1.]
 [0. 1. 0. ... 0. 0. 0.]
 [0. 1. 0. ... 1. 0. 1.]]
```

```
plt.hist(sim_results, bins=50)
```

```
(array([  5.,   2.,   2.,   1.,   1.,   7.,   6.,  11.,  11.,  18.,  38.,
         23.,  21.,  30.,  42.,  88.,  52.,  64.,  59.,  78., 158.,  89.,
        104.,  92.,  83., 169.,  67.,  89.,  66.,  66., 116.,  76.,  38.,
         42.,  36.,  65.,  18.,  10.,  15.,  10.,  17.,   5.,   2.,   3.,
          0.,   1.,   1.,   0.,   2.,   1.]),
 array([0.599  , 0.59924, 0.59948, 0.59972, 0.59996, 0.6002 , 0.60044,
        0.60068, 0.60092, 0.60116, 0.6014 , 0.60164, 0.60188, 0.60212,
        0.60236, 0.6026 , 0.60284, 0.60308, 0.60332, 0.60356, 0.6038 ,
        0.60404, 0.60428, 0.60452, 0.60476, 0.605  , 0.60524, 0.60548,
        0.60572, 0.60596, 0.6062 , 0.60644, 0.60668, 0.60692, 0.60716,
        0.6074 , 0.60764, 0.60788, 0.60812, 0.60836, 0.6086 , 0.60884,
        0.60908, 0.60932, 0.60956, 0.6098 , 0.61004, 0.61028, 0.61052,
        0.61076, 0.611  ]),
 <BarContainer object of 50 artists>)
```

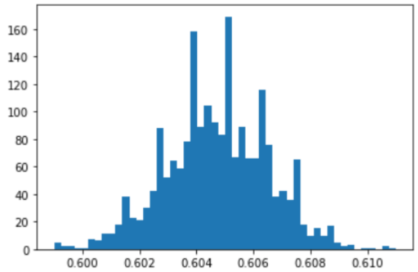

Example surface after a simulation of a 12 × 12 grid:

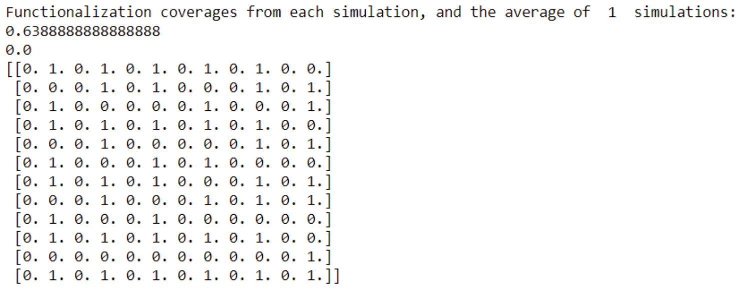

```
Functionalization coverages from each simulation, and the average of  1  simulations:
0.6388888888888888
0.0
[[0. 1. 0. 1. 0. 1. 0. 1. 0. 1. 0. 0.]
 [0. 0. 0. 1. 0. 1. 0. 0. 0. 1. 0. 1.]
 [0. 1. 0. 0. 0. 0. 0. 1. 0. 0. 0. 1.]
 [0. 1. 0. 1. 0. 1. 0. 1. 0. 1. 0. 0.]
 [0. 0. 0. 1. 0. 0. 0. 0. 0. 1. 0. 1.]
 [0. 1. 0. 0. 0. 1. 0. 1. 0. 0. 0. 0.]
 [0. 1. 0. 1. 0. 1. 0. 0. 0. 1. 0. 1.]
 [0. 0. 0. 1. 0. 0. 0. 1. 0. 1. 0. 1.]
 [0. 1. 0. 0. 0. 1. 0. 0. 0. 0. 0. 0.]
 [0. 1. 0. 1. 0. 1. 0. 1. 0. 1. 0. 0.]
 [0. 0. 0. 0. 0. 0. 0. 0. 0. 0. 0. 1.]
 [0. 1. 0. 1. 0. 1. 0. 1. 0. 1. 0. 1.]]
```

3. Coverage distribution model allowing at most one adjacent functional group to functionalization site at each step and only low-S (“local 1-neighbor max low-S”)

The pseudocode and code to model the coverage distribution under the constraints that (1) a low-S sulfur site can be functionalized if there is a maximum of 1 neighbor to the functionalization site and (2) no high-S sulfurs can be functionalized is given below. The pseudocode is:

1. Initialize a grid of 0’s with length SHEET_SIZE that is divisible by 2. Even-indexed columns are high-S and odd-indexed columns are low-S. Create a set of positions that correspond to low-S sulfur which is the set of odd numbers between 0 and (SHEET_SIZE – 1)^2.

2. Randomly select a number from this set of odd positions if it is not empty and convert it to the (row, column) location in the grid.

3. Check the values of the position above and below to see if there is at most one of these positions that is functionalized (i.e., sum of the values in positions above and below is < 2). If this is the case, functionalize this position (change to 1). Remove this position from the set of positions available. (Other positions not above/below are either not neighbors or are not high-S.)

4. Repeat steps 2–3 until the set of available positions is empty.

The Python code written in Jupyter Notebook used to obtain the coverage distribution is provided below.

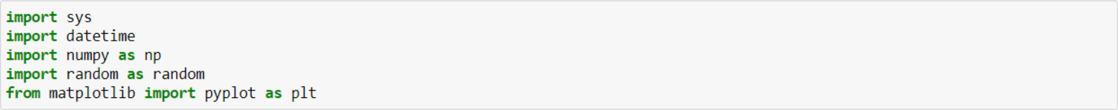

```
import sys
import datetime
import numpy as np
import random as random
from matplotlib import pyplot as plt
```

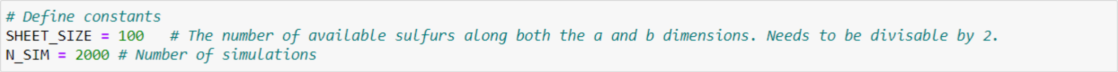

```
# Define constants
SHEET_SIZE = 100   # The number of available sulfurs along both the a and b dimensions. Needs to be divisable by 2.
N_SIM = 2000 # Number of simulations
```

```
# Array to store coverage results from each simulation
sim_results = np.zeros(N_SIM)

for i in range(N_SIM):
    # Initialize the surface as a grid, represented by a 2D numpy array
    surface = np.zeros((SHEET_SIZE, SHEET_SIZE))

    # Define the set of remaining positions that can be functionalized
    # ASSUMES that SHEET_SIZE is divisable by 2
    positions_left_odd = [j for j in range(0, SHEET_SIZE **2) if j % 2 == 1]       # Type 1 sulfur

    # Functionalization loop, until the set of remaining positions is empty
    while len(positions_left_odd) > 0:

        # Randomly select a position to functionalize from the odd number list
        fct_pos = random.choice(positions_left_odd)

        # Convert functionalization position to row and column indices
        col = fct_pos % SHEET_SIZE
        row = fct_pos // SHEET_SIZE
        # Check the number of neighbors this position has, if applicable
        num_neighbors = 0
        if row > 0:
            num_neighbors += surface[row - 1, col]
        if row < SHEET_SIZE - 1:
            num_neighbors += surface[row + 1, col]

        # Functionalize this position if there are less than 2 neighbors
        if num_neighbors < 2:
            surface[row, col] = 1

        # Remove the functionalized position from the appropriate set
        positions_left_odd.remove(fct_pos)

    # Calculate the percentage of the surface that is functionalized per MoS2
    sim_results[i] = surface.sum() / (SHEET_SIZE**2) * 2
```

```
# Print results
print("Functionalization coverages from each simulation, and the average of ", N_SIM, " simulations:")
print(sim_results.mean())
print(sim_results.std())
print(surface)
```

```
Functionalization coverages from each simulation, and the average of  2000  simulations:
0.6733208999999999
0.0030028724898003936
[[0. 1. 0. ... 1. 0. 1.]
 [0. 0. 0. ... 0. 0. 1.]
 [0. 1. 0. ... 1. 0. 1.]
 ...
 [0. 1. 0. ... 1. 0. 1.]
 [0. 0. 0. ... 0. 0. 0.]
 [0. 1. 0. ... 1. 0. 1.]]
```

```
plt.hist(sim_results, bins=50)
```

```
(array([  1.,   1.,   3.,   2.,   0.,   3.,   4.,   8.,   7.,  12.,  18.,
         18.,  42.,  38.,  49.,  55.,  60.,  72., 103.,  92.,  97.,  97.,
        100.,  94., 114., 160., 129.,  76.,  93.,  78.,  73.,  77.,  39.,
         40.,  32.,  16.,  25.,  26.,  12.,  13.,   6.,   4.,   5.,   1.,
          2.,   0.,   2.,   0.,   0.,   1.]),
 array([0.663   , 0.663432, 0.663864, 0.664296, 0.664728, 0.66516 ,
        0.665592, 0.666024, 0.666456, 0.666888, 0.66732 , 0.667752,
        0.668184, 0.668616, 0.669048, 0.66948 , 0.669912, 0.670344,
        0.670776, 0.671208, 0.67164 , 0.672072, 0.672504, 0.672936,
        0.673368, 0.6738  , 0.674232, 0.674664, 0.675096, 0.675528,
        0.67596 , 0.676392, 0.676824, 0.677256, 0.677688, 0.67812 ,
        0.678552, 0.678984, 0.679416, 0.679848, 0.68028 , 0.680712,
        0.681144, 0.681576, 0.682008, 0.68244 , 0.682872, 0.683304,
        0.683736, 0.684168, 0.6846  ]),
 <BarContainer object of 50 artists>)
```

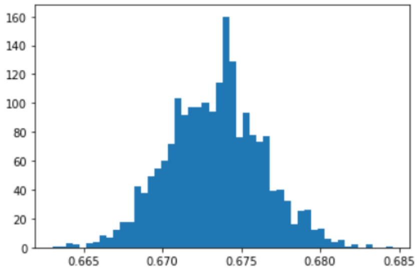

Example surface after a simulation of a 12 × 12 grid:

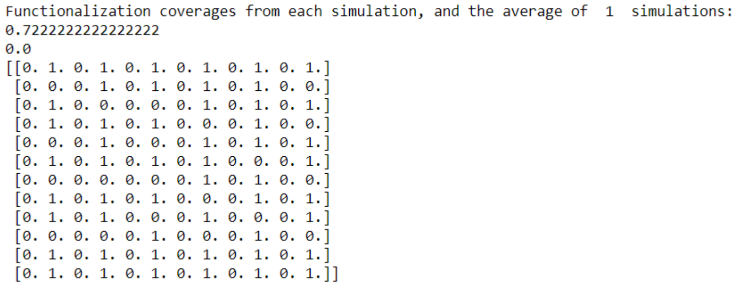

```
Functionalization coverages from each simulation, and the average of  1  simulations:
0.7222222222222222
0.0
[[0. 1. 0. 1. 0. 1. 0. 1. 0. 1. 0. 1.]
 [0. 0. 0. 1. 0. 1. 0. 1. 0. 1. 0. 0.]
 [0. 1. 0. 0. 0. 0. 0. 1. 0. 1. 0. 1.]
 [0. 1. 0. 1. 0. 1. 0. 0. 0. 1. 0. 0.]
 [0. 0. 0. 1. 0. 0. 0. 1. 0. 1. 0. 1.]
 [0. 1. 0. 1. 0. 1. 0. 1. 0. 0. 0. 1.]
 [0. 0. 0. 0. 0. 0. 0. 1. 0. 1. 0. 0.]
 [0. 1. 0. 1. 0. 1. 0. 0. 0. 1. 0. 1.]
 [0. 1. 0. 1. 0. 0. 0. 1. 0. 0. 0. 1.]
 [0. 0. 0. 0. 0. 1. 0. 0. 0. 1. 0. 0.]
 [0. 1. 0. 1. 0. 1. 0. 1. 0. 1. 0. 1.]
 [0. 1. 0. 1. 0. 1. 0. 1. 0. 1. 0. 1.]]
```

4. Coverage distribution model allowing at most one adjacent functional group to functionalization site at each step, on any sulfur (“local 1-neighbor max”)

The pseudocode and code to model the coverage distribution under the constraints that any site can be functionalized if there is a maximum of 1 neighbor to the functionalization site, is given below. The pseudocode is:

1. Initialize a grid of 0’s with length SHEET_SIZE that is divisible by 2. Even-indexed columns are high-S and odd-indexed columns are low-S. Create a set of positions that corresponds to both low- and high-S sulfur which is the set of numbers between 0 and (SHEET_SIZE – 1)^2.

2. Randomly select a number from this set of positions if it is not empty and convert it to the (row, column) location in the grid.

3. Check the values of the neighboring positions to see if there is at most one of these positions that is functionalized (i.e., sum of the values is < 2). In converting the hexagonal MoS_2 surface to a rectangular grid, the even-indexed rows have neighbors to the top, bottom, left, top right, right, and bottom right, and the odd-indexed rows have neighbors to the top, bottom, top left, left, bottom left, and right. If there is at most 1 neighbor in total, functionalize this position (change to 1). Remove this position from the set of positions.

4. Repeat steps 2–3 until the set of positions is empty.

The Python code written in Jupyter Notebook used to obtain the coverage distribution is provided below.

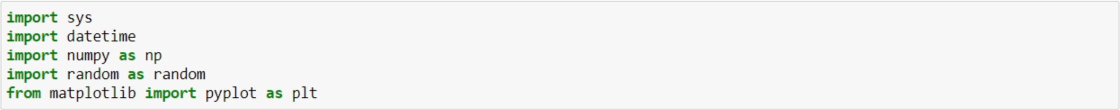

```python
import sys
import datetime
import numpy as np
import random as random
from matplotlib import pyplot as plt
```

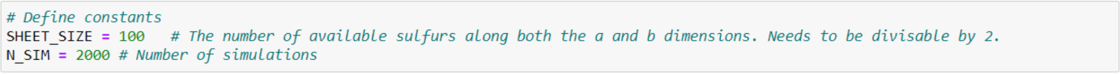

```python
# Define constants
SHEET_SIZE = 100   # The number of available sulfurs along both the a and b dimensions. Needs to be divisable by 2.
N_SIM = 2000 # Number of simulations
```

```
# Constant for number of neighbors
MAX_NEIGHBORS = 1

# Array to store coverage results from each simulation
sim_results = np.zeros(N_SIM)

for i in range(N_SIM):
    # Initialize the surface as a grid, represented by a 2D numpy array
    surface = np.zeros((SHEET_SIZE, SHEET_SIZE))

    # Define the set of remaining positions that can be functionalized
    # ASSUMES that SHEET_SIZE is divisable by 2
    pos_left = [j for j in range(0, SHEET_SIZE **2)]

    # Functionalization loop, until the set of remaining positions is empty
    while len(pos_left) > 0:

        # Randomly select a position to functionalize
        fct_pos = random.choice(pos_left)

        # Convert functionalization position to row and column indices
        col = fct_pos % SHEET_SIZE
        row = fct_pos // SHEET_SIZE

        # Counter for the number of neighbors
        num_neighbors = 0

        # Count the number of nearest neighbors, starting with top, bottom, left, and right
        if row > 0:
            num_neighbors += surface[row - 1, col]     # top neighbor
        if row < SHEET_SIZE - 1:
            num_neighbors += surface[row + 1, col]     # bottom neighbor
        if col > 0:
            num_neighbors += surface[row, col - 1]     # left neighbor
        if col < SHEET_SIZE - 1:
            num_neighbors += surface[row, col + 1]     # right neighbor

        # Even-indexed rows and odd-indexed rows have different patterns of neighbors in addition
        # to the top, bottom, left, and right.
        # Even: neighbors also include top right, bottom right
        # Odd: neighbors also include top left, bottom left
        if row % 2 == 0:
            if row > 0 and col < SHEET_SIZE - 1:
                num_neighbors += surface[row - 1, col + 1]     # top right neighbor
            if row < SHEET_SIZE - 1 and col < SHEET_SIZE - 1:
                num_neighbors += surface[row + 1, col + 1]     # bottom right neighbor
        else:
            if row > 0 and col > 0:
                num_neighbors += surface[row - 1, col - 1]     # top left neighbor
            if row < SHEET_SIZE - 1 and col > 0:
                num_neighbors += surface [row + 1, col - 1]    # bottom left neighbor

        # Functionalize if number of neighbors doesn't exceed maximum (1 neighbor)
        if num_neighbors <= MAX_NEIGHBORS:
            surface[row, col] = 1

        pos_left.remove(fct_pos)

    # Calculate the percentage of the surface that is functionalized per MoS2
    sim_results[i] = surface.sum() / (SHEET_SIZE**2) * 2
```

```
# Print results
print("Functionalization coverages from each simulation, and the average of ", N_SIM, " simulations:")
print(sim_results.mean())
print(sim_results.std())
print(surface)
```

```
Functionalization coverages from each simulation, and the average of  2000  simulations:
0.7533289999999999
0.002853033298088197
[[1. 0. 0. ... 1. 1. 1.]
 [1. 0. 1. ... 0. 0. 0.]
 [0. 1. 0. ... 1. 0. 1.]
 ...
 [1. 1. 0. ... 0. 1. 0.]
 [0. 0. 1. ... 0. 0. 1.]
 [1. 1. 0. ... 0. 1. 1.]]
```

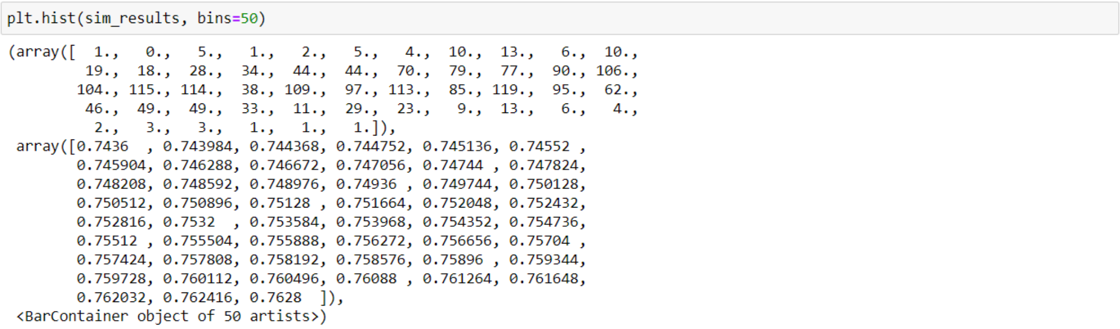

```
plt.hist(sim_results, bins=50)
```

```
(array([  1.,   0.,   5.,   1.,   2.,   5.,   4.,  10.,  13.,   6.,  10.,
         19.,  18.,  28.,  34.,  44.,  44.,  70.,  79.,  77.,  90., 106.,
        104., 115., 114.,  38., 109.,  97., 113.,  85., 119.,  95.,  62.,
         46.,  49.,  49.,  33.,  11.,  29.,  23.,   9.,  13.,   6.,   4.,
          2.,   3.,   3.,   1.,   1.,   1.]),
 array([0.7436  , 0.743984, 0.744368, 0.744752, 0.745136, 0.74552 ,
        0.745904, 0.746288, 0.746672, 0.747056, 0.74744 , 0.747824,
        0.748208, 0.748592, 0.748976, 0.74936 , 0.749744, 0.750128,
        0.750512, 0.750896, 0.75128 , 0.751664, 0.752048, 0.752432,
        0.752816, 0.7532  , 0.753584, 0.753968, 0.754352, 0.754736,
        0.75512 , 0.755504, 0.755888, 0.756272, 0.756656, 0.75704 ,
        0.757424, 0.757808, 0.758192, 0.758576, 0.75896 , 0.759344,
        0.759728, 0.760112, 0.760496, 0.76088 , 0.761264, 0.761648,
        0.762032, 0.762416, 0.7628  ]),
 <BarContainer object of 50 artists>)
```

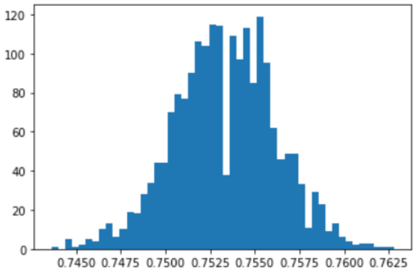

Example surface after a simulation of a 12 × 12 grid:

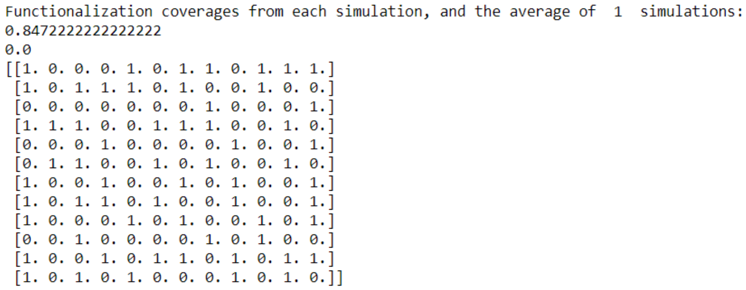

```
Functionalization coverages from each simulation, and the average of  1  simulations:
0.8472222222222222
0.0
[[1. 0. 0. 0. 1. 0. 1. 1. 0. 1. 1. 1.]
 [1. 0. 1. 1. 1. 0. 1. 0. 0. 1. 0. 0.]
 [0. 0. 0. 0. 0. 0. 0. 1. 0. 0. 0. 1.]
 [1. 1. 1. 0. 0. 1. 1. 1. 0. 0. 1. 0.]
 [0. 0. 0. 1. 0. 0. 0. 0. 1. 0. 0. 1.]
 [0. 1. 1. 0. 0. 1. 0. 1. 0. 0. 1. 0.]
 [1. 0. 0. 1. 0. 0. 1. 0. 1. 0. 0. 1.]
 [1. 0. 1. 1. 0. 1. 0. 0. 1. 0. 0. 1.]
 [1. 0. 0. 0. 1. 0. 1. 0. 0. 1. 0. 1.]
 [0. 0. 1. 0. 0. 0. 0. 1. 0. 1. 0. 0.]
 [1. 0. 0. 1. 0. 1. 1. 0. 1. 0. 1. 1.]
 [1. 0. 1. 0. 1. 0. 0. 0. 1. 0. 1. 0.]]
```

5. Coverage distribution model for a 2-stage process, first following “0-neighbor max low-S”, then following “local 1-neighbor max” (“2-stage local 1-neighbor max”)

The pseudocode and code to model the coverage distribution under the constraints that (1) the surface is functionalized first according to the “0-neighbor max low-S” constraints, and (2) the remaining open positions are functionalized according to the “local 1-neighbor max” constraints, is given below. The pseudocode is:

1. Initialize a grid of 0’s with length SHEET_SIZE that is divisible by 2. Even-indexed columns are high-S and odd-indexed columns are low-S. Create 2 sets of positions (a primary and secondary) that correspond to low-S sulfur which is the set of odd numbers between 0 and $(\text{SHEET\_SIZE} - 1)^2$.

2. Randomly select a number from this set of odd positions if it is not empty and convert it to the (row, column) location in the grid.

3. Check the value in of the corresponding position in the grid. If it is 0 (i.e., not functionalized), functionalized it (i.e., change it to 1). Then, remove this position from both the primary and secondary sets, and remove the position above and below it (i.e., the low-S positions) from the primary set of positions.

4. Repeat steps 2–3 until the primary set of available positions is empty.

5. Combine the secondary set with a set of positions representing the high-S positions (even numbers between 0 and $(\text{SHEET\_SIZE} - 1)^2$ to form the set of remaining positions.

6. Randomly select a number from the set of remaining positions if it is not empty and convert it to the (row, column) location in the grid.

7. Check the values of the neighboring positions to see if there is at most one of these positions that is functionalized (i.e., sum of the values is < 2). In converting the hexagonal MoS_2 surface to a rectangular grid, the even-indexed rows have neighbors to the top, bottom, left, top right, right, and bottom right, and the odd-

indexed rows have neighbors to the top, bottom, top left, left, bottom left, and right. If there is at most 1 neighbor in total, functionalize this position (change to 1). Remove this position from the set of remaining positions.

8. Repeat steps 6–7 until the set of remaining positions is empty.

The Python code written in Jupyter Notebook used to obtain the coverage distribution is provided below.

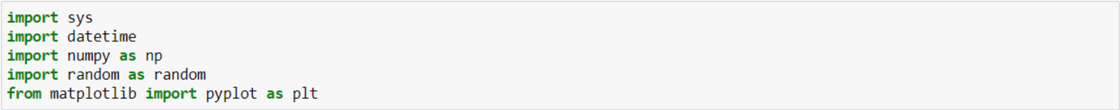

```
import sys
import datetime
import numpy as np
import random as random
from matplotlib import pyplot as plt
```

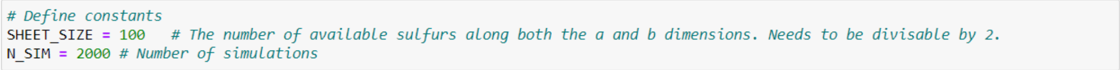

```
# Define constants
SHEET_SIZE = 100   # The number of available sulfurs along both the a and b dimensions. Needs to be divisable by 2.
N_SIM = 2000 # Number of simulations
```

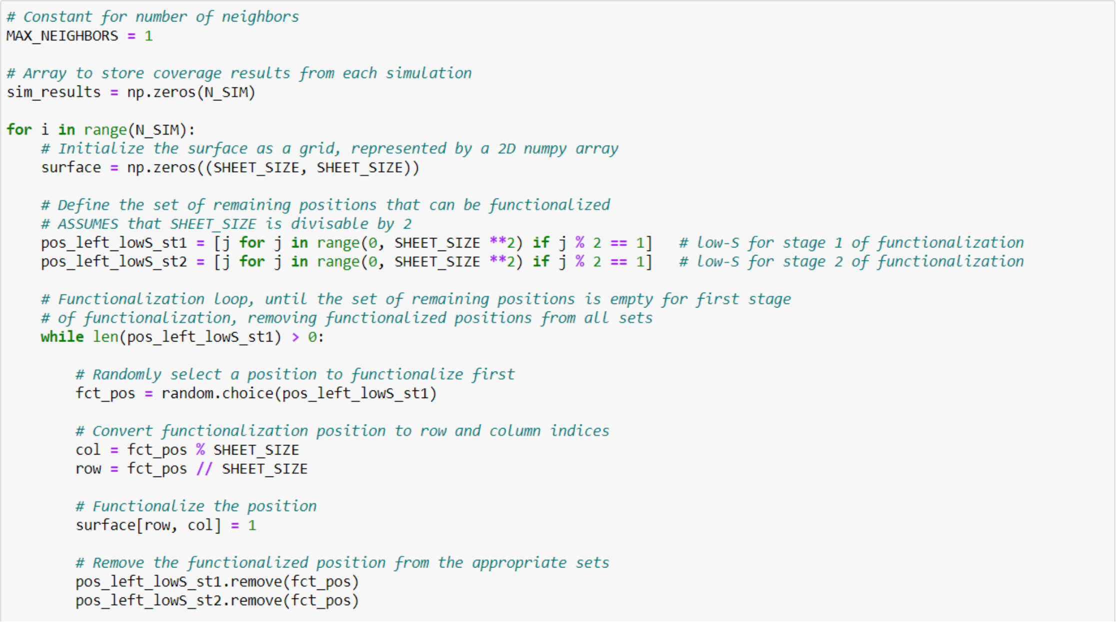

```
# Constant for number of neighbors
MAX_NEIGHBORS = 1

# Array to store coverage results from each simulation
sim_results = np.zeros(N_SIM)

for i in range(N_SIM):
    # Initialize the surface as a grid, represented by a 2D numpy array
    surface = np.zeros((SHEET_SIZE, SHEET_SIZE))

    # Define the set of remaining positions that can be functionalized
    # ASSUMES that SHEET_SIZE is divisable by 2
    pos_left_lowS_st1 = [j for j in range(0, SHEET_SIZE **2) if j % 2 == 1]   # low-S for stage 1 of functionalization
    pos_left_lowS_st2 = [j for j in range(0, SHEET_SIZE **2) if j % 2 == 1]   # low-S for stage 2 of functionalization

    # Functionalization loop, until the set of remaining positions is empty for first stage
    # of functionalization, removing functionalized positions from all sets
    while len(pos_left_lowS_st1) > 0:

        # Randomly select a position to functionalize first
        fct_pos = random.choice(pos_left_lowS_st1)

        # Convert functionalization position to row and column indices
        col = fct_pos % SHEET_SIZE
        row = fct_pos // SHEET_SIZE

        # Functionalize the position
        surface[row, col] = 1

        # Remove the functionalized position from the appropriate sets
        pos_left_lowS_st1.remove(fct_pos)
        pos_left_lowS_st2.remove(fct_pos)
```

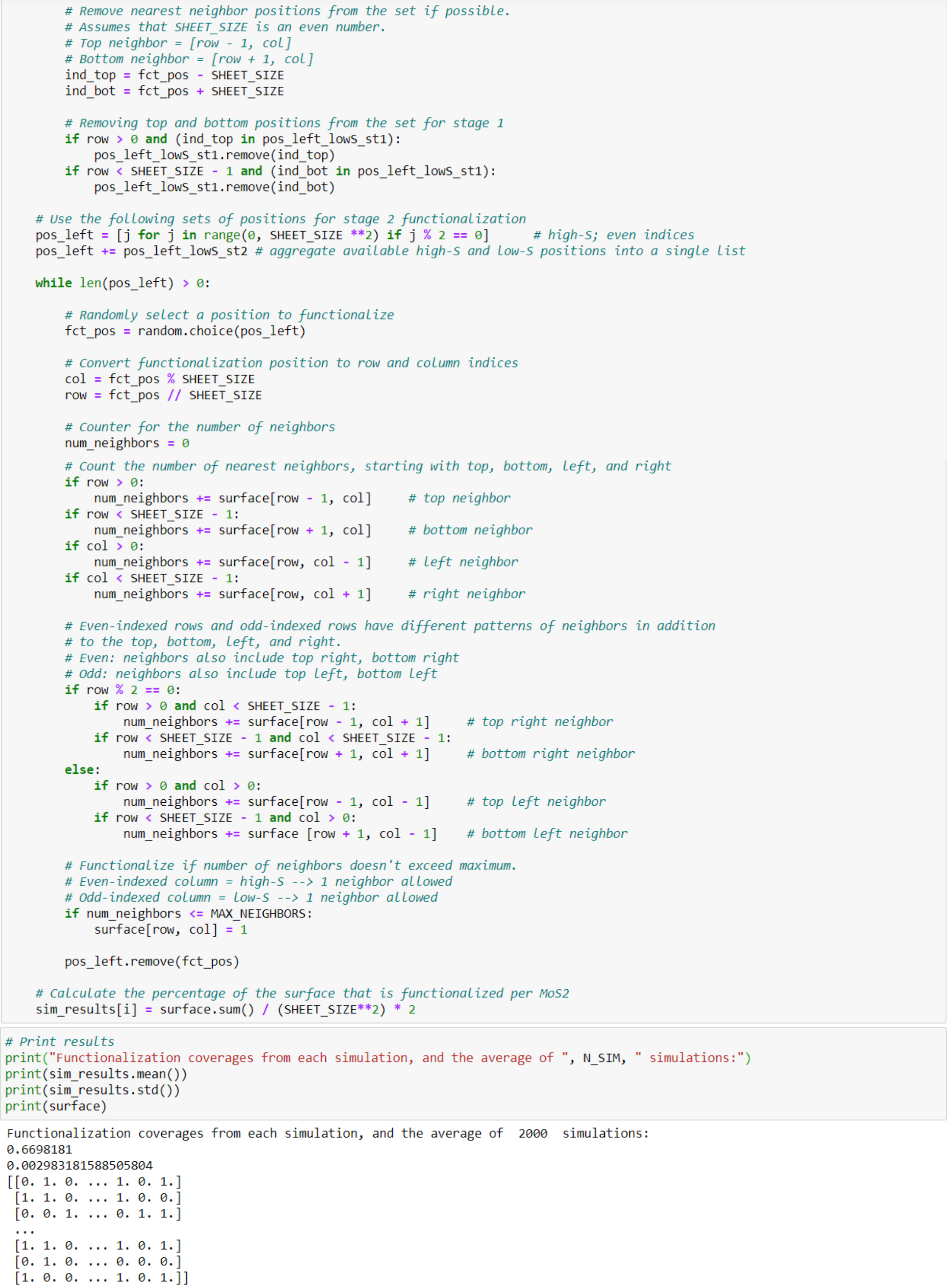

```
        # Remove nearest neighbor positions from the set if possible.
        # Assumes that SHEET_SIZE is an even number.
        # Top neighbor = [row - 1, col]
        # Bottom neighbor = [row + 1, col]
        ind_top = fct_pos - SHEET_SIZE
        ind_bot = fct_pos + SHEET_SIZE

        # Removing top and bottom positions from the set for stage 1
        if row > 0 and (ind_top in pos_left_lowS_st1):
            pos_left_lowS_st1.remove(ind_top)
        if row < SHEET_SIZE - 1 and (ind_bot in pos_left_lowS_st1):
            pos_left_lowS_st1.remove(ind_bot)

    # Use the following sets of positions for stage 2 functionalization
    pos_left = [j for j in range(0, SHEET_SIZE **2) if j % 2 == 0]      # high-S; even indices
    pos_left += pos_left_lowS_st2 # aggregate available high-S and low-S positions into a single list

    while len(pos_left) > 0:

        # Randomly select a position to functionalize
        fct_pos = random.choice(pos_left)

        # Convert functionalization position to row and column indices
        col = fct_pos % SHEET_SIZE
        row = fct_pos // SHEET_SIZE

        # Counter for the number of neighbors
        num_neighbors = 0

        # Count the number of nearest neighbors, starting with top, bottom, left, and right
        if row > 0:
            num_neighbors += surface[row - 1, col]     # top neighbor
        if row < SHEET_SIZE - 1:
            num_neighbors += surface[row + 1, col]     # bottom neighbor
        if col > 0:
            num_neighbors += surface[row, col - 1]     # left neighbor
        if col < SHEET_SIZE - 1:
            num_neighbors += surface[row, col + 1]     # right neighbor

        # Even-indexed rows and odd-indexed rows have different patterns of neighbors in addition
        # to the top, bottom, left, and right.
        # Even: neighbors also include top right, bottom right
        # Odd: neighbors also include top left, bottom left
        if row % 2 == 0:
            if row > 0 and col < SHEET_SIZE - 1:
                num_neighbors += surface[row - 1, col + 1]     # top right neighbor
            if row < SHEET_SIZE - 1 and col < SHEET_SIZE - 1:
                num_neighbors += surface[row + 1, col + 1]     # bottom right neighbor
        else:
            if row > 0 and col > 0:
                num_neighbors += surface[row - 1, col - 1]     # top left neighbor
            if row < SHEET_SIZE - 1 and col > 0:
                num_neighbors += surface [row + 1, col - 1]    # bottom left neighbor

        # Functionalize if number of neighbors doesn't exceed maximum.
        # Even-indexed column = high-S --> 1 neighbor allowed
        # Odd-indexed column = low-S --> 1 neighbor allowed
        if num_neighbors <= MAX_NEIGHBORS:
            surface[row, col] = 1

        pos_left.remove(fct_pos)

    # Calculate the percentage of the surface that is functionalized per MoS2
    sim_results[i] = surface.sum() / (SHEET_SIZE**2) * 2
```

```
# Print results
print("Functionalization coverages from each simulation, and the average of ", N_SIM, " simulations:")
print(sim_results.mean())
print(sim_results.std())
print(surface)
```

```
Functionalization coverages from each simulation, and the average of  2000  simulations:
0.6698181
0.002983181588505804
[[0. 1. 0. ... 1. 0. 1.]
 [1. 1. 0. ... 1. 0. 0.]
 [0. 0. 1. ... 0. 1. 1.]
 ...
 [1. 1. 0. ... 1. 0. 1.]
 [0. 1. 0. ... 0. 0. 0.]
 [1. 0. 0. ... 1. 0. 1.]]
```

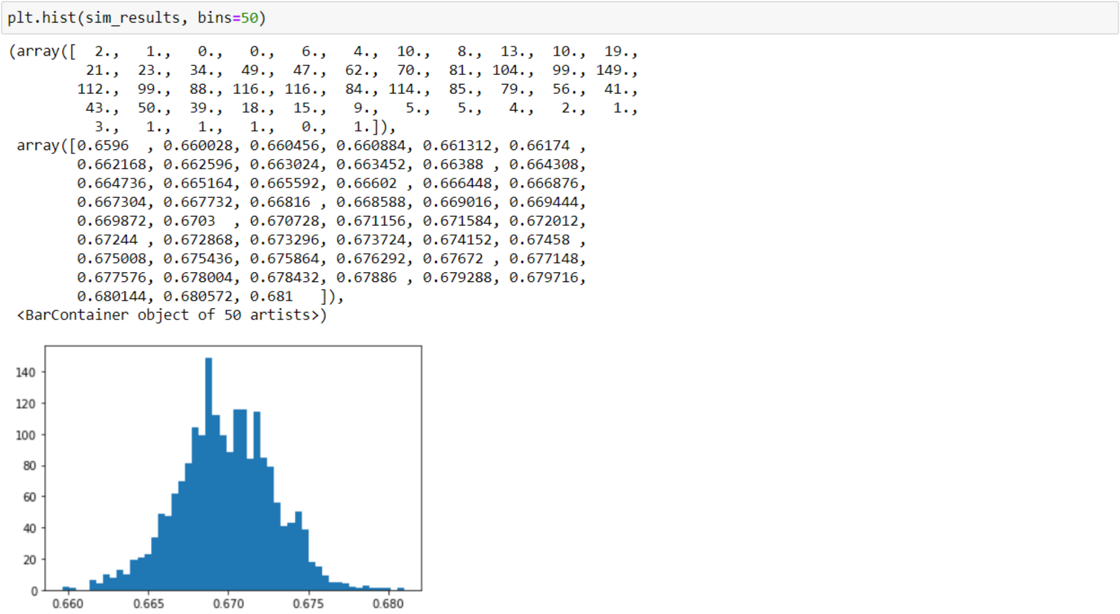

```
plt.hist(sim_results, bins=50)
```

```
(array([  2.,   1.,   0.,   0.,   6.,   4.,  10.,   8.,  13.,  10.,  19.,
         21.,  23.,  34.,  49.,  47.,  62.,  70.,  81., 104.,  99., 149.,
        112.,  99.,  88., 116., 116.,  84., 114.,  85.,  79.,  56.,  41.,
         43.,  50.,  39.,  18.,  15.,   9.,   5.,   5.,   4.,   2.,   1.,
          3.,   1.,   1.,   1.,   0.,   1.]),
 array([0.6596  , 0.660028, 0.660456, 0.660884, 0.661312, 0.66174 ,
        0.662168, 0.662596, 0.663024, 0.663452, 0.66388 , 0.664308,
        0.664736, 0.665164, 0.665592, 0.66602 , 0.666448, 0.666876,
        0.667304, 0.667732, 0.66816 , 0.668588, 0.669016, 0.669444,
        0.669872, 0.6703  , 0.670728, 0.671156, 0.671584, 0.672012,
        0.67244 , 0.672868, 0.673296, 0.673724, 0.674152, 0.67458 ,
        0.675008, 0.675436, 0.675864, 0.676292, 0.67672 , 0.677148,
        0.677576, 0.678004, 0.678432, 0.67886 , 0.679288, 0.679716,
        0.680144, 0.680572, 0.681   ]),
 <BarContainer object of 50 artists>)
```

Example surface after a simulation of a 12 × 12 grid:

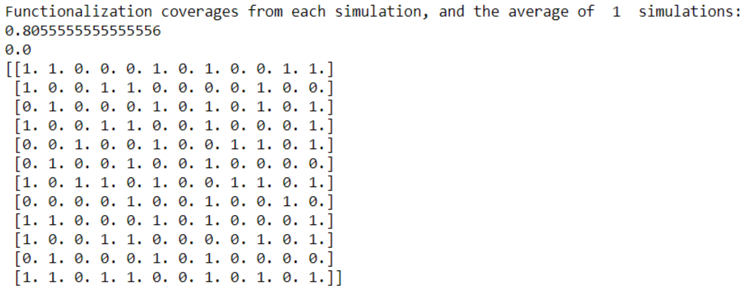

```
Functionalization coverages from each simulation, and the average of  1  simulations:
0.8055555555555556
0.0
[[1. 1. 0. 0. 0. 1. 0. 1. 0. 0. 1. 1.]
 [1. 0. 0. 1. 1. 0. 0. 0. 0. 1. 0. 0.]
 [0. 1. 0. 0. 0. 1. 0. 1. 0. 1. 0. 1.]
 [1. 0. 0. 1. 1. 0. 0. 1. 0. 0. 0. 1.]
 [0. 0. 1. 0. 0. 1. 0. 0. 1. 1. 0. 1.]
 [0. 1. 0. 0. 1. 0. 0. 1. 0. 0. 0. 0.]
 [1. 0. 1. 1. 0. 1. 0. 0. 1. 1. 0. 1.]
 [0. 0. 0. 0. 1. 0. 0. 1. 0. 0. 1. 0.]
 [1. 1. 0. 0. 0. 1. 0. 1. 0. 0. 0. 1.]
 [1. 0. 0. 1. 1. 0. 0. 0. 0. 1. 0. 1.]
 [0. 1. 0. 0. 0. 1. 0. 1. 0. 0. 0. 0.]
 [1. 1. 0. 1. 1. 0. 0. 1. 0. 1. 0. 1.]]
```

Bibliography

(1) Jenkins, T. A Brief History of ... Semiconductors. *Phys. Educ.* **2005**, *40* (5), 430. https://doi.org/10.1088/0031-9120/40/5/002.

(2) Tan, M. X.; Laibinis, P. E.; Nguyen, S. T.; Kesselman, J. M.; Stanton, C. E.; Lewis, N. S. Principles and Applications of Semiconductor Photoelectrochemistry. In *Progress in Inorganic Chemistry*; John Wiley & Sons, Ltd, 1994; pp 21–144. https://doi.org/10.1002/9780470166420.ch2.

(3) Fan, X.-L.; Yang, Y.; Xiao, P.; Lau, W.-M. Site-Specific Catalytic Activity in Exfoliated MoS_2 Single-Layer Polytypes for Hydrogen Evolution: Basal Plane and Edges. *J. Mater. Chem. A* **2014**, *2* (48), 20545–20551. https://doi.org/10.1039/C4TA05257A.

(4) Pal, B.; Singh, A.; G., S.; Mahale, P.; Kumar, A.; Thirupathaiah, S.; Sezen, H.; Amati, M.; Gregoratti, L.; Waghmare, U. V.; Sarma, D. D. Chemically Exfoliated MoS_2 Layers: Spectroscopic Evidence for the Semiconducting Nature of the Dominant Trigonal Metastable Phase. *Phys. Rev. B* **2017**, *96* (19), 195426. https://doi.org/10.1103/PhysRevB.96.195426.

(5) Tang, C. S.; Yin, X.; Wee, A. T. S. 1D Chain Structure in 1T′-Phase 2D Transition Metal Dichalcogenides and Their Anisotropic Electronic Structures. *Appl. Phys. Rev.* **2021**, *8* (1), 011313. https://doi.org/10.1063/5.0023799.

(6) Dasog, M.; Thompson, J. R.; Lewis, N. S. Oxidant-Activated Reactions of Nucleophiles with Silicon Nanocrystals. *Chem. Mater.* **2017**, *29* (16), 7002–7013. https://doi.org/10.1021/acs.chemmater.7b02572.

(7) Frontmatter. In *Functionalization of Semiconductor Surfaces*; John Wiley & Sons, Ltd, 2012; pp i–xx. https://doi.org/10.1002/9781118199770.fmatter.

(8) Chou, S. S.; Sai, N.; Lu, P.; Coker, E. N.; Liu, S.; Artyushkova, K.; Luk, T. S.; Kaehr, B.; Brinker, C. J. Understanding Catalysis in a Multiphasic Two-Dimensional Transition Metal Dichalcogenide. *Nat. Commun.* **2015**, *6* (1), 8311. https://doi.org/10.1038/ncomms9311.

(9) Zhang, S.-L.; Choi, H.-H.; Yue, H.-Y.; Yang, W.-C. Controlled Exfoliation of Molybdenum Disulfide for Developing Thin Film Humidity Sensor. *Curr. Appl. Phys.* **2014**, *14* (3), 264–268. https://doi.org/10.1016/j.cap.2013.11.031.

(10) Zheng, J.; Zhang, H.; Dong, S.; Liu, Y.; Tai Nai, C.; Suk Shin, H.; Young Jeong, H.; Liu, B.; Ping Loh, K. High Yield Exfoliation of Two-Dimensional Chalcogenides Using Sodium Naphthalenide. *Nat. Commun.* **2014**, *5* (1), 2995. https://doi.org/10.1038/ncomms3995.

(11) Nicolosi, V.; Chhowalla, M.; Kanatzidis, M. G.; Strano, M. S.; Coleman, J. N. Liquid Exfoliation of Layered Materials. *Science* **2013**, *340* (6139), 1226419. https://doi.org/10.1126/science.1226419.

(12) Voiry, D.; Goswami, A.; Kappera, R.; Silva, C. de C. C. e; Kaplan, D.; Fujita, T.; Chen, M.; Asefa, T.; Chhowalla, M. Covalent Functionalization of Monolayered Transition Metal Dichalcogenides by Phase Engineering. *Nat. Chem.* **2015**, *7* (1), 45–49. https://doi.org/10.1038/nchem.2108.

(13) Hinnemann, B.; Moses, P. G.; Bonde, J.; Jørgensen, K. P.; Nielsen, J. H.; Horch, S.; Chorkendorff, I.; Nørskov, J. K. Biomimetic Hydrogen Evolution: MoS_2

Nanoparticles as Catalyst for Hydrogen Evolution. *J. Am. Chem. Soc.* **2005**, *127* (15), 5308–5309. https://doi.org/10.1021/ja0504690.

(14) Voiry, D.; Salehi, M.; Silva, R.; Fujita, T.; Chen, M.; Asefa, T.; Shenoy, V. B.; Eda, G.; Chhowalla, M. Conducting MoS_2 Nanosheets as Catalysts for Hydrogen Evolution Reaction. *Nano Lett.* **2013**, *13* (12), 6222–6227. https://doi.org/10.1021/nl403661s.

(15) Ding, Q.; Song, B.; Xu, P.; Jin, S. Efficient Electrocatalytic and Photoelectrochemical Hydrogen Generation Using MoS_2 and Related Compounds. *Chem* **2016**, *1* (5), 699–726. https://doi.org/10.1016/j.chempr.2016.10.007.

(16) Kwon, K. C.; Choi, S.; Hong, K.; Moon, C. W.; Shim, Y.-S.; Kim, D. H.; Kim, T.; Sohn, W.; Jeon, J.-M.; Lee, C.-H.; Nam, K. T.; Han, S.; Kim, S. Y.; Jang, H. W. Wafer-Scale Transferable Molybdenum Disulfide Thin-Film Catalysts for Photoelectrochemical Hydrogen Production. *Energy Environ. Sci.* **2016**, *9* (7), 2240–2248. https://doi.org/10.1039/C6EE00144K.

(17) Li, H.; Tsai, C.; Koh, A. L.; Cai, L.; Contryman, A. W.; Fragapane, A. H.; Zhao, J.; Han, H. S.; Manoharan, H. C.; Abild-Pedersen, F.; Nørskov, J. K.; Zheng, X. Activating and Optimizing MoS_2 Basal Planes for Hydrogen Evolution through the Formation of Strained Sulphur Vacancies. *Nat. Mater.* **2016**, *15* (1), 48–53. https://doi.org/10.1038/nmat4465.

(18) Yin, Y.; Han, J.; Zhang, Y.; Zhang, X.; Xu, P.; Yuan, Q.; Samad, L.; Wang, X.; Wang, Y.; Zhang, Z.; Zhang, P.; Cao, X.; Song, B.; Jin, S. Contributions of Phase, Sulfur Vacancies, and Edges to the Hydrogen Evolution Reaction Catalytic Activity of Porous Molybdenum Disulfide Nanosheets. *J. Am. Chem. Soc.* **2016**, *138* (25), 7965–7972. https://doi.org/10.1021/jacs.6b03714.

(19) Wu, S.; Zeng, Z.; He, Q.; Wang, Z.; Wang, S. J.; Du, Y.; Yin, Z.; Sun, X.; Chen, W.; Zhang, H. Electrochemically Reduced Single-Layer MoS2 Nanosheets: Characterization, Properties, and Sensing Applications. *Small* **2012**, *8* (14), 2264–2270. https://doi.org/10.1002/smll.201200044.

(20) Akbari, E.; Jahanbin, K.; Afroozeh, A.; Yupapin, P.; Buntat, Z. Brief Review of Monolayer Molybdenum Disulfide Application in Gas Sensor. *Phys. B Condens. Matter* **2018**, *545*, 510–518. https://doi.org/10.1016/j.physb.2018.06.033.

(21) Chou, S. S.; Kaehr, B.; Kim, J.; Foley, B. M.; De, M.; Hopkins, P. E.; Huang, J.; Brinker, C. J.; Dravid, V. P. Chemically Exfoliated MoS_2 as Near-Infrared Photothermal Agents. *Angew. Chem. Int. Ed.* **2013**, *52* (15), 4160–4164. https://doi.org/10.1002/anie.201209229.

(22) Soria, F. A.; Patrito, E. M.; Paredes-Olivera, P. Oxidation of Hydrogenated Si(111) by a Radical Propagation Mechanism. *J. Phys. Chem. C* **2012**, *116* (46), 24607–24615. https://doi.org/10.1021/jp307798s.

(23) Linford, M. R.; Chidsey, C. E. D. Alkyl Monolayers Covalently Bonded to Silicon Surfaces. *J. Am. Chem. Soc.* **1993**, *115* (26), 12631–12632. https://doi.org/10.1021/ja00079a071.

(24) Thissen, P.; Seitz, O.; Chabal, Y. J. Wet Chemical Surface Functionalization of Oxide-Free Silicon. *Prog. Surf. Sci.* **2012**, *87* (9), 272–290. https://doi.org/10.1016/j.progsurf.2012.10.003.

(25) Buriak, J. M. Organometallic Chemistry on Silicon Surfaces: Formation of Functional Monolayers Bound through Si–C Bonds. *Chem. Commun.* **1999**, No. 12, 1051–1060. https://doi.org/10.1039/A900108E.

(26) Sieval, A. B.; Linke, R.; Zuilhof, H.; Sudhölter, E. J. R. High-Quality Alkyl Monolayers on Silicon Surfaces. *Adv. Mater.* **2000**, *12* (19), 1457–1460. https://doi.org/10.1002/1521-4095(200010)12:19<1457::AID-ADMA1457>3.0.CO;2-#.

(27) Yu, W. H.; Kang, E. T.; Neoh, K. G.; Zhu, S. Controlled Grafting of Well-Defined Polymers on Hydrogen-Terminated Silicon Substrates by Surface-Initiated Atom Transfer Radical Polymerization. *J. Phys. Chem. B* **2003**, *107* (37), 10198–10205. https://doi.org/10.1021/jp034330s.

(28) Bansal, A.; Li, X.; Lauermann, I.; Lewis, N. S.; Yi, S. I.; Weinberg, W. H. Alkylation of Si Surfaces Using a Two-Step Halogenation/Grignard Route. *J. Am. Chem. Soc.* **1996**, *118* (30), 7225–7226. https://doi.org/10.1021/ja960348n.

(29) Liu, W.; Sharp, I. D.; Tilley, T. D. Multifunctional Silicon Surfaces: Reaction of Dichlorocarbene Generated from Seyferth Reagent with Hydrogen-Terminated Silicon (111) Surfaces. *Langmuir* **2014**, *30* (1), 172–178. https://doi.org/10.1021/la403789a.

(30) Zhukhovitskiy, A. V.; Mavros, M. G.; Queeney, K. T.; Wu, T.; Van Voorhis, T.; Johnson, J. A. Reactions of Persistent Carbenes with Hydrogen-Terminated Silicon Surfaces. *J. Am. Chem. Soc.* **2016**, *138* (27), 8639–8652. https://doi.org/10.1021/jacs.6b04962.

(31) Stewart, M. P.; Maya, F.; Kosynkin, D. V.; Dirk, S. M.; Stapleton, J. J.; McGuiness, C. L.; Allara, D. L.; Tour, J. M. Direct Covalent Grafting of Conjugated Molecules onto Si, GaAs, and Pd Surfaces from Aryldiazonium Salts. *J. Am. Chem. Soc.* **2004**, *126* (1), 370–378. https://doi.org/10.1021/ja0383120.

(32) Bélanger, D.; Pinson, J. Electrografting: A Powerful Method for Surface Modification. *Chem. Soc. Rev.* **2011**, *40* (7), 3995–4048. https://doi.org/10.1039/C0CS00149J.

(33) Hurley, P. T.; Ribbe, A. E.; Buriak, J. M. Nanopatterning of Alkynes on Hydrogen-Terminated Silicon Surfaces by Scanning Probe-Induced Cathodic Electrografting. *J. Am. Chem. Soc.* **2003**, *125* (37), 11334–11339. https://doi.org/10.1021/ja035857l.

(34) Fellah, S.; Teyssot, A.; Ozanam, F.; Chazalviel, J.-N.; Vigneron, J.; Etcheberry, A. Kinetics of Electrochemical Derivatization of the Silicon Surface by Grignards. *Langmuir* **2002**, *18* (15), 5851–5860. https://doi.org/10.1021/la0203739.

(35) Wong, K. T.; Lewis, N. S. What a Difference a Bond Makes: The Structural, Chemical, and Physical Properties of Methyl-Terminated Si(111) Surfaces. *Acc. Chem. Res.* **2014**, *47* (10), 3037–3044. https://doi.org/10.1021/ar500207y.

(36) Vilan, A.; Yaffe, O.; Biller, A.; Salomon, A.; Kahn, A.; Cahen, D. Molecules on Si: Electronics with Chemistry. *Adv. Mater.* **2010**, *22* (2), 140–159. https://doi.org/10.1002/adma.200901834.

(37) Vilan, A.; Cahen, D. Chemical Modification of Semiconductor Surfaces for Molecular Electronics. *Chem. Rev.* **2017**, *117* (5), 4624–4666. https://doi.org/10.1021/acs.chemrev.6b00746.

(38) Veerbeek, J.; Huskens, J. Applications of Monolayer-Functionalized H-Terminated Silicon Surfaces: A Review. *Small Methods* **2017**, *1* (4), 1700072. https://doi.org/10.1002/smtd.201700072.

(39) Strother, T.; Cai, W.; Zhao, X.; Hamers, R. J.; Smith, L. M. Synthesis and Characterization of DNA-Modified Silicon (111) Surfaces. *J. Am. Chem. Soc.* **2000**, *122* (6), 1205–1209. https://doi.org/10.1021/ja9936161.

(40) Gouget-Laemmel, A. C.; Yang, J.; Lodhi, M. A.; Siriwardena, A.; Aureau, D.; Boukherroub, R.; Chazalviel, J.-N.; Ozanam, F.; Szunerits, S. Functionalization of Azide-Terminated Silicon Surfaces with Glycans Using Click Chemistry: XPS and FTIR Study. *J. Phys. Chem. C* **2013**, *117* (1), 368–375. https://doi.org/10.1021/jp309866d.

(41) Khaldi, K.; Sam, S.; Gouget-Laemmel, A. C.; Henry de Villeneuve, C.; Moraillon, A.; Ozanam, F.; Yang, J.; Kermad, A.; Ghellai, N.; Gabouze, N. Active Acetylcholinesterase Immobilization on a Functionalized Silicon Surface. *Langmuir* **2015**, *31* (30), 8421–8428. https://doi.org/10.1021/acs.langmuir.5b01928.

(42) Fabre, B.; Hauquier, F. Boronic Acid-Functionalized Oxide-Free Silicon Surfaces for the Electrochemical Sensing of Dopamine. *Langmuir* **2017**, *33* (35), 8693–8699. https://doi.org/10.1021/acs.langmuir.7b00699.

(43) Zhang, F.; Sun, B.; Song, T.; Zhu, X.; Lee, S. Air Stable, Efficient Hybrid Photovoltaic Devices Based on Poly(3-Hexylthiophene) and Silicon Nanostructures. *Chem. Mater.* **2011**, *23* (8), 2084–2090. https://doi.org/10.1021/cm103221a.

(44) Grimm, R. L.; Bierman, M. J.; O'Leary, L. E.; Strandwitz, N. C.; Brunschwig, B. S.; Lewis, N. S. Comparison of the Photoelectrochemical Behavior of H-Terminated and Methyl-Terminated Si(111) Surfaces in Contact with a Series of One-Electron, Outer-Sphere Redox Couples in CH3CN. *J. Phys. Chem. C* **2012**, *116* (44), 23569–23576. https://doi.org/10.1021/jp308461q.

(45) Doiron, C. W.; Fitzpatrick, N. A.; Masucci, C. P.; Martin, J. L.; Carl, A. D.; Grimm, R. L. Open-Circuit Photovoltage Exceeding 950 MV with an 840 MV Average at Sb2S3–Thianthrene+/0 Junctions Enabled by Thioperylene Anhydride Back Contacts. *ACS Omega* **2020**, *5* (27), 16875–16884. https://doi.org/10.1021/acsomega.0c02077.

(46) Hessel, C. M.; Henderson, E. J.; Veinot, J. G. C. Hydrogen Silsesquioxane: A Molecular Precursor for Nanocrystalline Si-SiO2 Composites and Freestanding Hydride-Surface-Terminated Silicon Nanoparticles. *Chem. Mater.* **2006**, *18*, 6139–6146.

(47) Henderson, E. J.; Kelly, J. A.; Veinot, J. G. C. Influence of HSiO $_{1.5}$ Sol−Gel Polymer Structure and Composition on the Size and Luminescent Properties of Silicon Nanocrystals. *Chem. Mater.* **2009**, *21* (22), 5426–5434. https://doi.org/10.1021/cm902028q.

(48) Clark, R. J.; Aghajamali, M.; Gonzalez, C. M.; Hadidi, L.; Islam, M. A.; Javadi, M.; Mobarok, M. H.; Purkait, T. K.; Robidillo, C. J. T.; Sinelnikov, R.; Thiessen, A. N.; Washington, J.; Yu, H.; Veinot, J. G. C. From Hydrogen Silsesquioxane to Functionalized Silicon Nanocrystals. *Chem. Mater.* **2017**, *29* (1), 80–89. https://doi.org/10.1021/acs.chemmater.6b02667.

(49) Zhai, Y.; Dasog, M.; Snitynsky, R. B.; Purkait, T. K.; Aghajamali, M.; Hahn, A. H.; Sturdy, C. B.; Lowary, T. L.; Veinot, J. G. C. Water-Soluble Photoluminescent D -Mannose and L -Alanine Functionalized Silicon Nanocrystals and Their Application to Cancer Cell Imaging. *J. Mater. Chem. B* **2014**, *2* (47), 8427–8433. https://doi.org/10.1039/C4TB01161A.

(50) Lin, T.; Liu, X.; Zhou, B.; Zhan, Z.; Cartwright, A. N.; Swihart, M. T. A Solution-Processed UV-Sensitive Photodiode Produced Using a New Silicon Nanocrystal Ink. *Adv. Funct. Mater.* **2014**, *24* (38), 6016–6022. https://doi.org/10.1002/adfm.201400600.

(51) Maier-Flaig, F.; Rinck, J.; Stephan, M.; Bocksrocker, T.; Bruns, M.; Kübel, C.; Powell, A. K.; Ozin, G. A.; Lemmer, U. Multicolor Silicon Light-Emitting Diodes (SiLEDs). *Nano Lett.* **2013**, *13* (2), 475–480. https://doi.org/10.1021/nl3038689.

(52) Robidillo, C. J. T.; Aghajamali, M.; Faramus, A.; Sinelnikov, R.; Veinot, J. G. C. Interfacing Enzymes with Silicon Nanocrystals through the Thiol–Ene Reaction. *Nanoscale* **2018**, *10* (39), 18706–18719. https://doi.org/10.1039/C8NR05368E.

(53) Inoue, A.; Sugimoto, H.; Fujii, M. Silver Nanoparticles Stabilized with a Silicon Nanocrystal Shell and Their Antimicrobial Activity. *RSC Adv.* **2019**, *9* (27), 15171–15176. https://doi.org/10.1039/C9RA02559F.

(54) Heine, T. Transition Metal Chalcogenides: Ultrathin Inorganic Materials with Tunable Electronic Properties. *Acc. Chem. Res.* **2015**, *48* (1), 65–72. https://doi.org/10.1021/ar500277z.

(55) Calandra, M. Chemically Exfoliated Single-Layer MoS_2 : Stability, Lattice Dynamics, and Catalytic Adsorption from First Principles. *Phys. Rev. B* **2013**, *88* (24), 245428. https://doi.org/10.1103/PhysRevB.88.245428.

(56) Chhowalla, M.; Shin, H. S.; Eda, G.; Li, L.-J.; Loh, K. P.; Zhang, H. The Chemistry of Two-Dimensional Layered Transition Metal Dichalcogenide Nanosheets. *Nat. Chem.* **2013**, *5* (4), 263–275. https://doi.org/10.1038/nchem.1589.

(57) Jariwala, D.; Sangwan, V. K.; Lauhon, L. J.; Marks, T. J.; Hersam, M. C. Emerging Device Applications for Semiconducting Two-Dimensional Transition Metal Dichalcogenides. *ACS Nano* **2014**, *8* (2), 1102–1120. https://doi.org/10.1021/nn500064s.

(58) Duan, X.; Wang, C.; Pan, A.; Yu, R.; Duan, X. Two-Dimensional Transition Metal Dichalcogenides as Atomically Thin Semiconductors: Opportunities and Challenges. *Chem. Soc. Rev.* **2015**, *44* (24), 8859–8876. https://doi.org/10.1039/C5CS00507H.

(59) Cho, B.; Hahm, M. G.; Choi, M.; Yoon, J.; Kim, A. R.; Lee, Y.-J.; Park, S.-G.; Kwon, J.-D.; Kim, C. S.; Song, M.; Jeong, Y.; Nam, K.-S.; Lee, S.; Yoo, T. J.; Kang, C. G.; Lee, B. H.; Ko, H. C.; Ajayan, P. M.; Kim, D.-H. Charge-Transfer-Based Gas Sensing Using Atomic-Layer MoS2. *Sci. Rep.* **2015**, *5* (1), 8052. https://doi.org/10.1038/srep08052.

(60) Park, M.; Park, Y. J.; Chen, X.; Park, Y.-K.; Kim, M.-S.; Ahn, J.-H. MoS_2-Based Tactile Sensor for Electronic Skin Applications. *Adv. Mater.* **2016**, *28* (13), 2556–2562. https://doi.org/10.1002/adma.201505124.

(61) Deng, D.; Novoselov, K. S.; Fu, Q.; Zheng, N.; Tian, Z.; Bao, X. Catalysis with Two-Dimensional Materials and Their Heterostructures. *Nat. Nanotechnol.* **2016**, *11* (3), 218–230. https://doi.org/10.1038/nnano.2015.340.

(62) Wang, H.; Lu, Z.; Xu, S.; Kong, D.; Cha, J. J.; Zheng, G.; Hsu, P.-C.; Yan, K.; Bradshaw, D.; Prinz, F. B.; Cui, Y. Electrochemical Tuning of Vertically Aligned MoS_2 Nanofilms and Its Application in Improving Hydrogen Evolution Reaction. *Proc. Natl. Acad. Sci.* **2013**, *110* (49), 19701–19706. https://doi.org/10.1073/pnas.1316792110.

(63) Yadav, V.; Roy, S.; Singh, P.; Khan, Z.; Jaiswal, A. 2D MoS_2-Based Nanomaterials for Therapeutic, Bioimaging, and Biosensing Applications. *Small* **2019**, *15* (1), 1803706. https://doi.org/10.1002/smll.201803706.

(64) Deng, R.; Yi, H.; Fan, F.; Fu, L.; Zeng, Y.; Wang, Y.; Li, Y.; Liu, Y.; Ji, S.; Su, Y. Facile Exfoliation of MoS 2 Nanosheets by Protein as a Photothermal-Triggered Drug Delivery System for Synergistic Tumor Therapy. *RSC Adv.* **2016**, *6* (80), 77083–77092. https://doi.org/10.1039/C6RA13993K.

(65) Yin, W.; Yan, L.; Yu, J.; Tian, G.; Zhou, L.; Zheng, X.; Zhang, X.; Yong, Y.; Li, J.; Gu, Z.; Zhao, Y. High-Throughput Synthesis of Single-Layer MoS_2 Nanosheets as a Near-Infrared Photothermal-Triggered Drug Delivery for Effective Cancer Therapy. *ACS Nano* **2014**, *8* (7), 6922–6933. https://doi.org/10.1021/nn501647j.

(66) Wang, S.; Chen, Y.; Li, X.; Gao, W.; Zhang, L.; Liu, J.; Zheng, Y.; Chen, H.; Shi, J. Injectable 2D MoS_2-Integrated Drug Delivering Implant for Highly Efficient NIR-Triggered Synergistic Tumor Hyperthermia. *Adv. Mater.* **2015**, *27* (44), 7117–7122. https://doi.org/10.1002/adma.201503869.

(67) Yin, F.; Anderson, T.; Panwar, N.; Zhang, K.; Tjin, S. C.; Ng, B. K.; Yoon, H. S.; Qu, J.; Yong, K.-T. Functionalized MoS_2 Nanosheets as Multi-Gene Delivery Vehicles for *In Vivo* Pancreatic Cancer Therapy. *Nanotheranostics* **2018**, *2* (4), 371–386. https://doi.org/10.7150/ntno.27308.

(68) Kim, T. I.; Kim, J.; Park, I.-J.; Cho, K.-O.; Choi, S.-Y. Chemically Exfoliated 1T-Phase Transition Metal Dichalcogenide Nanosheets for Transparent Antibacterial Applications. *2D Mater.* **2019**, *6* (2), 025025. https://doi.org/10.1088/2053-1583/ab070e.

(69) Tang, K.; Wang, L.; Geng, H.; Qiu, J.; Cao, H.; Liu, X. Molybdenum Disulfide (MoS_2) Nanosheets Vertically Coated on Titanium for Disinfection in the Dark. *Arab. J. Chem.* **2020**, *13* (1), 1612–1623. https://doi.org/10.1016/j.arabjc.2017.12.013.

(70) Chou, S. S.; De, M.; Kim, J.; Byun, S.; Dykstra, C.; Yu, J.; Huang, J.; Dravid, V. P. Ligand Conjugation of Chemically Exfoliated MoS_2. *J. Am. Chem. Soc.* **2013**, *135* (12), 4584–4587. https://doi.org/10.1021/ja310929s.

(71) Chen, X.; McDonald, A. R. Functionalization of Two-Dimensional Transition-Metal Dichalcogenides. *Adv. Mater.* **2016**, *28* (27), 5738–5746. https://doi.org/10.1002/adma.201505345.

(72) Benson, E. E.; Zhang, H.; Schuman, S. A.; Nanayakkara, S. U.; Bronstein, N. D.; Ferrere, S.; Blackburn, J. L.; Miller, E. M. Balancing the Hydrogen Evolution Reaction, Surface Energetics, and Stability of Metallic MoS_2 Nanosheets via Covalent Functionalization. *J. Am. Chem. Soc.* **2018**, *140* (1), 441–450. https://doi.org/10.1021/jacs.7b11242.

(73) Ding, Q.; Czech, K. J.; Zhao, Y.; Zhai, J.; Hamers, R. J.; Wright, J. C.; Jin, S. Basal-Plane Ligand Functionalization on Semiconducting 2H-MoS_2 Monolayers.

ACS Appl. Mater. Interfaces **2017**, *9* (14), 12734–12742. https://doi.org/10.1021/acsami.7b01262.

(74) Chu, X. S.; Yousaf, A.; Li, D. O.; Tang, A. A.; Debnath, A.; Ma, D.; Green, A. A.; Santos, E. J. G.; Wang, Q. H. Direct Covalent Chemical Functionalization of Unmodified Two-Dimensional Molybdenum Disulfide. *Chem. Mater.* **2018**, *30* (6), 2112–2128. https://doi.org/10.1021/acs.chemmater.8b00173.

(75) Shen, J.; Wu, J.; Wang, M.; Ge, Y.; Dong, P.; Baines, R.; Brunetto, G.; Machado, L. D.; Ajayan, P. M.; Ye, M. Insight into In Situ Amphiphilic Functionalization of Few-Layered Transition Metal Dichalcogenide Nanosheets. *Adv. Mater.* **2016**, *28* (38), 8469–8476. https://doi.org/10.1002/adma.201602887.

(76) Vera-Hidalgo, M.; Giovanelli, E.; Navío, C.; Pérez, E. M. Mild Covalent Functionalization of Transition Metal Dichalcogenides with Maleimides: A “Click” Reaction for 2H-MoS_2 and WS_2. *J. Am. Chem. Soc.* **2019**, *141* (9), 3767–3771. https://doi.org/10.1021/jacs.8b10930.

(77) Quirós-Ovies, R.; Vázquez Sulleiro, M.; Vera-Hidalgo, M.; Prieto, J.; Gómez, I. J.; Sebastián, V.; Santamaría, J.; Pérez, E. M. Controlled Covalent Functionalization of 2H-MoS_2 with Molecular or Polymeric Adlayers. *Chem. – Eur. J.* **2020**, *26* (29), 6629–6634. https://doi.org/10.1002/chem.202000068.

(78) Vázquez Sulleiro, M.; Quirós-Ovies, R.; Vera-Hidalgo, M.; Gómez, I. J.; Sebastián, V.; Santamaría, J.; Pérez, E. M. Covalent Cross-Linking of 2H-MoS_2 Nanosheets. *Chem. – Eur. J.* **2021**, *27* (9), 2993–2996. https://doi.org/10.1002/chem.202004366.

(79) Knirsch, K. C.; Berner, N. C.; Nerl, H. C.; Cucinotta, C. S.; Gholamvand, Z.; McEvoy, N.; Wang, Z.; Abramovic, I.; Vecera, P.; Halik, M.; Sanvito, S.; Duesberg, G. S.; Nicolosi, V.; Hauke, F.; Hirsch, A.; Coleman, J. N.; Backes, C. Basal-Plane Functionalization of Chemically Exfoliated Molybdenum Disulfide by Diazonium Salts. *ACS Nano* **2015**, *9* (6), 6018–6030. https://doi.org/10.1021/acsnano.5b00965.

(80) Vishnoi, P.; Sampath, A.; Waghmare, U. V.; Rao, C. N. R. Covalent Functionalization of Nanosheets of MoS_2 and $MoSe_2$ by Substituted Benzenes and Other Organic Molecules. *Chem. – Eur. J.* **2017**, *23* (4), 886–895. https://doi.org/10.1002/chem.201604176.

(81) Yan, E. X.; Cabán-Acevedo, M.; Papadantonakis, K. M.; Brunschwig, B. S.; Lewis, N. S. Reductant-Activated, High-Coverage, Covalent Functionalization of 1T′-MoS_2. *ACS Mater. Lett.* **2020**, *2* (2), 133–139. https://doi.org/10.1021/acsmaterialslett.9b00241.

(82) Manjunatha, S.; Rajesh, S.; Vishnoi, P.; Rao, C. N. R. Reaction with Organic Halides as a General Method for the Covalent Functionalization of Nanosheets of 2D Chalcogenides and Related Materials. *J. Mater. Res.* **2017**, *32* (15), 2984–2992. https://doi.org/10.1557/jmr.2017.224.

(83) Canton-Vitoria, R.; Sayed-Ahmad-Baraza, Y.; Pelaez-Fernandez, M.; Arenal, R.; Bittencourt, C.; Ewels, C. P.; Tagmatarchis, N. Functionalization of MoS_2 with 1,2-Dithiolanes: Toward Donor-Acceptor Nanohybrids for Energy Conversion. *npj 2D Mater. Appl.* **2017**, *1* (1), 1–9. https://doi.org/10.1038/s41699-017-0012-8.

(84) Backes, C.; Berner, N. C.; Chen, X.; Lafargue, P.; LaPlace, P.; Freeley, M.; Duesberg, G. S.; Coleman, J. N.; McDonald, A. R. Functionalization of Liquid-

Exfoliated Two-Dimensional 2H-MoS_2. *Angew. Chem. Int. Ed.* **2015**, *54* (9), 2638–2642. https://doi.org/10.1002/anie.201409412.

(85) Heising, J.; Kanatzidis, M. G. Exfoliated and Restacked MoS_2 and WS_2: Ionic or Neutral Species? Encapsulation and Ordering of Hard Electropositive Cations. *J. Am. Chem. Soc.* **1999**, *121* (50), 11720–11732. https://doi.org/10.1021/ja991644d.

(86) Yu, H.; Webb, L. J.; Ries, R. S.; Solares, S. D.; Goddard, W. A.; Heath, J. R.; Lewis, N. S. Low-Temperature STM Images of Methyl-Terminated Si(111) Surfaces. *J. Phys. Chem. B* **2005**, *109* (2), 671–674. https://doi.org/10.1021/jp047672m.

(87) Huang, Y.; Nielsen, R. J.; Goddard, W. A. Reaction Mechanism for the Hydrogen Evolution Reaction on the Basal Plane Sulfur Vacancy Site of MoS_2 Using Grand Canonical Potential Kinetics. *J. Am. Chem. Soc.* **2018**, *140* (48), 16773–16782. https://doi.org/10.1021/jacs.8b10016.

(88) Tang, Q.; Jiang, D. Stabilization and Band-Gap Tuning of the 1T-MoS2 Monolayer by Covalent Functionalization. *Chem. Mater.* **2015**, *27* (10), 3743–3748. https://doi.org/10.1021/acs.chemmater.5b00986.

(89) Kresse, G.; Hafner, J. Ab Initio Molecular-Dynamics Simulation of the Liquid-Metal--Amorphous-Semiconductor Transition in Germanium. *Phys. Rev. B* **1994**, *49* (20), 14251–14269. https://doi.org/10.1103/PhysRevB.49.14251.

(90) Kresse, G.; Furthmüller, J. Efficient Iterative Schemes for Ab Initio Total-Energy Calculations Using a Plane-Wave Basis Set. *Phys. Rev. B* **1996**, *54* (16), 11169–11186. https://doi.org/10.1103/PhysRevB.54.11169.

(91) Perdew, J. P.; Burke, K.; Ernzerhof, M. Generalized Gradient Approximation Made Simple. *Phys. Rev. Lett.* **1996**, *77* (18), 3865–3868. https://doi.org/10.1103/PhysRevLett.77.3865.

(92) Johnson, E. R.; Becke, A. D. A Post-Hartree-Fock Model of Intermolecular Interactions: Inclusion of Higher-Order Corrections. *J. Chem. Phys.* **2006**, *124* (17), 174104. https://doi.org/10.1063/1.2190220.

(93) Mathew, K.; Kolluru, V. S. C.; Mula, S.; Steinmann, S. N.; Hennig, R. G. Implicit Self-Consistent Electrolyte Model in Plane-Wave Density-Functional Theory. *J. Chem. Phys.* **2019**, *151* (23), 234101. https://doi.org/10.1063/1.5132354.

(94) Henkelman, G.; Uberuaga, B. P.; Jónsson, H. A Climbing Image Nudged Elastic Band Method for Finding Saddle Points and Minimum Energy Paths. *J. Chem. Phys.* **2000**, *113* (22), 9901–9904. https://doi.org/10.1063/1.1329672.

(95) Sundararaman, R.; Letchworth-Weaver, K.; Schwarz, K. A.; Gunceler, D.; Ozhabes, Y.; Arias, T. A. JDFTx: Software for Joint Density-Functional Theory. *SoftwareX* **2017**, *6*, 278–284. https://doi.org/10.1016/j.softx.2017.10.006.

(96) Sundararaman, R.; Goddard, W. A. The Charge-Asymmetric Nonlocally Determined Local-Electric (CANDLE) Solvation Model. *J. Chem. Phys.* **2015**, *142* (6), 064107. https://doi.org/10.1063/1.4907731.

(97) Goodpaster, J. D.; Bell, A. T.; Head-Gordon, M. Identification of Possible Pathways for C–C Bond Formation during Electrochemical Reduction of CO2: New Theoretical Insights from an Improved Electrochemical Model. *J. Phys. Chem. Lett.* **2016**, *7* (8), 1471–1477. https://doi.org/10.1021/acs.jpclett.6b00358.

(98) Abidi, N.; Lim, K. R. G.; Seh, Z. W.; Steinmann, S. N. Atomistic Modeling of Electrocatalysis: Are We There Yet? *WIREs Comput. Mol. Sci.* **2021**, *11* (3), e1499. https://doi.org/10.1002/wcms.1499.

(99) Golub', A. S.; Protsenko, G. A.; Gumileva, L. V.; Buyanovskaya, A. G.; Novikov, Yu. N. The Formation of Intercalation Compounds of MoS2 with Cations of Alkali Metals and Alkylammonium from Monolayer Dispersion of Molybdenum Disulfide. *Russ. Chem. Bull.* **1993**, *42* (4), 632–634. https://doi.org/10.1007/BF00703994.

(100) Sanville, E.; Kenny, S. D.; Smith, R.; Henkelman, G. Improved grid-based algorithm for Bader charge allocation. *J. Comput. Chem.* **2007**, *28* (5), 899–908. https://doi.org/10.1002/jcc.20575.

(101) Li, Y.; O'Leary, L. E.; Lewis, N. S.; Galli, G. Combined Theoretical and Experimental Study of Band-Edge Control of Si through Surface Functionalization. *J. Phys. Chem. C* **2013**, *117* (10), 5188–5194. https://doi.org/10.1021/jp3124583.

(102) Cabán-Acevedo, M.; Papadantonakis, K. M.; Brunschwig, B. S.; Lewis, N. S. Surface Passivation and Positive Band-Edge Shift of p-Si(111) Surfaces Functionalized with Mixed Methyl/Trifluoromethylphenylacetylene Overlayers. *J. Phys. Chem. C* **2020**, *124* (30), 16338–16349. https://doi.org/10.1021/acs.jpcc.0c02017.

(103) Li, Y.; Calder, S.; Yaffe, O.; Cahen, D.; Haick, H.; Kronik, L.; Zuilhof, H. Hybrids of Organic Molecules and Flat, Oxide-Free Silicon: High-Density Monolayers, Electronic Properties, and Functionalization. *Langmuir* **2012**, *28* (26), 9920–9929. https://doi.org/10.1021/la3010568.

(104) Ciampi, S.; Harper, J. B.; Gooding, J. J. Wet Chemical Routes to the Assembly of Organic Monolayers on Silicon Surfaces via the Formation of Si–C Bonds: Surface Preparation, Passivation and Functionalization. *Chem. Soc. Rev.* **2010**, *39* (6), 2158–2183. https://doi.org/10.1039/B923890P.

(105) Purkait, T. K.; Iqbal, M.; Wahl, M. H.; Gottschling, K.; Gonzalez, C. M.; Islam, M. A.; Veinot, J. G. C. Borane-Catalyzed Room-Temperature Hydrosilylation of Alkenes/Alkynes on Silicon Nanocrystal Surfaces. *J. Am. Chem. Soc.* **2014**, *136* (52), 17914–17917. https://doi.org/10.1021/ja510120e.

(106) Plymale, N. T.; Dasog, M.; Brunschwig, B. S.; Lewis, N. S. A Mechanistic Study of the Oxidative Reaction of Hydrogen-Terminated Si(111) Surfaces with Liquid Methanol. *J. Phys. Chem. C* **2017**, *121* (8), 4270–4282. https://doi.org/10.1021/acs.jpcc.6b11555.

(107) Liu, Y.; Yamazaki, S.; Izuhara, S. Modification and Chemical Transformation of Si(111) Surface. *J. Organomet. Chem.* **2006**, *691* (26), 5809–5824. https://doi.org/10.1016/j.jorganchem.2006.09.048.

(108) Sato, S.; Swihart, M. T. Propionic-Acid-Terminated Silicon Nanoparticles: Synthesis and Optical Characterization. *Chem. Mater.* **2006**, *18* (17), 4083–4088. https://doi.org/10.1021/cm060750t.

(109) Bywalez, R.; Karacuban, H.; Nienhaus, H.; Schulz, C.; Wiggers, H. Stabilization of Mid-Sized Silicon Nanoparticles by Functionalization with Acrylic Acid. *Nanoscale Res. Lett.* **2012**, *7* (1), 76. https://doi.org/10.1186/1556-276X-7-76.

(110) Fujita, M.; Iizuka, Y.; Miyake, A. Thermal and Kinetic Analyses on Michael Addition Reaction of Acrylic Acid. *J. Therm. Anal. Calorim.* **2017**, *128* (2), 1227–1233. https://doi.org/10.1007/s10973-016-5985-6.

(111) Chalkley, M. J.; Oyala, P. H.; Peters, J. C. Cp* Noninnocence Leads to a Remarkably Weak C–H Bond via Metallocene Protonation. *J. Am. Chem. Soc.* **2019**, *141* (11), 4721–4729. https://doi.org/10.1021/jacs.9b00193.

(112) Aureau, D.; Ozanam, F.; Allongue, P.; Chazalviel, J.-N. The Titration of Carboxyl-Terminated Monolayers Revisited: In Situ Calibrated Fourier Transform Infrared Study of Well-Defined Monolayers on Silicon. *Langmuir* **2008**, *24* (17), 9440–9448. https://doi.org/10.1021/la801219u.

(113) Douarche, C.; Cortès, R.; Henry de Villeneuve, C.; Roser, S. J.; Braslau, A. DNA Adsorption at Functionalized Si/Buffer Interfaces Studied by x-Ray Reflectivity. *J. Chem. Phys.* **2008**, *128* (22), 225108. https://doi.org/10.1063/1.2927256.

(114) Nguyen, H. M.; Seitz, O.; Aureau, D.; Sra, A.; Nijem, N.; Gartstein, Yu. N.; Chabal, Y. J.; Malko, A. V. Spectroscopic Evidence for Nonradiative Energy Transfer between Colloidal CdSe/ZnS Nanocrystals and Functionalized Silicon Substrates. *Appl. Phys. Lett.* **2011**, *98* (16), 161904. https://doi.org/10.1063/1.3579545.

(115) Peng, W.; Rupich, S. M.; Shafiq, N.; Gartstein, Y. N.; Malko, A. V.; Chabal, Y. J. Silicon Surface Modification and Characterization for Emergent Photovoltaic Applications Based on Energy Transfer. *Chem. Rev.* **2015**, *115* (23), 12764–12796. https://doi.org/10.1021/acs.chemrev.5b00085.

(116) Mayer, T.; Hunger, R.; Klein, A.; Jaegermann, W. Engineering the Line up of Electronic Energy Levels at Inorganic–Organic Semiconductor Interfaces by Variation of Surface Termination and by Substitution. *Phys. Status Solidi B* **2008**, *245* (9), 1838–1848. https://doi.org/10.1002/pssb.200879542.

(117) Higashi, G. S.; Chabal, Y. J.; Trucks, G. W.; Raghavachari, K. Ideal Hydrogen Termination of the Si (111) Surface. *Appl. Phys. Lett.* **1990**, *56* (7), 656–658. https://doi.org/10.1063/1.102728.

(118) EC-Lab Application Note 29. In *Ohmic Drop, Part III: Suitable Use of the ZIR Techniques*; BioLogic, 2010; pp 1–5.

(119) Bard, A. J. *Standard Potentials in Aqueous Solution*, 1st ed.; Routledge: New York, 2017. https://doi.org/10.1201/9780203738764.

(120) Webb, L. J.; Rivillon, S.; Michalak, D. J.; Chabal, Y. J.; Lewis, N. S. Transmission Infrared Spectroscopy of Methyl- and Ethyl-Terminated Silicon(111) Surfaces. *J. Phys. Chem. B* **2006**, *110* (14), 7349–7356. https://doi.org/10.1021/jp054618c.

(121) Bansal, A.; Lewis, N. S. Stabilization of Si Photoanodes in Aqueous Electrolytes through Surface Alkylation. *J. Phys. Chem. B* **1998**, *102* (21), 4058–4060. https://doi.org/10.1021/jp980679h.

(122) Tufts, B. J.; Abrahams, I. L.; Caley, C. E.; Lunt, S. R.; Miskelly, G. M.; Sailor, M. J.; Santangelo, P. G.; Lewis, N. S.; Roe, A. L.; Hodgson, K. O. XPS and EXAFS Studies of the Reactions of Cobalt(III) Ammine Complexes with Gallium Arsenide Surfaces. *J. Am. Chem. Soc.* **1990**, *112* (13), 5123–5136. https://doi.org/10.1021/ja00169a021.

(123) Wasserman, S. R.; Tao, Y. T.; Whitesides, G. M. Structure and Reactivity of Alkylsiloxane Monolayers Formed by Reaction of Alkyltrichlorosilanes on Silicon Substrates. *Langmuir* **1989**, *5* (4), 1074–1087. https://doi.org/10.1021/la00088a035.
(124) Peng, F.; Su, Y.; Zhong, Y.; Fan, C.; Lee, S.-T.; He, Y. Silicon Nanomaterials Platform for Bioimaging, Biosensing, and Cancer Therapy. *Acc. Chem. Res.* **2014**, *47* (2), 612–623. https://doi.org/10.1021/ar400221g.
(125) Dasog, M.; Kehrle, J.; Rieger, B.; Veinot, J. G. C. Silicon Nanocrystals and Silicon-Polymer Hybrids: Synthesis, Surface Engineering, and Applications. *Angew. Chem. Int. Ed.* **2016**, *55* (7), 2322–2339. https://doi.org/10.1002/anie.201506065.
(126) Cheng, X.; Lowe, S. B.; Reece, P. J.; Gooding, J. J. Colloidal Silicon Quantum Dots: From Preparation to the Modification of Self-Assembled Monolayers (SAMs) for Bio-Applications. *Chem. Soc. Rev.* **2014**, *43* (8), 2680–2700. https://doi.org/10.1039/C3CS60353A.
(127) Hessel, C. M.; Rasch, M. R.; Hueso, J. L.; Goodfellow, B. W.; Akhavan, V. A.; Puvanakrishnan, P.; Tunnel, J. W.; Korgel, B. A. Alkyl Passivation and Amphiphilic Polymer Coating of Silicon Nanocrystals for Diagnostic Imaging. *Small* **2010**, *6* (18), 2026–2034. https://doi.org/10.1002/smll.201000825.
(128) Zhou, T.; Anderson, R. T.; Li, H.; Bell, J.; Yang, Y.; Gorman, B. P.; Pylypenko, S.; Lusk, M. T.; Sellinger, A. Bandgap Tuning of Silicon Quantum Dots by Surface Functionalization with Conjugated Organic Groups. *Nano Lett.* **2015**, *15* (6), 3657–3663. https://doi.org/10.1021/nl504051x.
(129) Yan, E.; Balgley, R.; Morla, M. B.; Kwon, S.; Musgrave, C. B.; Brunschwig, B. S.; Goddard, W. A.; Lewis, N. S. Experimental and Theoretical Comparison of Potential-Dependent Methylation on Chemically Exfoliated WS_2 and MoS_2. *ACS Appl. Mater. Interfaces* **2022**, *14* (7), 9744–9753. https://doi.org/10.1021/acsami.1c20949.
(130) Michalet, X.; Pinaud, F. F.; Bentolila, L. A.; Tsay, J. M.; Doose, S.; Li, J. J.; Sundaresan, G.; Wu, A. M.; Gambhir, S. S.; Weiss, S. Quantum Dots for Live Cells, in Vivo Imaging, and Diagnostics. *Science* **2005**, *307* (5709), 538–544. https://doi.org/10.1126/science.1104274.
(131) Mu, Q.; Xu, H.; Li, Y.; Ma, S.; Zhong, X. Adenosine Capped QDs Based Fluorescent Sensor for Detection of Dopamine with High Selectivity and Sensitivity. *Analyst* **2013**, *139* (1), 93–98. https://doi.org/10.1039/C3AN01592K.
(132) Li, Y.-J.; Harroun, S. G.; Su, Y.-C.; Huang, C.-F.; Unnikrishnan, B.; Lin, H.-J.; Lin, C.-H.; Huang, C.-C. Synthesis of Self-Assembled Spermidine-Carbon Quantum Dots Effective against Multidrug-Resistant Bacteria. *Adv. Healthc. Mater.* **2016**, *5* (19), 2545–2554. https://doi.org/10.1002/adhm.201600297.
(133) Chinen, A. B.; Guan, C. M.; Ferrer, J. R.; Barnaby, S. N.; Merkel, T. J.; Mirkin, C. A. Nanoparticle Probes for the Detection of Cancer Biomarkers, Cells, and Tissues by Fluorescence. *Chem. Rev.* **2015**, *115* (19), 10530–10574. https://doi.org/10.1021/acs.chemrev.5b00321.
(134) Zhao, D.; Song, H.; Hao, L.; Liu, X.; Zhang, L.; Lv, Y. Luminescent ZnO Quantum Dots for Sensitive and Selective Detection of Dopamine. *Talanta* **2013**, *107*, 133–139. https://doi.org/10.1016/j.talanta.2013.01.006.

(135) Meng, C.; Xiao, Y.; Wang, P.; Zhang, L.; Liu, Y.; Tong, L. Quantum-Dot-Doped Polymer Nanofibers for Optical Sensing. *Adv. Mater.* **2011**, *23* (33), 3770–3774. https://doi.org/10.1002/adma.201101392.

(136) Xu, S.; Lu, H.; Li, J.; Song, X.; Wang, A.; Chen, L.; Han, S. Dummy Molecularly Imprinted Polymers-Capped CdTe Quantum Dots for the Fluorescent Sensing of 2,4,6-Trinitrotoluene. *ACS Appl. Mater. Interfaces* **2013**, *5* (16), 8146–8154. https://doi.org/10.1021/am4022076.

(137) Ge, S.; Zhang, C.; Zhu, Y.; Yu, J.; Zhang, S. BSA Activated CdTe Quantum Dot Nanosensor for Antimony Ion Detection. *Analyst* **2009**, *135* (1), 111–115. https://doi.org/10.1039/B915622D.

(138) Lou, Y.; Zhao, Y.; Chen, J.; Zhu, J.-J. Metal Ions Optical Sensing by Semiconductor Quantum Dots. *J. Mater. Chem. C* **2013**, *2* (4), 595–613. https://doi.org/10.1039/C3TC31937G.

(139) Lan, X.; Voznyy, O.; Kiani, A.; García de Arquer, F. P.; Abbas, A. S.; Kim, G.-H.; Liu, M.; Yang, Z.; Walters, G.; Xu, J.; Yuan, M.; Ning, Z.; Fan, F.; Kanjanaboos, P.; Kramer, I.; Zhitomirsky, D.; Lee, P.; Perelgut, A.; Hoogland, S.; Sargent, E. H. Passivation Using Molecular Halides Increases Quantum Dot Solar Cell Performance. *Adv. Mater.* **2016**, *28* (2), 299–304. https://doi.org/10.1002/adma.201503657.

(140) Tang, J.; Kemp, K. W.; Hoogland, S.; Jeong, K. S.; Liu, H.; Levina, L.; Furukawa, M.; Wang, X.; Debnath, R.; Cha, D.; Chou, K. W.; Fischer, A.; Amassian, A.; Asbury, J. B.; Sargent, E. H. Colloidal-Quantum-Dot Photovoltaics Using Atomic-Ligand Passivation. *Nat. Mater.* **2011**, *10* (10), 765–771. https://doi.org/10.1038/nmat3118.

(141) Kim, J.; Ouellette, O.; Voznyy, O.; Wei, M.; Choi, J.; Choi, M.-J.; Jo, J. W.; Baek, S.-W.; Fan, J.; Saidaminov, M. I.; Sun, B.; Li, P.; Nam, D.-H.; Hoogland, S.; Lu, Z.-H.; García de Arquer, F. P.; Sargent, E. H. Butylamine-Catalyzed Synthesis of Nanocrystal Inks Enables Efficient Infrared CQD Solar Cells. *Adv. Mater.* **2018**, *30* (45), 1803830. https://doi.org/10.1002/adma.201803830.

(142) Semonin, O. E.; Luther, J. M.; Beard, M. C. Quantum Dots for Next-Generation Photovoltaics. *Mater. Today* **2012**, *15* (11), 508–515. https://doi.org/10.1016/S1369-7021(12)70220-1.

(143) Derfus, A. M.; Chan, W. C. W.; Bhatia, S. N. Probing the Cytotoxicity of Semiconductor Quantum Dots. *Nano Lett.* **2004**, *4* (1), 11–18. https://doi.org/10.1021/nl0347334.

(144) Li, H.; Wu, Z.; Zhou, T.; Sellinger, A.; Lusk, M. T. Double Superexchange in Quantum Dot Mesomaterials. *Energy Environ. Sci.* **2014**, *7* (3), 1023. https://doi.org/10.1039/c3ee42991a.

(145) Sun, L.; Koh, Z. Y.; Wang, Q. PbS Quantum Dots Embedded in a ZnS Dielectric Matrix for Bulk Heterojunction Solar Cell Applications. *Adv. Mater.* **2013**, *25* (33), 4598–4604. https://doi.org/10.1002/adma.201301544.

(146) Liu, C.-Y.; Holman, Z. C.; Kortshagen, U. R. Hybrid Solar Cells from P3HT and Silicon Nanocrystals. *Nano Lett.* **2009**, *9* (1), 449–452. https://doi.org/10.1021/nl8034338.

(147) Kelly, J. A.; Henderson, E. J.; Veinot, J. G. C. Sol–Gel Precursors for Group 14 Nanocrystals. *Chem. Commun.* **2010**, *46* (46), 8704. https://doi.org/10.1039/c0cc02609c.

(148) Gregori, G.; Kleebe, H.-J.; Readey, D. W.; Soraru, G. D. Energy-Filtered TEM Study of Ostwald Ripening of Si Nanocrystals in a SiOC Glass. *J. Am. Ceram. Soc.* **2006**, *89* (5), 1699–1703. https://doi.org/10.1111/j.1551-2916.2006.00971.x.

(149) Mastronardi, M. L.; Hennrich, F.; Henderson, E. J.; Maier-Flaig, F.; Blum, C.; Reichenbach, J.; Lemmer, U.; Kübel, C.; Wang, D.; Kappes, M. M.; Ozin, G. A. Preparation of Monodisperse Silicon Nanocrystals Using Density Gradient Ultracentrifugation. *J. Am. Chem. Soc.* **2011**, *133* (31), 11928–11931. https://doi.org/10.1021/ja204865t.

(150) Falk, M.; Whalley, E. Infrared Spectra of Methanol and Deuterated Methanols in Gas, Liquid, and Solid Phases. *J. Chem. Phys.* **1961**, *34* (5), 1554–1568. https://doi.org/10.1063/1.1701044.

(151) Nikolic, G. *Fourier Transforms: New Analytical Approaches and FTIR Strategies*; Intech, 2011.

(152) Jo, J. W.; Choi, J.; García de Arquer, F. P.; Seifitokaldani, A.; Sun, B.; Kim, Y.; Ahn, H.; Fan, J.; Quintero-Bermudez, R.; Kim, J.; Choi, M.-J.; Baek, S.-W.; Proppe, A. H.; Walters, G.; Nam, D.-H.; Kelley, S.; Hoogland, S.; Voznyy, O.; Sargent, E. H. Acid-Assisted Ligand Exchange Enhances Coupling in Colloidal Quantum Dot Solids. *Nano Lett.* **2018**, *18* (7), 4417–4423. https://doi.org/10.1021/acs.nanolett.8b01470.